Effect of Heat Treatment on Microstructure and Mechanical Behavior of Additively Manufactured Nitinol Shape Memory Alloys

Student name: Weijia Zhu

Student number: 5032601

Faculty of Mechanical, Maritime and Materials Engineering (3mE)

Delft University of Technology

Supervisors: Dr. Vera Popovich

Jia-Ning Zhu

Acknowledgements

With this thesis comes an end to my master at the Delft University of Technology. Firstly, I am very grateful to my supervisor Dr. Vera Popovich for giving me the opportunity to work on this project. Thank you so much for all your coaching and feedback during the meetings. I also would like to thank my daily supervisor Jia-Ning Zhu. I really appreciate your patient guidance and valuable instructions on my experimental tests. Without your help, I could not complete my work so quickly.

I would also like to thank Ton and Elise for helping me with setting up the mechanical test equipment for almost 3 weeks. They also gave me many suggestions about my work. I am so grateful to Sander van Asperen and Maria Terol Sanchez for the fundamental training in the polishing lab. I would like to thank Hans Brouwer for the furnace training and Richard Huizenga for carrying out the X-ray analysis. In addition, thanks to all my friends for the unforgettable memory at TU Delft.

Lastly, I would like to thank my husband Hao Ma for his love and accompany. And thank my parents, my parents in law and my brother and sister for always supporting me.

Abstract

Nitinol shape memory alloys (SMAs) have a unique combination of shape memory capability, making it an attractive material for various engineering and biomedical applications. Additive manufacturing (AM) by laser powder bed fusion (L-PBF) allows to produce Nitinol net-shape parts, which broadens its applications. Due to the high heating and cooling rate during L-PBF process, there always exists supersaturated solute elements and metastable structures in L-PBF Nitinol parts. Microstructure and precipitate characteristics have detrimental effects on phase transformation and shape memory behavior of Nitinol alloys. Proper heat treatment is an important method to mitigate these detrimental effects and improve the properties of Nitinol. In this project, the effect of heat treatment on shape memory behavior of equiatomic Nitinol fabricated by L-PBF is studied. The heat treatment process is optimized, which is annealing at 950 ^{o}C for 5.5h and subsequent aging at 350 ^{o}C for 18 hours. By applying the optimized heat treatment process, the cyclic stability of the Ti50Ni50 SMA are improved by 50% for recoverable strain and 70 MPa for applied stress. Additionally, the relationship among the microstructure and precipitates, functional and mechanical properties, and heat treatment parameters are investigated.

Contents

List of figures

List of tables

Chapter 1 Introduction

Shape memory alloys (SMAs) are functional materials with shape memory effect and superelasticity [1]. Nitinol (NiTi) SMAs are attractive material for various engineering and biomedical applications [2]. Nitinol SMAs have two different phases, including stable austenite at high temperature and stable martensite at low temperature, three different crystal structures including twinning martensite, detwinning martensite and austenite, and achieve the shape memory effect or superelasticity through six transformation modes between the above three different crystal structures [2]. Moreover, they also have excellent mechanical properties, corrosion resistance and biocompatibility, which make them widely used in industrial, medical and daily life [3]. However, due to its high strength, high reactivity and high work hardening, most of the Nitinol SMAs fabricated by conventional methods are small parts with simple geometries. The difficulties existing in the preparation and machining process limit the further application for Nitinol SMAs.

The development of additive manufacturing technology (AM) has provided another method to fabricate the complex shape and structure of Nitinol SMAs and expanded the application range of Nitinol SMAs. L-PBF is a common method to fabricate Nitinol SMAs, because it provides a better geometrical accuracy and surface finish. Since the functional properties of Nitinol SMAs are based on the transformation between martensite and austenite, the phase transformation temperatures and transformation paths are the key factors affecting the practical application of Nitinol SMAs [3]. However, due to the high heating and cooling rate during L-PBF process, there always exist supersaturated solute elements and metastable structures in L-PBF Nitinol parts, which can affect their microstructure and precipitates. Microstructure and precipitate characteristics have detrimental effects on phase transformation and shape memory behavior of Nitinol SMAs.

Ni-rich, Ti-rich and equiatomic Nitinol SMAs have different properties due to their different atomic ratio of Ni and Ti [2]. In general, Ni-rich Nitinol has better superelastic property, while near equiatomic and Ti-rich Nitinol show better shape memory property [4]. Studies have found that heat treatments can effectively change phases, microstructure and phase element content distribution of Ni-rich Nitinol SMAs fabricated by L-PBF [5]. The change in microstructure and precipitates evolution as a function of various heat treatments is crucial for tailoring L-PBF Nitinol shape memory behavior. However, less study has been done for equiatomic Nitinol SMAs. Therefore, this project aims to study the effect of heat treatments on

the shape memory behaviors of equiatomic L-PBF Nitinol SMAs. This is very important for broadening the application of equiatomic Nitinol SMAs.

Chapter 2 Literature Review

2.1 Laser Powder Bed Fusion

2.1.1 General Background

Additive manufacturing (AM), also known as 3D printing, was firstly developed in the 1980s to produce models and prototype parts [6]. Compared with traditional manufacturing, AM has advantages in reducing waste, reducing lead time and cost, and customizing complex geometries and material properties. Hence, AM has gained popularity in academic research as well as industrial applications. In particular, additive manufacturing is revolutionizing manufacturing across various industries, such as biomedical, aerospace, buildings, automotive, engineering, satellite and food supply chains [7]. Nowadays, they have been able to produce complex net-shaped or nearly net-shaped functional parts, including metals, polymers, composites and ceramics. For metal materials, additive manufacturing methods mainly include electron beam rapid manufacturing, (EBRM), direct metal deposition (DMD), laser engineered net shaping (LENS), selective laser sintering (SLS), electron beam melting (EBM), and laser powder bed fusion (L-PBF), etc [8]. Among these additive manufacturing methods, L-PBF has been widely used in various materials fabrication due to its high dimensional accuracy and good surface quality.

Deckard et al. first proposed SLS in 19 centuries [7]. After that, L-PBF technology was proposed based on the concept of SLS in Germany. The schematic diagram of the working principle of L-PBF is shown in Fig. 2. 1 [9]. A high-power density laser is employed to focus the spot to a diameter of tens to hundreds of microns. The scanning path of the laser is changed through the scanning galvanometer, and the molten metal powder is scanned according to the two-dimensional slice model. When a layer is melted, the forming cylinder will lower the layer thickness, and the powder feeding cylinder will increase the layer thickness. The roller will send the powder into the forming cylinder, and the laser will melt again according to the model, and then repeat the above process until the entire sample is complete Melt forming. After several years of continuous research and development, the technology successfully produced parts with excellent mechanical properties, dense structure and high precision.

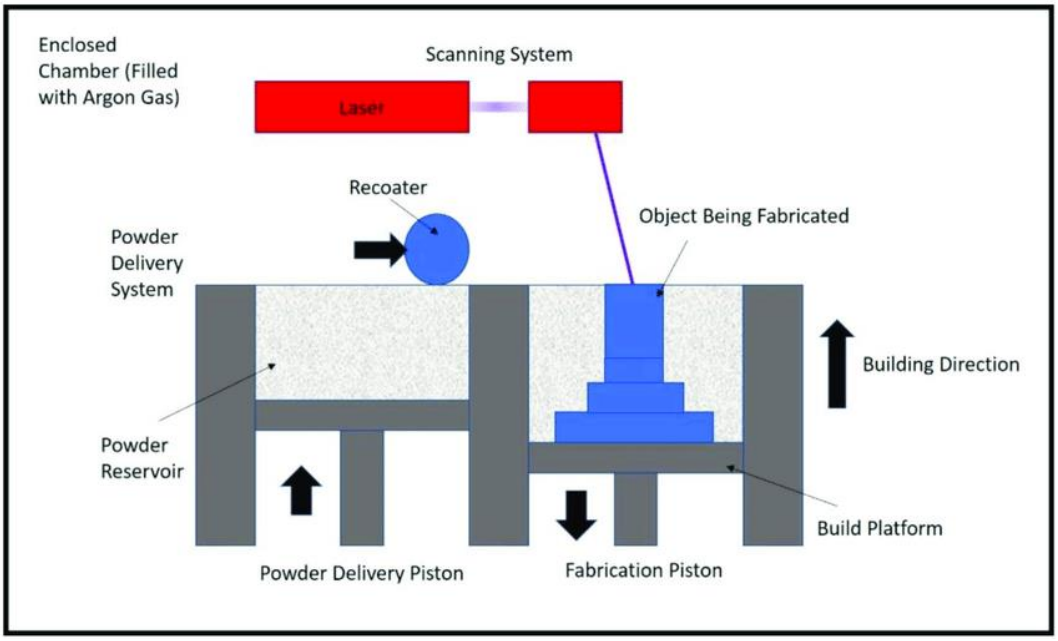

Fig. 2. 1 Schematic diagram of L-PBF process [9].

Generally, L-PBF has the following characteristics [10]:

1) The shape of components is not restricted. L-PBF is not limited by the geometry of the components, as long as the computer can figure out the three-dimensional configuration of the sample. On the other hand, L-PBF is a layer by layer manufacturing technology, which dramatically reduces production costs.

2) High accuracy. The accuracy of L-PBF mainly depends on the laser spot diameter. With the rapid development of fiber lasers, the minimum spot diameter of the laser can be at the micron level or even the nanometer level, which dramatically improves the accuracy of L-PBF.

3) The formed components have high density and good performance. During the L-PBF forming process, a high-energy beam laser can completely melt the metal powder and form high-density parts after rapid solidification. In addition, L-PBF has the characteristics of micro-melt pool smelting reaction and rapid solidification, which makes the parts prepared by it have excellent mechanical properties.

2.1.2 Process Parameters

Although L-PBF technology has the above advantages, many parameters need to be optimized during the production process by L-PBF. These parameters are categorized as Fig. 2. 2 [11]. L-PBF technology is a complex physical metallurgical process. Its forming process involves many physical phenomena, including laser energy absorption and transfer, heat convection

between the material and the surroundings, heat transfer among powder particles, microstructure evolution, material melting, vaporization, chemical reaction, etc. The laser heat source moves very fast during the forming process. As explained in Fig. 2. 1, the high-energy laser beam quickly and selectively melts the metal powders according to the predetermined scanning path. The entire energy transfer process is fast and highly nonlinear. The metal powders are melted to form a molten pool by the high-energy laser beam. And physical and chemical reactions occur in the molten pool. The thermophysical properties of the forming material are also different at different temperatures. Fig. 2. 3 lists the L-PBF process parameters. The following shows symbols of some relative parameters: laser power (P), scanning speed (v), hatch spacing (h), layer thickness (t), and spot size (d) [12]. These parameters affect the L-PBF forming process, making the microstructure and mechanical properties of the formed workpiece different, which affects the quality and performance of L-PBF forming parts. Below are explanations for some L-PBF process parameters.

1) Laser type: In the L-PBF process, the shorter the laser wavelength, the higher the laser absorption rate of the powder material, and the easier the laser energy will be absorbed by the powder material. Therefore, the fiber laser with good stability and focus is usually selected.

2) Laser energy density: An important engineering parameter in additive manufacturing technology. In the L-PBF process, the input laser energy density is a vital aspect affecting products' density and defects. As a rule, the higher the input laser energy density, the higher the relative density of the L-PBF part. Too low laser density will cause the powder to melt incompletely and cause delamination. Too high laser density will cause splashes in the molten pool, causing warping, cracking, spheroidization, and other defects. Volumetric input laser energy density (E_v, J/mm) for L-PBF process is described by the following equation [13]:

$$E_v = P/vht \qquad \text{Eq. (1)}$$

3) Powder material: The particle size of the powder material, accompanied by its distribution and morphology, directly affects the microscopy morphology of L-PBF samples [12]. The number of particles contained in the laser spot diameter is limited. The smaller the microscopic area, the harder to control the uniformity of samples.

4) Layer thickness: Layer thickness refers to the thickness of the powder layer leveled onto the powder bed by the powder delivery system [12]. The layer thickness influences the energy transferred to the powder per unit volume. Layer thickness is also a key factor affecting density. The choice of thickness should consider the physical and chemical properties of the powder

material and the characteristics of the machine. If a layer is too thick, it is not easy to be completely melted, and the molten pool is difficult to control; If the layer is too thin, the precision requirements of the processing technology and equipment will be stricter, which restricts the production.

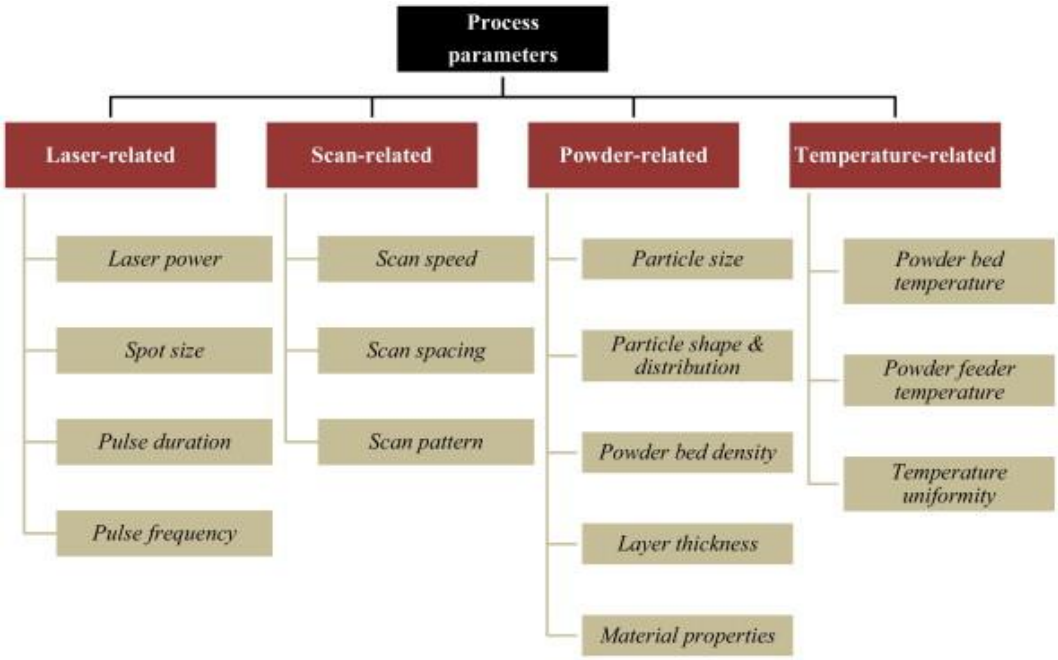

Fig. 2. 2 Controlling parameters in L-PBF process [11].

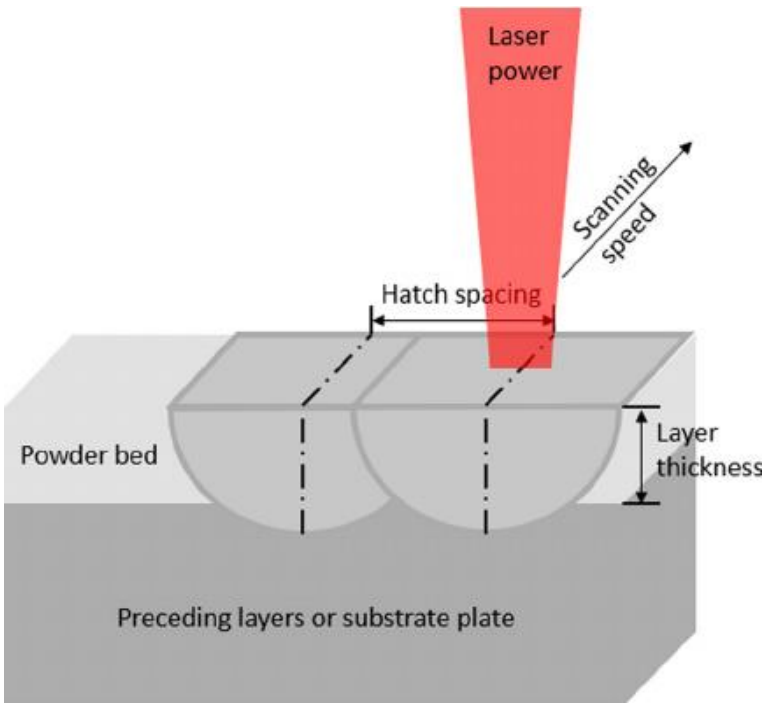

Fig. 2. 3 Schematic of L-PBF process [14].

2.2 Nitinol Shape Memory Alloys

2.2.1 Introduction and Phase Transformation of NiTi Alloys

Phase diagram of NiTi alloy system is essential for guiding heat treatment process and improving shape memory properties. Fig. 2. 4 is the phase diagram of NiTi binary alloy. NiTi alloys with a near equiatomic ratio are called Nitinol. Nitinol can exhibit shape memory behavior and superelasticity. The solubility curve on the Ti-rich side decreases rapidly with temperature. Moreover, the primary precipitation is the cubic Ti_2Ni phase. The solubility curve on the Ni-rich side changes more slowly as the temperature decreases, with Ni_3Ti, Ni_3Ti_2, and Ni_4Ti_3 precipitate [15]. Ni_4Ti_3 phase occurs at lower aging temperature and shorter aging time. Slightly higher aging temperature and longer aging time will lead to metastable Ni_3Ti_2 precipitation. The long-term higher aging temperature will produce stable Ni_3Ti phases. Ni_4Ti_3 precipitates are particularly important for the shape memory property of NiTi alloy [15]. Hence, aging temperature and duration are both significant parameters for the shape memory effect of NiTi alloys.

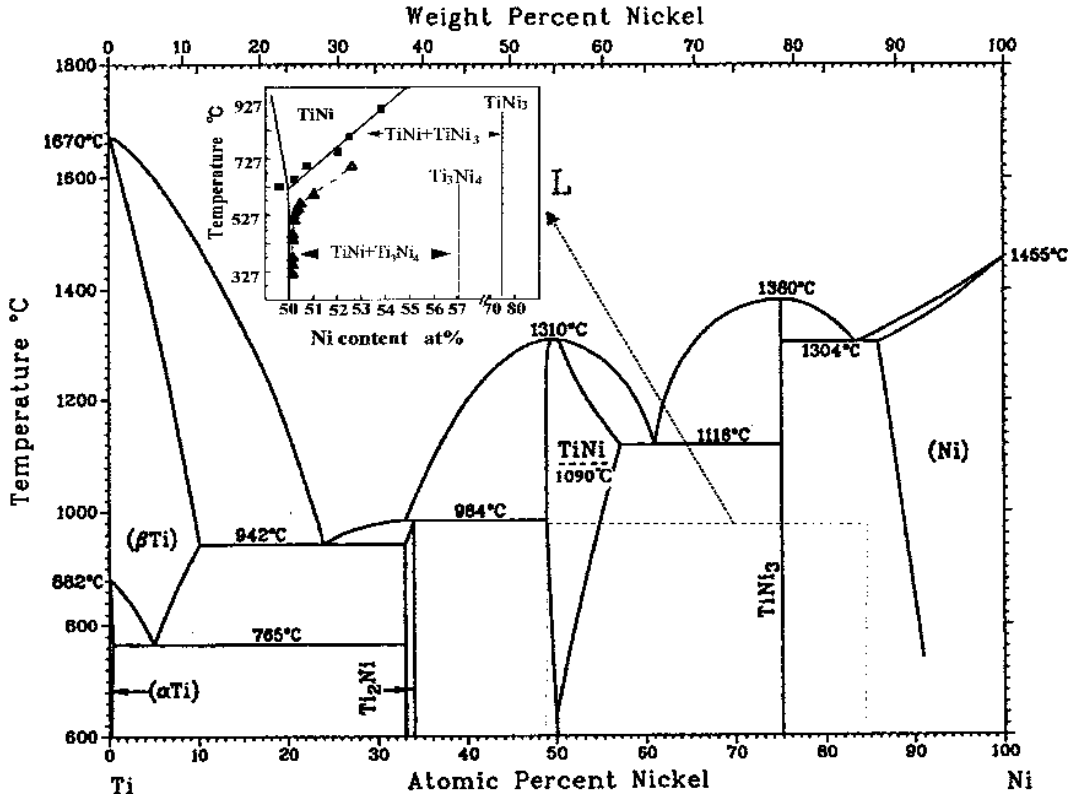

Fig. 2. 4 Phase diagram of a NiTi alloy [15].

NiTi alloys have two phases (austenite and martensite), three different crystal structures (for Ni-rich Nitinol, i.e., the austenite B2 phase of cubic, the mesophase R of the trigonal structure,

and the monoclinic structure martensitic B19' phase). As shown in Fig. 2. 5 [15], there are three phase transformation paths in NiTi-based SMAs, showing a transition from high-temperature body-centered cubic austenite B2 phase to low-temperature monoclinic martensite B19' phase. For the binary NiTi alloy after solution treatment, a direct transformation from B2 to B19' will occur. For ternary Ti-Ni-Cu and Ti-Ni-Fe alloys, two different continuous second-order martensitic transformations will occur. Moreover, if NiTi binary alloy is aged at proper temperatures, it will also show a continuous phase transition from B2 to R and then to B19. The phase transition from parent phase to martensite is called martensite phase transition, and vice versa is called a reverse phase transition.

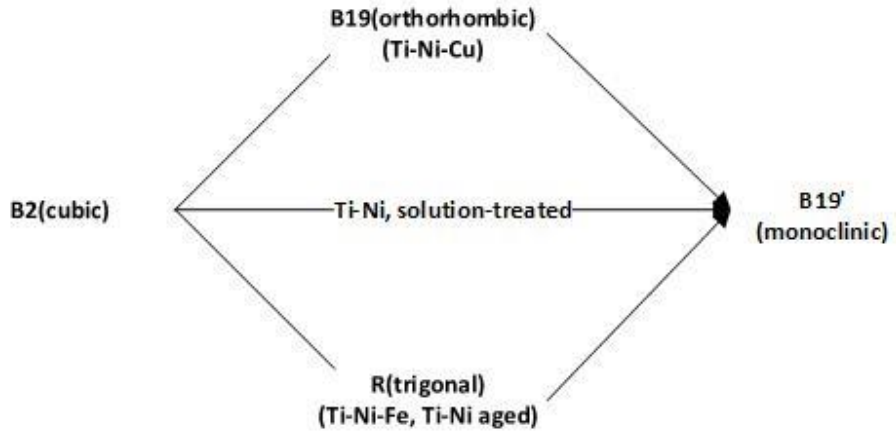

Fig. 2. 5 Three transformation paths in NiTi-based alloys [15].

The phase transformation behavior of Nitinol SMAs is usually measured by differential scanning calorimetry (DSC). As shown in Fig. 2. 5, after complete solution treatment of Nitinol SMAs, austenite is directly transformed into martensite during cooling and heating. In the dislocation network or the related Ni_4Ti_3 two-phase particles, the intermediate R phase becomes the necessary product in the positive transformation process. Therefore, the DSC detects the two-stage martensitic transformation B2 -R-B19', as shown in Fig. 2. 6. Multi-level transformations are often observed in Ni-rich Nitinol SMAs after aging treatment. As stipulated at ASTM F2005-05 [16], the starting transformation temperatures of the R phase and martensite phase are R_s and M_s, respectively. R_f and M_f represent the completion temperature of R phase transformation and martensitic transformation, respectively. In the reverse phase transformation process, the start temperature and end temperature of austenite transformation are expressed as A_s and A_f. M_d is martensite desist temperature and is defined as "the temperature above A_f at which stress-induced martensite will no longer form" [16].

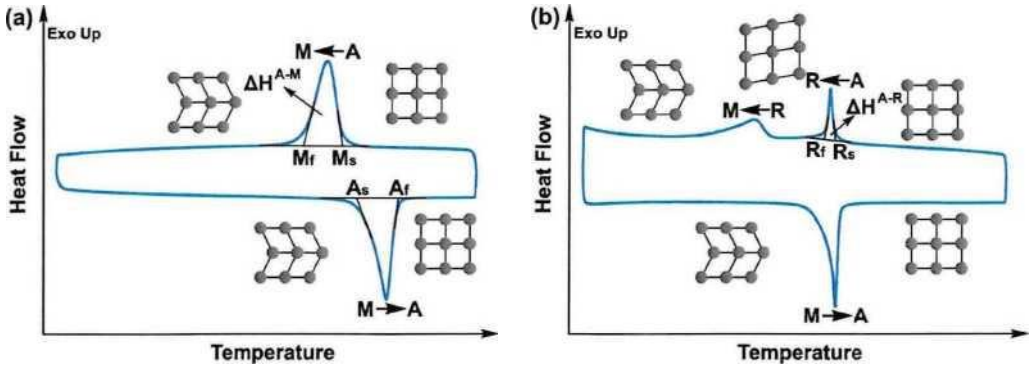

Fig. 2. 6 Schematic illustration of thermoelastic martensitic transformation as detected by DSC [17].

2.2.2 Shape Memory Effect

Shape memory effect and superelasticity are typical characteristics of Nitinol. Shape memory effect is a temperature-induced change in alloy's crystal structure. Shape memory effect refers to a phenomenon, in which a material is able to return to its formerly fabricated shape when exposed to appropriate heat treatments after deforming at lower temperatures [2]. The nearly equiatomic NiTi-based alloys, Nitinol, exhibit an excellent shape memory effect. The transformation composition for Nitinol is 49 to 51 at.% Ni, with a range of martensite transformation temperatures from –50 to 110 °C and a magnitude of hysteresis of around 30 degrees [2]. The underlying reason for the shape memory effect is the thermoelastic martensite deformation. When applied stress below austenite transformation temperature, Nitinol is deformed following a detwinning mechanism. Upon unloading and heating, the detwinned structure reverts to the parent phase, resulting in the recovery of the deformation. Fig. 2. 7 (a) shows the path that thermal shape memory occurs during loading and unloading. Assuming an austenitic state Nitinol, a complete transformation from austenite to twinned martensite occurs if Nitinol is cooled below M_f without applied stress. Upon loading, the material is deformed through reorientation and detwinning of martensite along the path I to II. Then, releasing the load leads to elastic recovery of the reoriented detwinned martensite, indicating as path II to III, and the material stays deformed. If heating the deformed Nitinol alloy at a higher temperature than A_f, the Nitinol alloy will transform from martensite to austenite. In the end, the Nitinol alloy remembers its former shape.

Superelasticity refers to a stress-induced change in alloy's crystal structure. It stands for the nonlinear recoverable deformation behavior of shape memory alloys. It happens above the A_f. The austenitic state Nitinol can transform to a martensitic state upon loading along the path I

to II (Fig. 2. 7 (b). A large elastic strain of up to 11% can be achieved [18]. When the load is released, the Nitinol alloy will transform back to an austenitic state along path II to I. At last, the superelastic deformation will be recovered, displaying a hysteresis loop in the stress-strain curve.

Fig. 2. 8 gives an illustration of deformation regions and critical stress as a function of temperature. The shape memory effects exist below A_f, while superelasticity exists between A_f and M_d. If the sample is deformed above M_d, shape memory recovery and superelasticity cannot be observed, and the material will deform in the form of nonlinear plastic behavior.

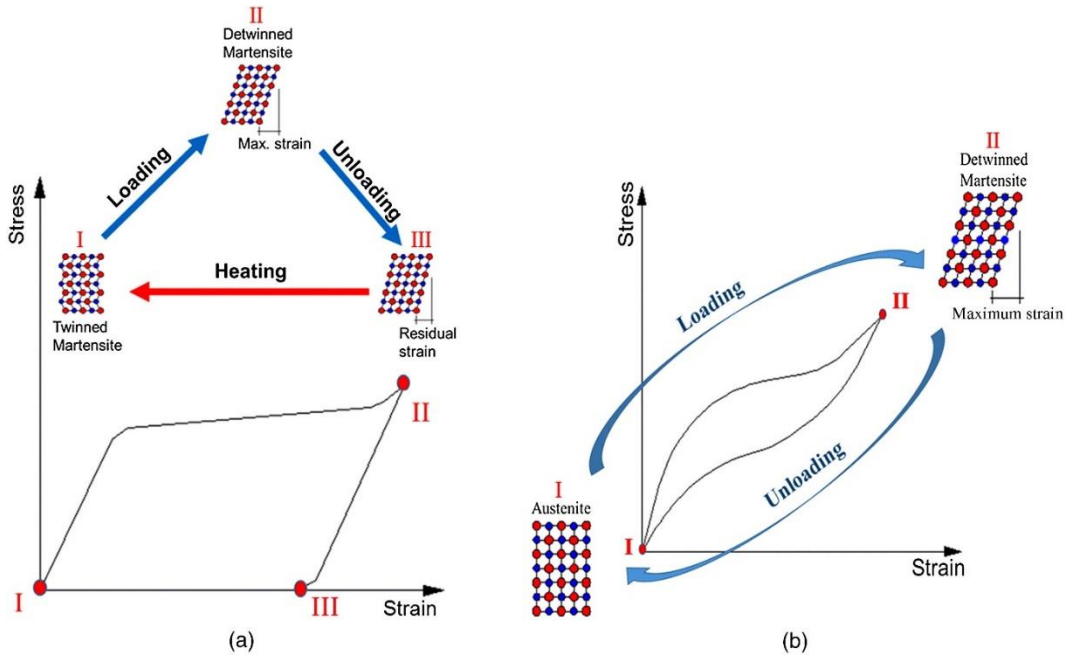

Fig. 2. 7 (a) Shape memory effect (b) Superelasticity [19].

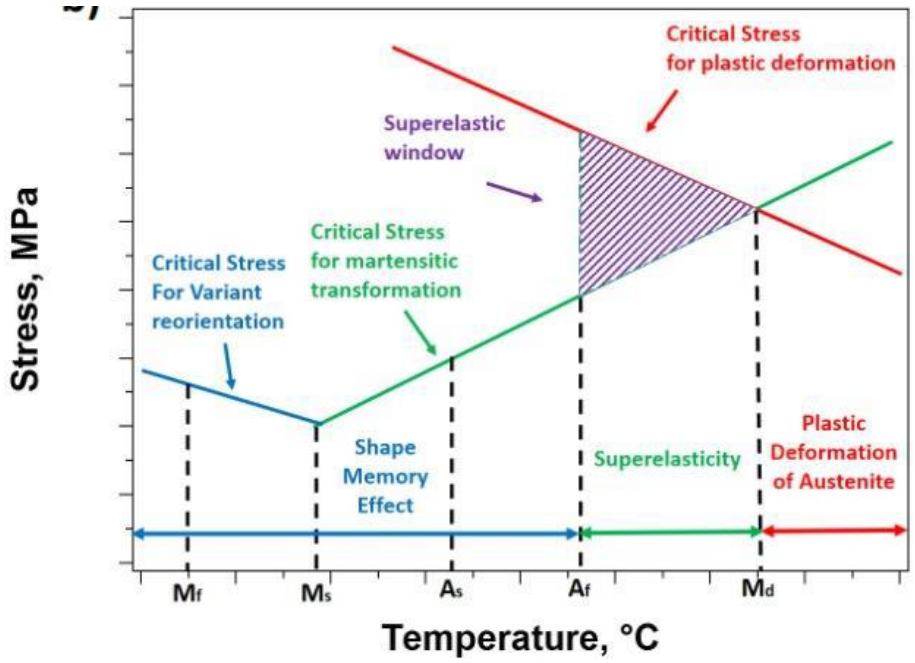

Fig. 2. 8 The critical stress and mechanical properties regions of SMAs as a function of temperature [20].

2.2.3 L-PBF Nitinol Shape Memory Alloys

As an intermetallic compound, NiTi alloy is difficult to manufacture by traditional processing methods. Therefore, some scholars use laser selective melting forming technology to manufacture NiTi alloy parts. As explained above, L-PBF parameters affect the properties of components, to optimize the parameters is a must. Table 2. 1 lists some applied L-PBF parameters by different groups. The energy input is valued by Eq. 1.

Table 2. 1 L-PBF parameters to produce NiTi achieved by different groups.

Effective laser power (W)	Scanning velocity (mm/s)	Hatch distance (lm)	Layer thickness (lm)	Energy input (J/mm^3)	Author(s)
77	200	120	50	64.1	Meier et al. [21]
77	200	120	50	64.1	Haberland et al. [22]
250	1250	120	30	55.5	Taheri Andani et al. [23]
250	1250	120	30	55.5	Saedi et al. [24]
40, 250	160, 110	75, 60	30	111, 126	Dadbaksh et al. [25]

56	133	120	50	70	Bormann et al. [26]
50	100–160	100	60	52–83	Shishkovsky et al. [27]
250	500, 600, 800, 1250	100, 120, 140, 187	30, 60, 75	48–99	Zhu et al. [28]

Saedi. et al. [13], studies the effects of laser power and scanning speed on the transformation behavior and properties of L-PBF Nitinol. Fig. 2. 9 exhibits the optical microscopy images of four samples, which fabricated by L-PBF at a constant scanning speed, but variable laser power values. While Fig. 2. 10 displays four samples fabricated by L-PBF at a constant laser power and different scanning speeds. It is noticeable that scanning speed and laser power significantly affect the grains size and structures. Fig. 2. 11 shows the effects of energy level/scanning speed on A_f and M_s. Vicker hardness variation is also demonstrated. The results show that transformation temperatures and Vicker hardness are all related to energy level and scanning speed.

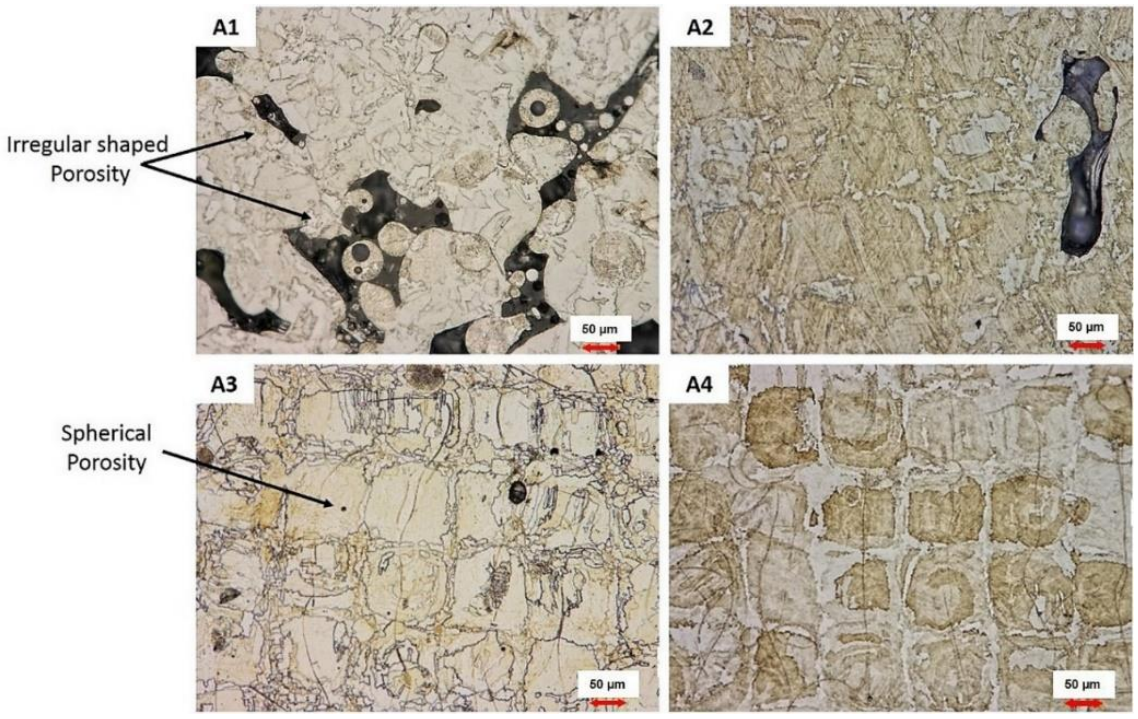

Fig. 2. 9 Optical Micrographs of' L-PBF Ni50.8Ti49.2, scanning speeds v is 1000 mm/s, laser powers (W) are: (A1) P = 100, (A2) P = 150, (A3) P = 200, and (A4) P = 250 [13].

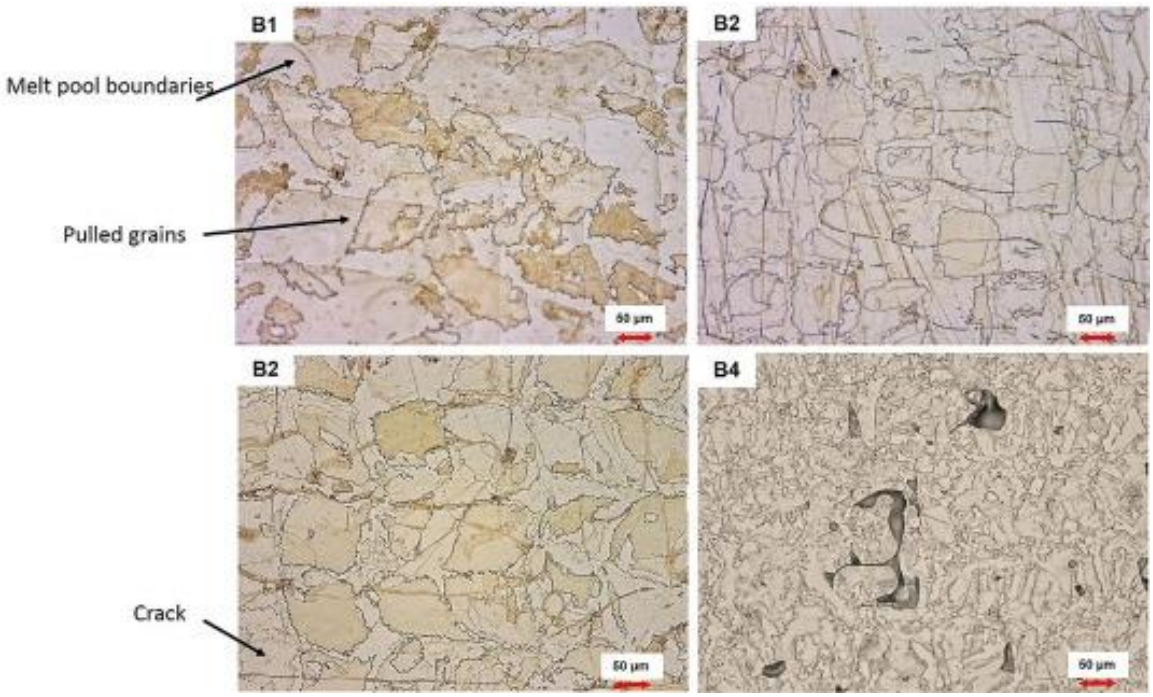

Fig. 2. 10 Optical Micrographs of' L-PBF Ni50.8Ti49.2, laser power is 100 W, scanning speeds v (mm/s) are: (B1) 125, (B2) 175, (B3) 225, and (B4) 500 [13].

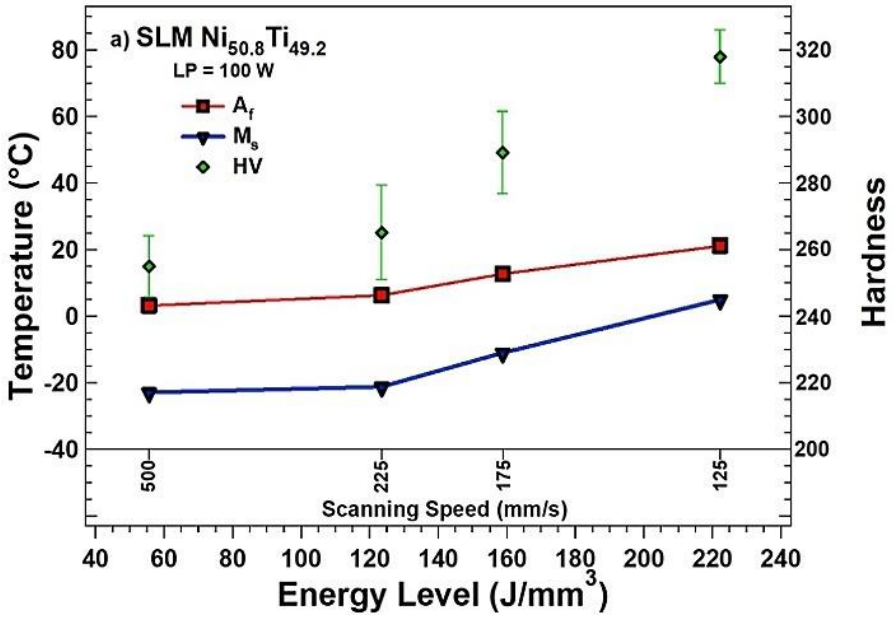

Fig. 2. 11 M_s and A_f temperatures, and Vicker hardness as a function of energy level and scanning speed [13].

2.2.4 Properties

Nitinol SMAs can exhibit shape memory behavior when heated at a higher temperature than austenite transformation temperature. Hence, the transformation temperatures are the most critical property for representing Nitinol shape memory alloys. A_f represents the finish of

austenite transformation. Therefore, the shape recovery is complete at A_f. Table 2. 1 summarizes the transformation temperatures, the primary physical properties and some of the mechanical properties of Nitinol SMAs with an A_f value of about 110 °C [2]. Note that nickel strongly affects the transformation temperature and yield strength of the austenite. Excess nickel decreases the transformation temperature and improves the yield strength. Proper heat treatments can significantly improve the shape memory properties and strength. Therefore, developing the proper heat treatment procedures is vital to produce Nitinol SMAs with desired properties.

Differential scanning calorimeter (DSC) is the most popular method of characterizing the transformation behaviors in SMAs. ASTM F2004 is the standard for the DSC test method [29]. For example, Fig. 2. 12 shows the transformation information of a NiTi alloy by DSC. Besides, the stress-strain properties can be measured in a standard tensile test at different temperatures. ASTM F2516 is the governing standard for tensile testing of Nitinol [30]. Moreover, the approximate transformation temperatures can also be obtained according to the changing of properties. In a typical Nitinol tensile test, 6 percent strain is applied to the sample firstly, then unload and subsequently keeps increasing the strain until failure. The measurements of the ultimate tensile strength (UTS) and elongation are the same as other materials. Besides, more parameters can be measured. When the tensile test is employed above A_f, upper plateau strength, lower plateau strength and the residual elongation (i.e., permanent set) can be measured. The upper plateau strength is recorded at 3 percent strain recorded during loading, while the lower plateau strength is measured at 2.5 percent strain upon unloading. Residual elongation is the permanent set after unloading. Fig. 2. 13 displays these critical points. Fig. 2. 14 is stress-strain curves for austenite phase (at a higher temperature than M_d), martensite phase (at a temperature below M_s), and austenite and stress-induced martensite phases (at temperatures range from A_f to M_d). The different slopes of stress-strain curves of austenite and martensite in different temperatures are why their yield strengths in **Error! Reference source n ot found.** are a range.

Table 2. 2 Properties of binary Nitinol SMAs [2].

Properties	**Property value**
Melting temperatures, °C	1300
Density, g/cm^3	6.45
Resistivity/ uΩ cm	

Austenite	100
Martensite	70
Thermal conductivity, W/m °C	
Austenite	18
Martensite	8.5
Corrosion resistance	Similar to 300 series stainless steel or titanium alloys
Young's modulus, GPa	
Austenite	Around 83
Martensite	Around 28–41
Yield strength, MPa	
Austenite,	195–690
Martensite,	70–140
Ultimate tensile strength, MPa	895
Transformation temperatures, °C	-200–110
Latent heat of transformation, kJ/kg	167
Shape memory strain	8.5% maximum

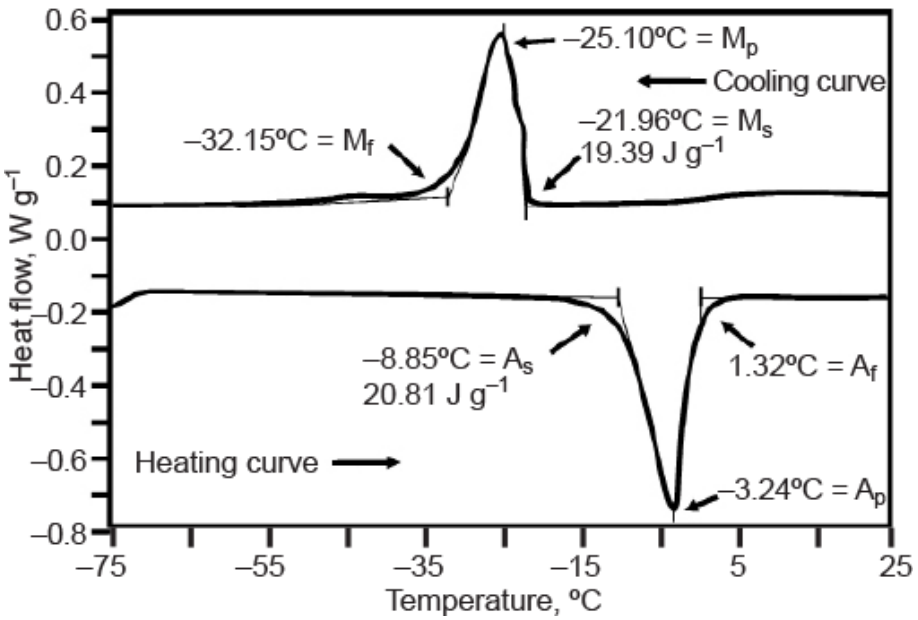

Fig. 2. 12 DSC Curve for NiTi alloy [29].

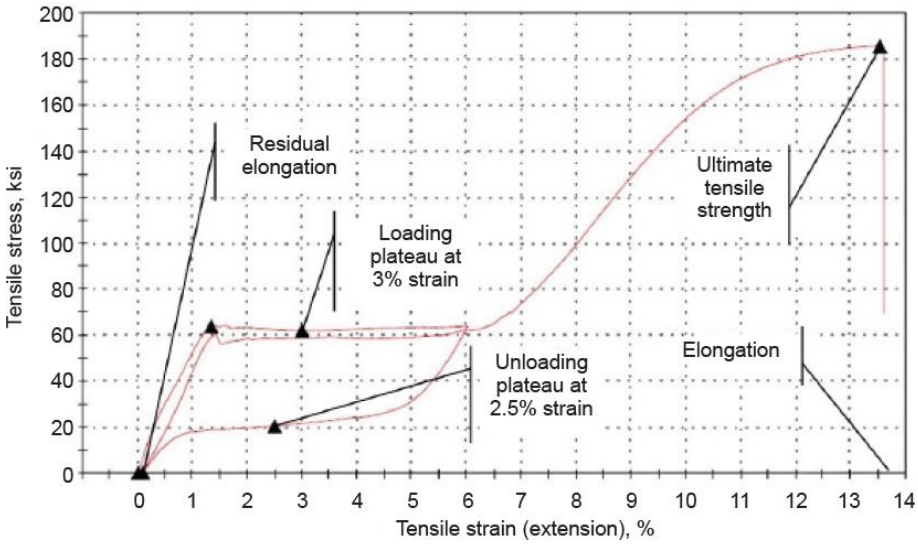

Fig. 2. 13 Typical Tensile Test for Nitinol [31].

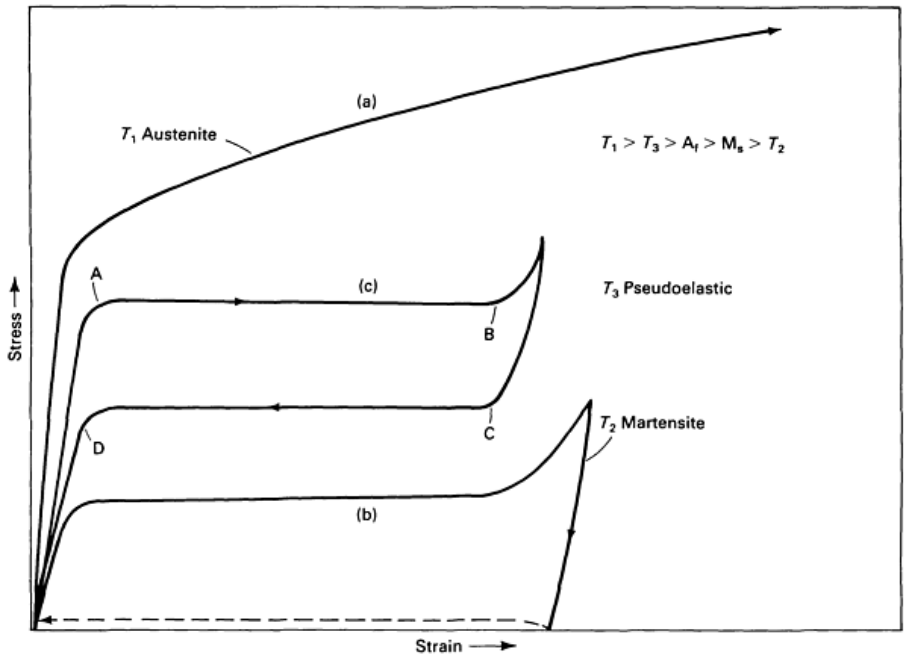

Fig. 2. 14 Typical stress-strain curves for: (a) Austenite. (b) Martensite. (c) Austenite and Stress-induced Martensite [2].

2.2.5 Applications

Nitinol SMA has been widely applied in such areas as biomedical, aviation, aerospace, and energy for its excellent mechanical properties, corrosion resistance, biocompatibility, and especially shape memory effect as well as superelasticity. Current applications include connecting fasteners, drive components, superelastic components, and shape memory alloy films. Among all fields, Nitinol is an outstanding leader in medical biomaterials and is widely used in clinical medicine and medical equipment, such as threads, orthodontic wires, cerebral

aneurysm clips, intramedullary needles, artificial joints, contraceptive rings, artificial hearts, artificial blood vessels, etc. have all entered medical clinical trials [32][8].

The following shows several categories of applications by properties:

1) Free Recovery

Free recovery means when an SMA component is deformed while martensitic, and the only function required of the shape memory is that the component returns to its previous shape after heating. The free recovery characteristic of Nitinol makes it extremely popular in interventional medical treatment. After pre-compression and deformation of various human body stents, they can be placed in human blood vessels, digestive tracts, respiratory tracts and other lengths through a small cavity. After the stents are expanded, they can support the narrow road in the body cavity. A representative example application with this property is the Simon filter, which was developed by M. Simon in 1989 and used for over three decades [33]. Fig. 2. 15 is a schematic of Simon filter; the Nitinol wire is shaped to be collapsed so as to suit the vein as Fig. 2. 15 (b), then return to Fig. 2. 15 (c) when it is inserted into the vein and gain heat. It is reliable, easy to use, can significantly shorten the treatment time and reduce the cost. Notably, Ti-rich Nitinol is more favorable for free recovery applications as it possesses much better shape memory property than Ni-rich Nitinol [12].

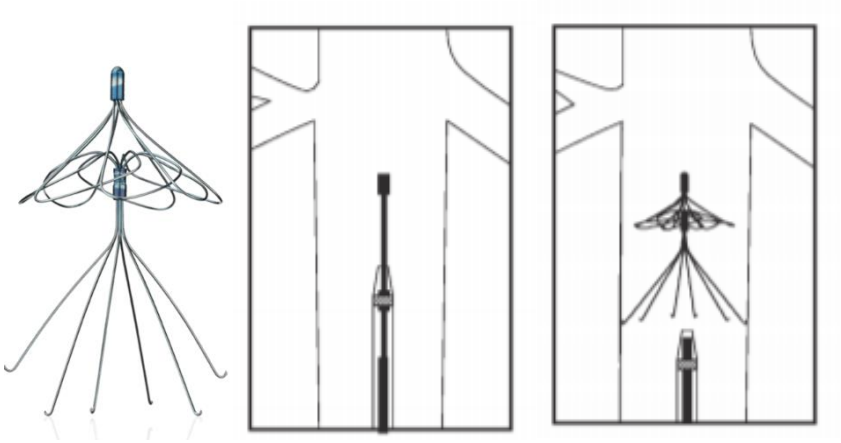

(a) (b) (c)

Fig. 2. 15 SIMON NITINOL® Vena Cava Filter [34].

2) Constrained Recovery

Compared with free recovery, constrained recovery takes advantage of the stress created as a component attempts to recover to its original shape while it cannot. The first significant

application for the Nitinol shape memory alloy is Cryofit hydraulic couplings, which was launched by Raychem Corporation of Menlo Park, CA [2]. As shown in Fig. 2. 16 [35], the CryoFit coupling is manufactured as a hollow pipe with a slightly smaller diameter than tubes. Its diameter is then expanded under cooled liquid nitrogen, and it will shrink and hold the tube strongly with warming up. Compared with traditional components, the Nitinol joint structure is more superficial, takes up less space, is easy to install, and has higher reliability.

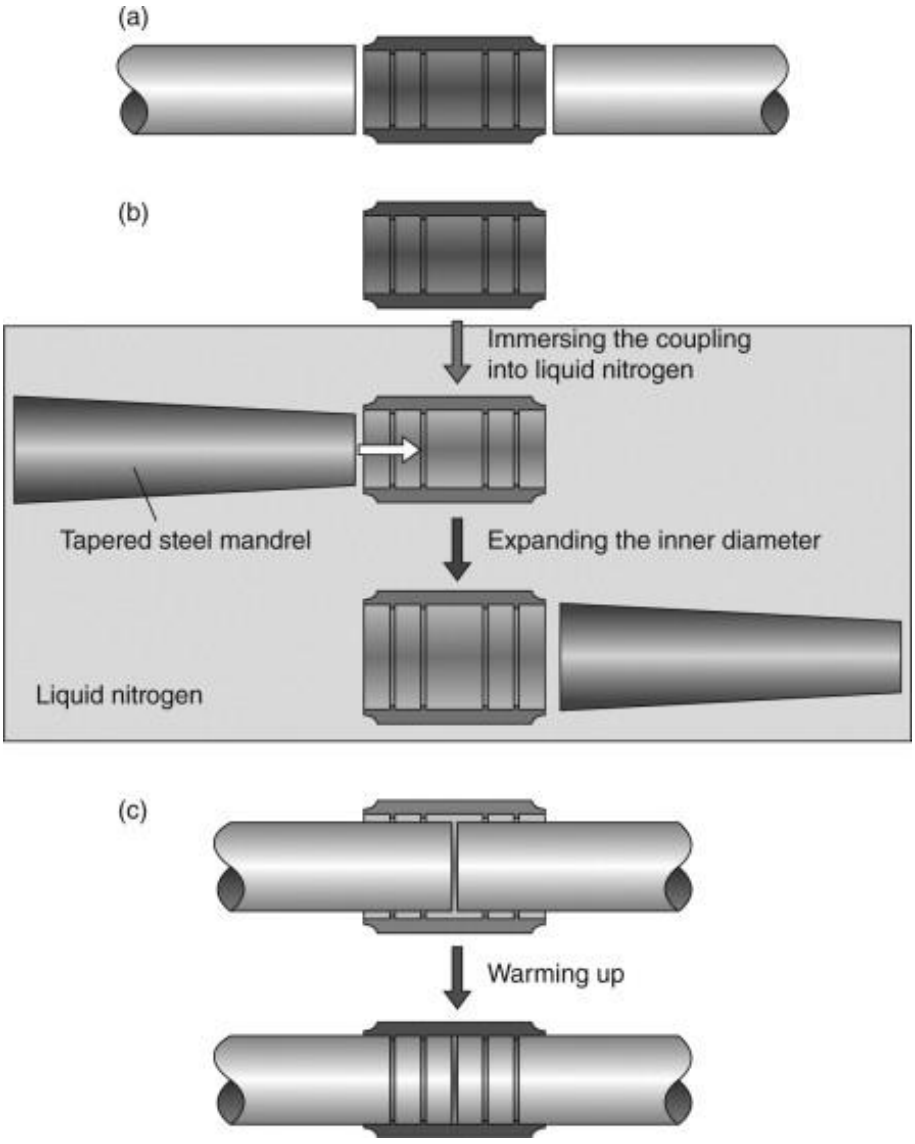

Fig. 2. 16 Schematic of CryoFit. (a) Coupling in austinite phase with original shape. (b) Coupling in the martensitic phase. (c) Coupling in austinite phase [35].

3) Force Actuators

In some applications, the Nitinol component is designed to exert force over a considerable range of motion, often for many cycles. These applications take advantage of the characteristic that the restoring force can do external work when the shape is restored after heating. Coil

spring actuator is such an application, and a typical Nitinol crystalline arrangement schematic is shown in Fig. 2. 17 [36]. In this actuation system, the spring is expanded when heating, while it shrinks when cooling. Such a spring actuator can be used in many applications in industry and aerospace, i.e., motor-gear train, small-scale robots, grippers and robotic hands [36]. The requirements for these applications are the ability to produce a large force per unit weight and the shape memory fatigue life.

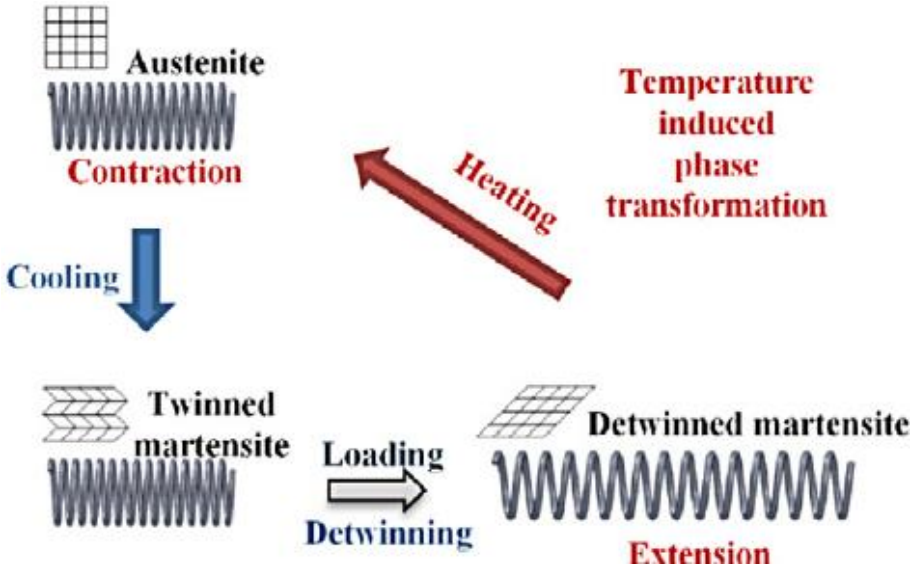

Fig. 2. 17 Nitinol coil spring actuator [36].

4) Superelastic Applications

At the temperature range from A_f to M_d, SMAs exhibit superelasticity, which can be seen as an extreme degree of elasticity. It is usually used in many applications that require superelasticity, including eyeglass frames, guidewires, stents, stylets, forming mandrels, stone retrieval baskets, and orthodontic files. Among these applications, arch wires for orthodontic correction by Nitinol have been applied for more than 30 years and have got rapid development [37]. Lock washers made by Nitinol can effectively solve the loosening problem caused by the decrease in the tightening force caused by vibration. It should be known that equiatomic Nitinol is hard to achieve superelasticity as their strength is relatively low [23]. Hence, Ni-rich Nitinol is frequently applied when superelasticity property is needed [38] [39].

5) Damping Applications

Shape memory alloy can also be used as an excellent damping material for structural vibration and shock absorption due to its high energy consumption during the cycle of loading and unloading. Fig. 2. 18 is a recentering Nitinol shape memory alloy damper, in which Nitinol

wires (inside the red oval) are utilized as energy dissipation components [40]. During the damper's service life, it is connected to another component via the connecting fitting and push-pull rod on both sides. Before applying, the prestrain of the superelastic Nitinol wires will be adjusted. The position of connecting fitting is fixed, while the push-pull rod is able to move relative to its connecting component. The status in Fig. 2. 18 is in its equilibrium position. Due to the Superelasticity of Nitinol wires and their prestrain, the push-pull rod is allowed to move in both left and right directions and return to its equilibrium position when the load is removed. During this cyclic process, the damper provides damping, attributed to the hysteretic property of the superelastic wires.

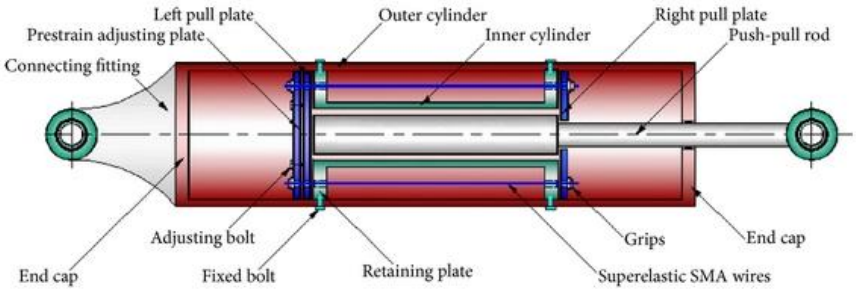

Fig. 2. 18 Diagram of a passive damper [40].

2.3. Effects of Post Process Heating Treatment on Microstructure and Properties

2.3.1 Heat Treatment and Corresponding Effects on Microstructure

There are specification requirements of shape memory and superelastic properties for medical and other applications of Nitinol shape memory alloys [41]. However, the composition of elements itself cannot control the functional properties due to the different phase compositions, microstructures, and phase element contents by different manufacturing processes. As discussed, the transformation paths and transformation products are affected by heat treatments. The solution annealed Nitinol transforms following one-stage transformation path B2–B19'. However, aging treatment introduces the intermediate phase R and changes B2–B19' path to a two-stage transformation path B2–R–B19'. Also, in some cases, R phase can show superior properties over martensite B19'. Heat treatment is hence introduced to improve and tailor the properties of Nitinol. In practice, Nitinol may be subjected to different types of heat treatments, depending on chemical composition, fabrication process, and intended application. These methods include mainly annealing, aging and "annealing+subsequent aging".

2.3.1.1 Annealing effect

Annealing / Solutionizing / Solution Annealing: In the broadest sense, annealing is the process of heating an alloy to an elevated temperature to promote a homogeneous equilibrium state, with microstructural defects and residual stresses are eased [42]. It includes "Solution Annealing" and "Stress Relief Annealing". "Solutionizing" or "Solution annealing" is a high-temperature heat treatment designed to put one or more constituents into solid solution, in order to remove precipitates [16]. Usually, for Nitinol heat treatments, "Annealing", "Solutionizing" and "Solution Annealing" can be used interchangeably. In this report, "Annealing" stands for "Solutionizing" and "Solution Annealing". The temperature range for annealing should be within the TiNi solid solution phase region in Fig. 2. 4 (the phase diagram of NiTi alloy), which should be higher than around 700 °C and lower than the melting temperature (around 1300 °C). On the other hand, "Stress Relief Annealing" is a low-temperature heat treatment for a short time. The aim is to release the residual stress.

Typically, L-PBF Nitinol SMAs have an inhomogeneous microstructure due to the rapid heating and cooling process during L-PBF. The inhomogeneous microstructure has detrimental effects on phase transformation and shape memory behavior of Nitinol SMAs. Annealing can lead to the dissolving of the secondary phases, which results in homogenous microstructure and thus lower transformation temperatures [20]. In addition, austenite is directly transformed into martensite during cooling and heating without the R phase after annealing.

2.3.1.2 Aging effect

Aging can strengthen Ni/Ti rich NiTi by promoting the precipitation of a dispersed Ni_3Ti_4 / $Ti_2Ni(O)$ phase throughout the matrix. Aging temperatures and aging times both control the microstructures of precipitates. Fig. 2. 19 are Transmission Electron Microscope (TEM) images of Ni rich NiTi samples aged at 450 °C for 1 h and 5 h, respectively. The lens-shaped precipitates are formed, and their average length increases with increasing aging time. Aging temperatures and times vary with the composition, fabrication process and the desired properties. Fig. 2. 20 is the TTT diagram for Ni52Ti48 alloy, which shows the upper-temperature limit for the Ti_3Ni_4 phase is 680 °C. Hence, the aging temperature should be below 680 °C from the point of view of physical metallurgy. In practice, the aging temperature is often set as 350°C to 600 °C [12] [43][44].

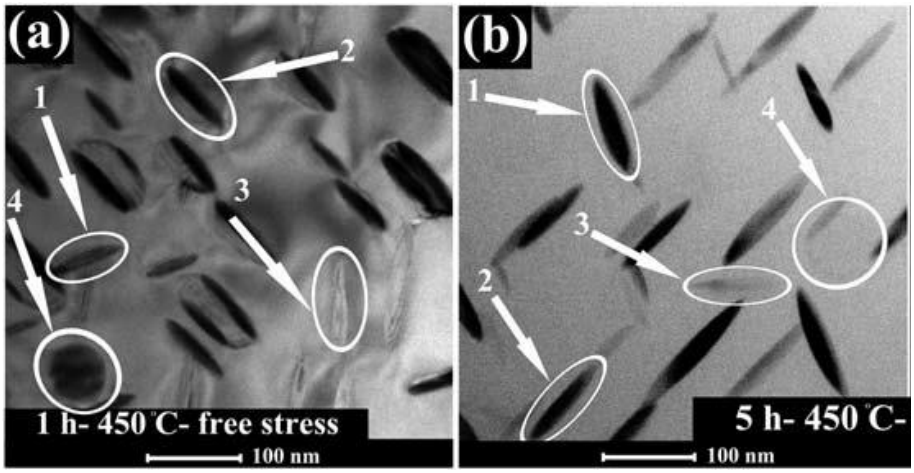

Fig. 2. 19 TEM images of NiTi sample aged at 450 °C for (a) 1 h and (b) 5h [45].

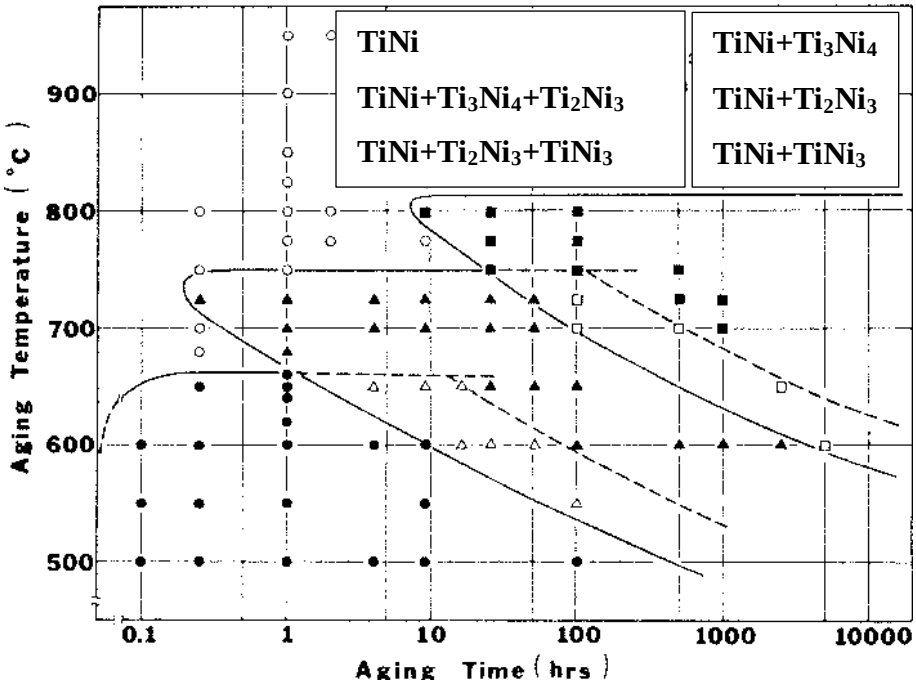

Fig. 2. 20 TTT diagram for Ni52Ti48 alloy as a function of aging temperature and aging time [15].

2.3.1.3 Annealing and Subsequent Aging Effect

Annealing is believed to provide a homogeneous equilibrium state, with microstructural defects and residual stresses are eased. Subsequent aging processes can lead to the precipitation of Ni rich phases (i.e., Ni_3Ti, Ni_3Ti_2, and Ni_4Ti_3) or Ti rich phases $Ti_2Ni(O)$. It is noteworthy that the proper annealing process helps release stress and homogenize defects, which can be the forming centers of precipitates. In the meantime, the composition, microstructure, distribution of precipitates, and the related properties are highly controlled by the subsequent aging process.

2.3.2 Transformation Temperatures

To ensure the Nitinol formulation, transformation temperatures are one of the recognizable characteristics. Many studies reveal that transformation temperatures are highly heat treatment dependent [20] [24]. Xu Huang et al. [46] study the effects of annealing temperature on the phase transformation behavior of Ni50.85Ti49.15 SMAs. They found that when the annealing temperature decreases, the temperature of R_s and R_f increases first and then decreases, reaching the maximum when annealing at 350°C. When the annealing temperature exceeds 650°C, the DSC results show that the R phase disappears and the austenite is directly transformed into martensite, and vice versa [46]. Andani, M.T et al. found that the transformation temperatures of Ni-rich Nitinol decrease upon annealing and subsequent water quenching [47]. In their study, Ni_3Ti_2, a metastable phase, dissolves during annealing and this prevents a further precipitation when water quenching is applied. Annealing also decreases the DSC peak width [47]. This phenomenon is confirmed by Saedi et al.[48][24]. Their results exhibit lower transformation temperatures (about 20 °C) and a single-phase transformation. Fig. 2. 21 demonstrates the DSC response of solutionized L-PBF Nitinol aged at different parameters. The results show that the transformation temperatures may increase with aging time, which could be caused by the evaporation of Ni in high temperature conditions for long duration, or the formation of Ni-rich phases at high temperatures. During heat treatment processes at high temperatures, Ti can react with oxygen, resulting in the reduction of Ti. Consequently, the transformation temperatures will decrease. This could further result in poor martensite to austenite transformations and an elevation in precipitate formation [49].

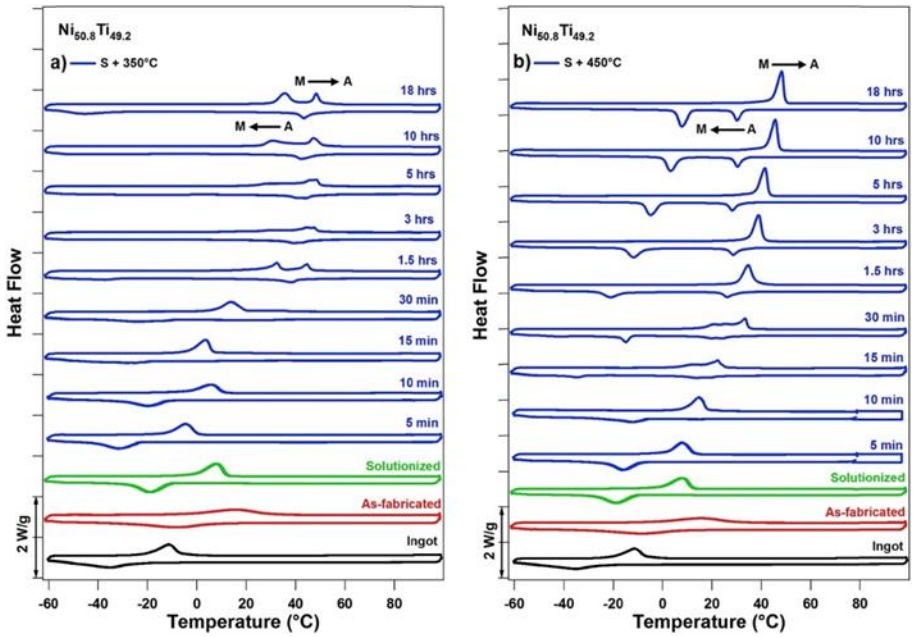

Fig. 2. 21 DSC response of solutionized L-PBF Nitinol aged at (a) 350 °C, (b) 450 °C with different aging time [24].

2.3.3 Shape Memory Effect

Shape memory NiTi has been widely used in many applications. However, Shape memory properties can be restrained by many detrimental factors caused by such as microstructural defects, dislocations, and precipitates. Hence, it is very desirable to optimize the degradation either by optimizing process parameters or by applying heat treatment. Fig. 2. 22 is a schematic diagram of typical stress-strain curve for a shape memory alloy, which shows the critical points of stress strain curve. Saedi et al. [24] compared the shape memory effect of solutionized L-PBF sample and "solutionized + aging" sample (Ni50.8Ti49.2) by compressive test (Fig. 2. 23). It can be observed that solutionized sample showed irrecoverable strain at 400 MPa while aged sample showed almost full recovery. Thus, can be concluded that aged sample has higher strength than the solutionized sample due to the precipitates hardening.

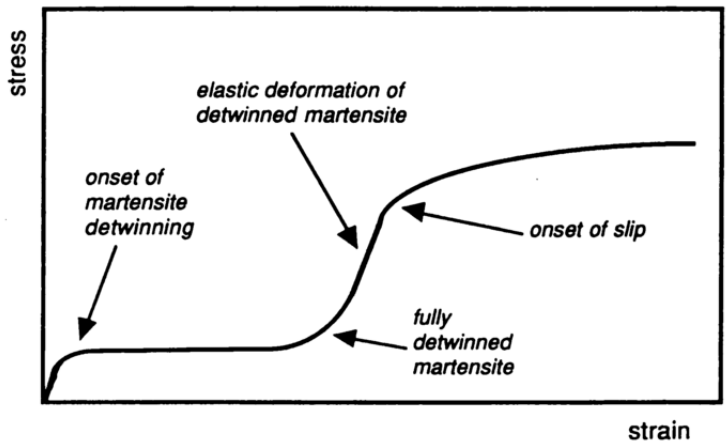

Fig. 2. 22 Schematic diagram of a typical stress-strain curve for a shape memory alloy [50].

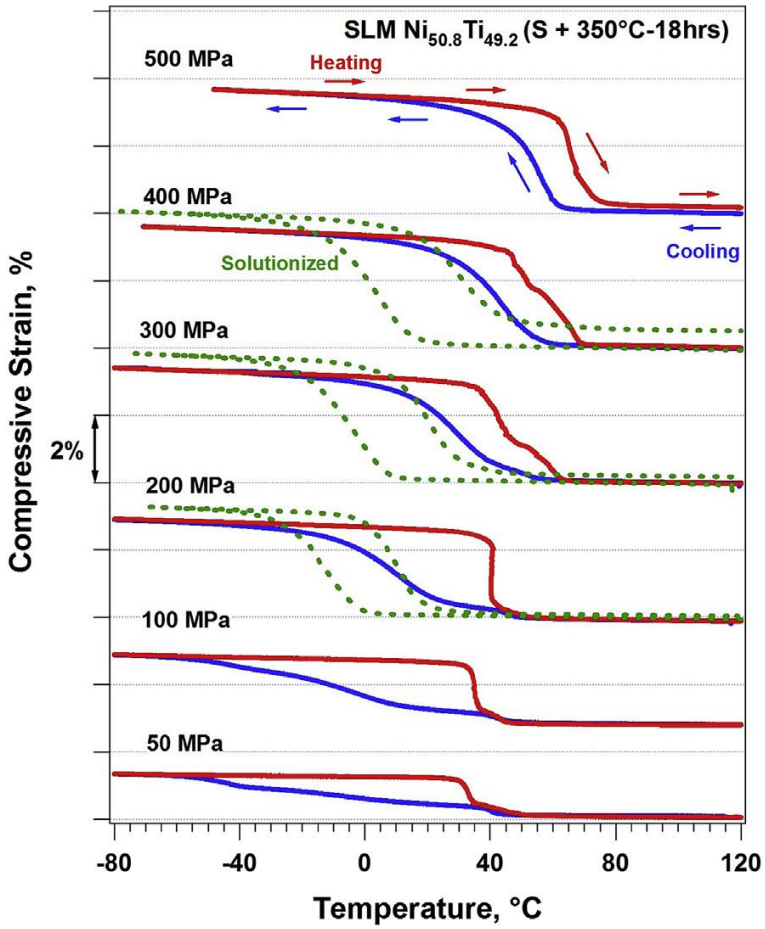

Fig. 2. 23 Thermal cycling under constant stress of solutionized (dashed line) and 18 h aged at 350 ℃ for L-PBF Ni50.8Ti49.2 [24].

2.3.4 Mechanical Properties

Heat treatments strongly influence the strength, including hardness and tensile strength of Nitinol, due to the precipitation processes occurring during heat treatment. However, heat

treatment may have different effects on the properties of Nitinol specimens with different compositions and fabrication processes. Hardness is a typical index of mechanical properties, and it is also essential for quality control in the production process. Also, hardness is the easiest evaluation method. Saedi et al. [24] conducted a Vicker's hardness tests on L-PBF Nitinol, and the authors found that the hardness value of L-PBF Nitinol specimen (224 HV is much lower than that of the ingot (278 HV). This can be explained by the microstructure change during the heating and cooling process of L-PBF. Their results also show an increased hardness value (288 HV) by solution annealing. The increase of hardness value after solution annealing is ascribed to the dissolved Ni_4Ti_3 precipitates. Another heat treatment process (annealing+ aging for 18 h at 350 °C) exhibits a much higher hardness value of 345 HV. The hardness values of the specimen upon different conditions are shown in Fig. 2. 24. Saedi et al. also conclude that annealing and subsequent aging increase the yield stress value by the age-hardening effect.

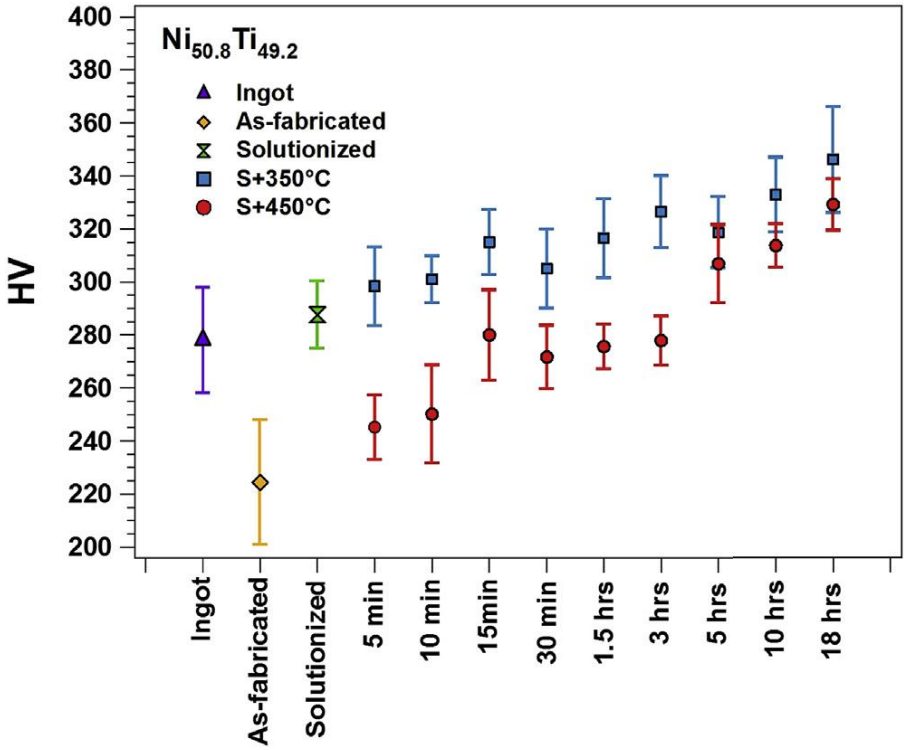

Fig. 2. 24 Vicker hardness of L-PBF Ni50.8Ti49.2 at different conditions [24].

2.3.5 Summary Chart of Heat Treatment Parameters and Corresponding Effects on the Transformation Behavior and Properties:

Table 2. 3 is a summary chart of heat treatment parameters and corresponding conclusions from relevant literature sources. In summary, annealing can homogenize the microstructure, and

hence improve the shape memory property of Nitinol. Aging can promote the formation of precipitates in order to facilitate the strength and superelasticity of L-PBF Nitinol. Nevertheless, there is no positive correlation between shape memory property and annealing temperatures and times. Similarly, higher aging temperatures and longer time do not certainly achieve better strength and superelasticity. Hence, optimization of the proper heat treatment parameters and studying the underlying mechanisms is necessary.

Table 2. 3 Heat treatment parameters and its effects

Sl. No.	Composition	Annealing Temperature	Aging	Effect in transformation behavior
1	Ni50.8Ti49.2	950 °C for 5.5h and water quenching (WQ)	350 °C and 450 °C for 5min–18h and WQ	Annealing and aging can improve the superelasticity of Nitinol. 350 °C aged sample shows better superelasticity than 450 °C aged one. The aged sample has higher strength than the solutionized sample [24].
2	Ni50.8Ti49.2		350 °C to 600 °C for 30 min–18h and WQ	A_f increased when samples are aged up to 500 °C and intermediate R-phase occurred. Aging alone can improve the L-PBF Nitinol superelasticity and shape memory properties [51].
3	Ni50.2Ti49.8	830 °C for 25min and furnace cooling		Annealing annihilates L-PBF stress-induced martensite plates, and causes a mixed shape memory response [32].
4	Ni50.16Ti49.84		400 °C for 5min and WQ	Aging can achieve higher transformation strain and recovery percentage for L-PBF Nitinol [4].
5	Ni50.8Ti49.2	1050 °C for 4 h and WQ	400 – 500 °C for 1–2 h and WQ	Annealing and aging can enhance shape memory properties and reduces A_f for combustion synthesis Nitinol
6	Ti50.5Ni49.5	400 – 800 °C for 30 min and WQ*		Ti_2Ni precipitate forms in Ti-rich NiTi alloys. The size, numbers and distribution of precipitates can be controlled by heat treatment [53].
7	Ni50.9Ti49.1		580 – 600 °C for 1h and WQ	Proper aging temperature can improve the strength of Nitinol [43].

** The annealing temperature is lower than the NiTi solid phase formation temperature. Hence, annealing in these cases belongs to stress relief annealing rather than solution annealing.*

2.4. Conclusions

The key findings of this literature review are summarized as follows:

1. Nitinol shape memory alloys produced by different manufacturing technologies possess distinguishing transformation temperature, shape memory and mechanical properties. Among different manufacturing technologies, L-PBF contributes to achieving near net shape and complex geometric Nitinol devices.

2. Composition, L-PBF parameters and post-heat treatment can control functional and mechanical properties of Nitinol shape memory alloys by influencing microstructures (e.g., precipitations, grain shape, size). However, the relationship among composition, L-PBF parameters, post-heat treatment and functional properties still need to be understood.

3. In general, Ni-rich Nitinol has better superelastic property, while near equiatomic and Ti-rich Nitinol show better shape memory property. The as-fabricated material for this experiment is near equiatomic Nitinol; hence the result is expected to evaluate mainly by shape memory response.

4. Proper annealing and aging processes can significantly improve the superelastic property and shape memory property. One of the biggest challenges is how to develop proper heat treatment procedures to obtain the desired properties.

5. Annealing, aging, and (annealing + aging) are selected to study their effects on the properties of equiatomic L-PBF Nitinol. Table 2. 4 is the estimated heat treatment processes for experiments. These heat treatment parameters are selected from the relevant literature in order to compare and optimize. The expected effects on the properties of equiatomic L-PBF Nitinol are also shown.

6. Residual stress and dislocations exist on as-fabricated L-PBF Nitinol. Annealing can improve the shape memory property by removing these residual stress and dislocations. Aging can facilitate the strength and the thermomechanical stability of L-PBF Nitinol by promoting the formation of precipitates. Besides, although superelasticity cannot be observed in equiatomic Nitinol due to its low strength, L-PBF process may create locally constituent fluctuations and precipitates in equiatomic Nitinol. Heat treatment may improve the strength of L-PBF equiatomic Nitinol by changing the distribution of precipitates and its microstructures. Hence, there is a possibility to achieve the superelasticity property on L-PBF equiatomic Nitinol by applying proper heat treatment.

Table 2. 4 The overview of selected post heat treatment parameters

Heat Treatment (HT) type	**Annealing**	**Aging**	**The Origins of Parameters**
HT1	950 °C for 5.5h and WQ	350 °C for 18h and WQ	Proper parameters for L-PBF Ni50.8Ti49.2 [24]
HT2	950 °C for 5.5h and WQ	450 °C for 10h and WQ	Proper parameters for L-PBF Ni50.8Ti49.2 [24]
HT3	830 °C for 25min and furnace cooling at 10 °C/ min		Proper parameters for L-PBF Ni50.2Ti49.8 [32]

2.5. Research Objectives

Based on the findings of this literature review, research objectives are established as follows:

1. Study the microstructure and precipitate behaviors of L-PBF Nitinol alloys.

2. Optimize heat treatment process, improving thermal stability and shape memory effect of L-PBF Nitinol alloys.

3. Provide a link between the microstructures, phase transformation behaviour, mechanical properties, and shape memory response of as-processed and post heat treated L-PBF Nitinol alloys.

Chapter 3 Materials and Methods

3.1 Material

The material investigated herein is Ni50Ti50 (atomic %) manufactured via L-PBF [28]. The NiTi samples were fabricated using an Aconity3D Midi (Aconity3D GmbH, Germany) machine equipped with a laser source featuring a maximum power of 1000 W and a beam with a Gaussian distribution. The scanning electron microscopy (SEM) image of the NiTi powder used is shown in Fig. 3. 1 a. A bidirectional scanning strategy was implemented for fabricating cylindrical samples (diameter of 13 mm and height of 25 mm) (Fig. 3. 1 b). L-PBF process parameters such as laser power, scanning velocity, hatch distance, etc. used in this study are provided in Table 3. 1. The samples for microstructure characterization (Hardness, Optical Microscopy, Scanning Electric Microscopy, X-Ray Diffraction) and mechanical tests were separated via electrical discharge machining (EDM) (Table 3. 2.).

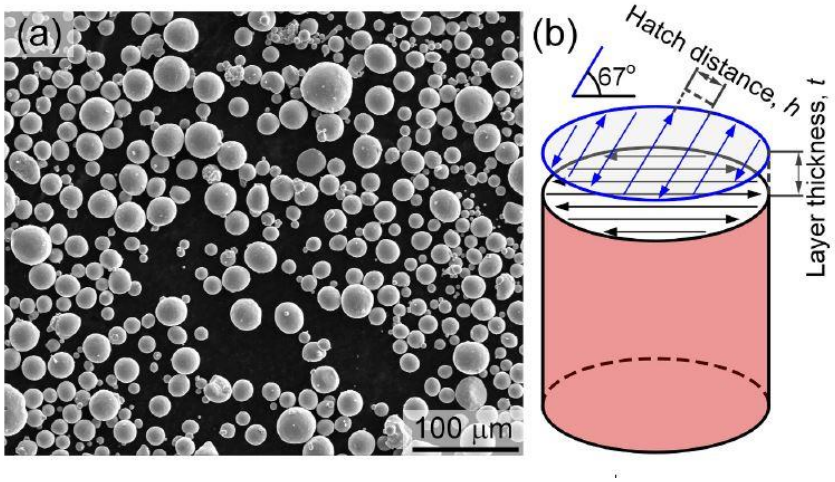

Fig. 3. 1. (a) SEM of the commercial Nitinol powder and (b) the schematic of the applied scanning strategy [28]

Table 3. 1 L-PBF process parameters

	Laser Power (W)	Scan velocity (mm/s)	Hatch distance (mm)	Layer thickness (mm)	Laser beam diameter (µm)	Volume energy density (J/mm)
A1	250	1250	0.1	0.03	80	67
A2	250	1250	0.12	0.03	80	56
A4	250	800	0.12	0.03	80	87

A6	250	500	0.14	0.06	80	56

Table 3. 2 Sample sizes for different tests

	Diameter (mm)	Height (mm)
Hardness/OM/SEM/XRD	13	1
DSC	5	1
Mechanical testing	5	20

3.2 Post heat treatments

As summarized in Table 2.4, three different post heat treatment conditions were applied to optimize heat treatment parameters. As fabricated samples were used as reference samples for comparisons with the post heat treated samples. HT1 and HT2 consist of a combination of solution annealing and aging treatment. For solution annealing process, the samples were kept at 950 °C for 5.5 hours followed by WQ for both HT1 and HT2. Subsequently, the solutionized samples were aged at 350 °C for 18 hours and 450 °C for 10 hours for HT1 and HT2, respectively, and followed by WQ. For HT3, the samples were hold at 830 °C for 25 min followed by furnace cooling at 10 ^{o}C/ min to room temperature. Based on the primary optimization, solutionized samples (950 °C for 5.5 hours & WQ) were aged at 350 °C for different time &WQ to optimize the aging time (HT4/5/6). Also, solution annealing (HT7: 950 °C for 5.5 hours & WQ) and aging (HT8: 350 °C for 18 hours & WQ) were implemented individually to further study the effects of different heat treatments on shape memory behaviors of L-PBF NiTi. The overview of post heat treatments is shown in Table 3.3. In addition, more optimization trials are given in Appendix A.

Table 3.3 The overview of the post heat treatments

Post Process Heat Treatment (HT)	Annealing	Aging
HT1	950 ^{o}C for 5.5h and WQ	350 ^{o}C for 18h and WQ
HT2	950 ^{o}C for 5.5h and WQ	450 ^{o}C for 10h and WQ
HT3	830 ^{o}C for 25min and furnace cooling at 10 ^{o}C/ min	

HT4/5/6	950 °C for 5.5h and WQ	350 °C for 30min / 9h / 27h, respectively; followed by WQ
HT7	950 °C for 5.5h and WQ	
HT8		350 °C for 18h and WQ

3.3 Microstructural Analysis

Samples mounted in conductive resin were polished to a mirror finish prior to measurements. A scanning electron microscope (SEM, JEOL JSM 6500 F) equipped with dispersive X-ray spectroscopy (EDS) analyzer was used to measure the precipitates. For metallographic examination, the mirror finish samples were further color-etched according to the procedure used by Therese Bormann et al. [54]. The etching solution consisted of 120 ml pure water, 15 ml HCl (Merck), 15 g $Na_2S_2O_5$ (Fluka), 10 g $K_2S_2O_5$ (Merck) and 2 g NH_4HF (Sigma-Aldrich). The etched microstructures were then examined via a Leica DMI 5000 optical microscope under the polarized light mode. For Vickers hardness measurements, a Durascan microhardness tester (Struers) was used. Polished samples were applied a main load of 2kgf with loading time 10s. An average of 10 hardness values for each sample were reported. The indents were made at 2mm distance with series measurement.

TEM images were taken by a FEI cubed titan Cs-corrected 80-300 kV TEM equipment. The instrument was operated in STEM mode and in brightfield mode. At the same time elemental maps were also made. Pre sample preparation consisted of cutting and sawing a cylinder of the material followed by mechanical polishing to around 20 μm thickness. The harsher sample preparation procedures before STEM-analysis includes punching 2.3 mm discs and gluing this on a 3 mm Cu ring, and the subsequent Ar ion milling to electron transparency.

XRD analysis was carried out for phase identifications and phase fraction calculations in the as fabricated and post heat treated samples. The measurements were carried out using the Bruker D8 Advance diffractometer in Bragg- Brentano geometry and Lynxeye position sensitive detector using a Cu-Kα radiation. The step size used was 0.03° 2θ with 45 kV and 40 mA current in a 2θ range of 17°–120° and scatter screen height of 5 mm.

3.4 DSC Measurements

Phase transformation behavior was analyzed by a differential scanning calorimetry (DSC, Perkin Elmer DSC 800) in a nitrogen atmosphere, with a cooling and heating rate of 10 ºC /min over a temperature range of -70 ºC to 200 ºC. The temperature-time profile was given in Fig. 3. 2. The samples were polished to establish good thermal contact. On the calorimetric graph, phase transformations are depicted as peaks and the areas under those peaks indicate the energies of transformations. TTs measured as the intersection of the baseline and the maximum gradient line of a transformation peak as shown in Fig. 2. 12.

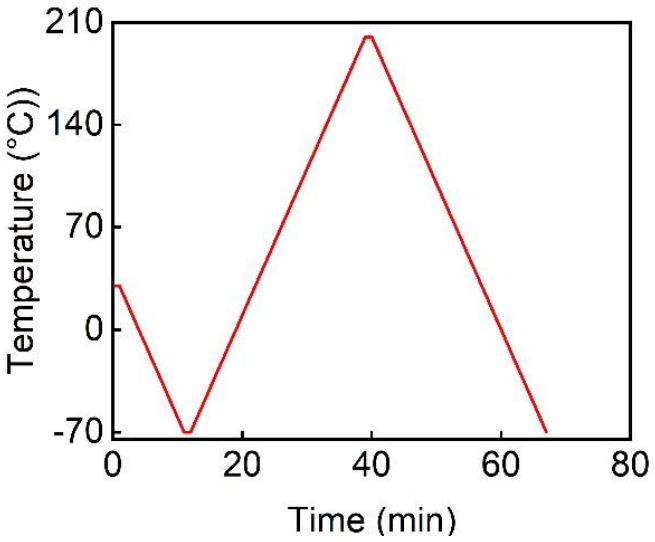

Fig. 3. 2 Temperature-Time profile for DSC measurements

3.5 Mechanical Testing

Compression tests were conducted by a 24 kN MTS Landmark servo-hydraulic test platform (Fig. 3. 3). A strain rate of 10^{-4} sec^{-1} was employed during loading while unloading was performed under force control. The strain was measured by a ceramic rod extensometer with a gage length of 10 mm, which was attached to the samples. The samples were heated up using an induction coil and cooled via three air blowing nozzles. The temperature was monitored by a thermocouple contacted to the sample. A 3-step gradually increasing strain level test was applied to investigate the critical stress for phase transformation and strain recovery (see Fig. 3. 4 a). A "hard" cyclic test (50 cycles with a fixed maximum 4% strain) aimed to observe the cyclic stability of samples (Fig. 3. 4 b).

The flowchart of the experimental design is shown as Fig. 3. 5.

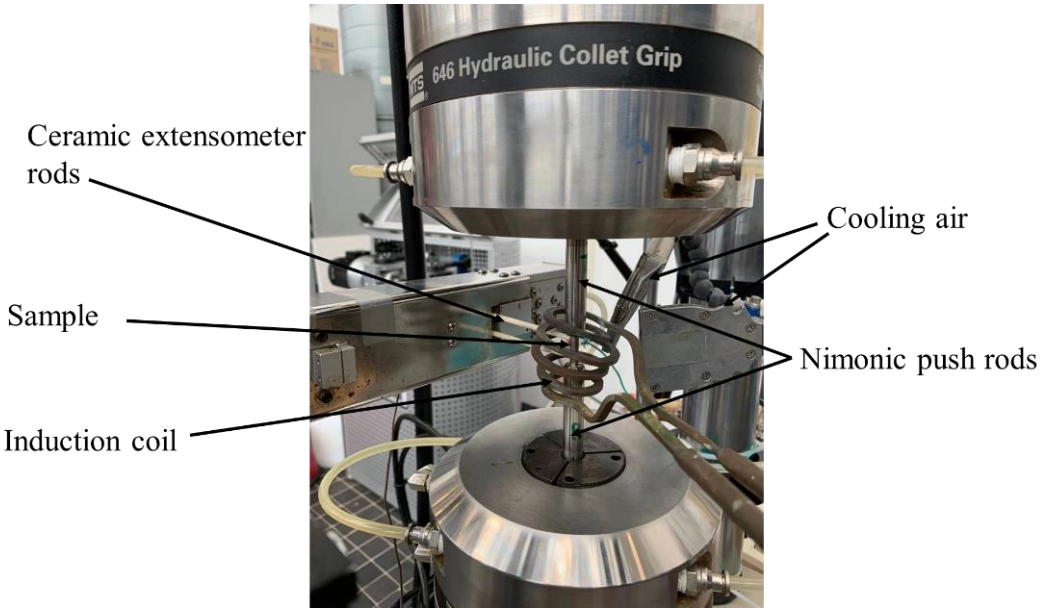

Fig. 3. 3 The setup for compression tests.

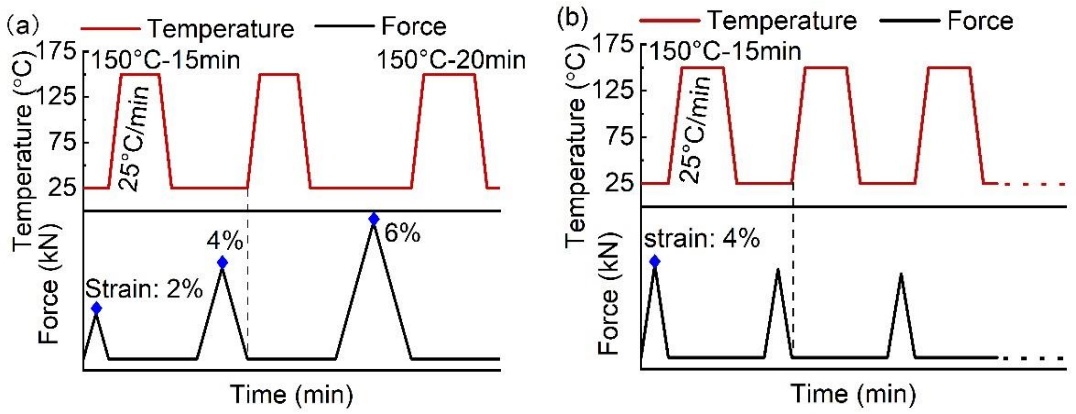

Fig. 3. 4 . Temperature & Force profiles as a function of time for gradually increased strain level test (a) and cyclic stable strain level test (b).

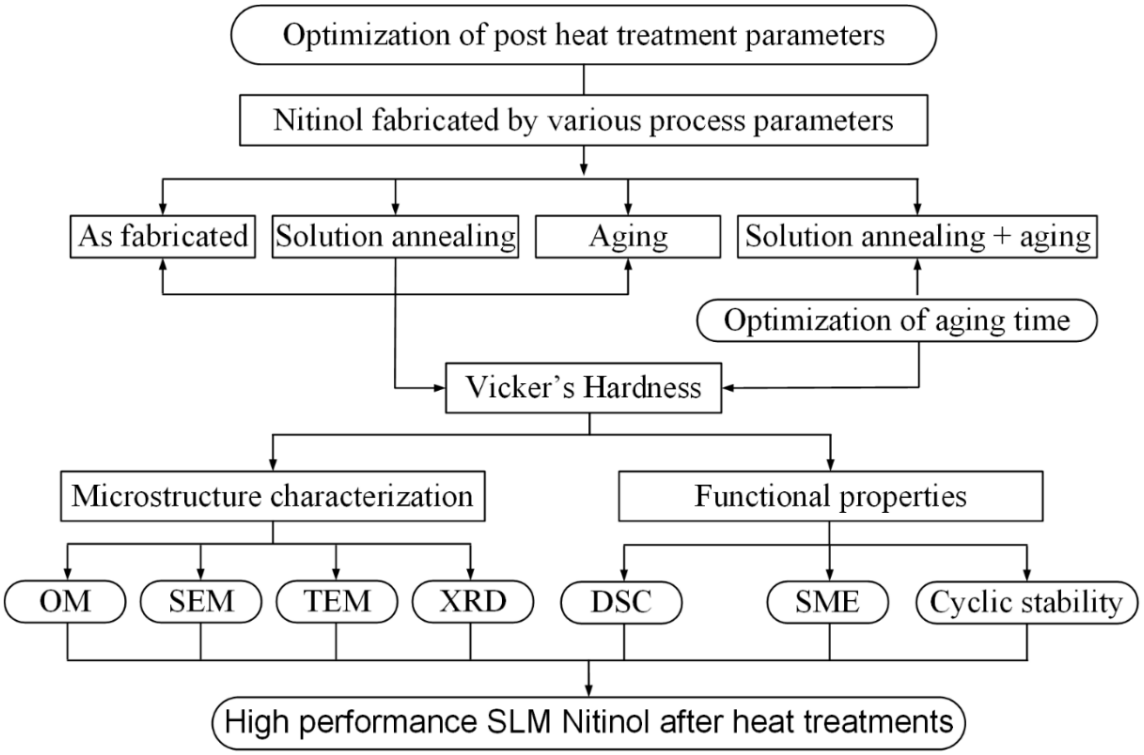

Fig. 3. 5 The flowchart of experimental design

Chapter 4 Optimization of post heat treatment parameters

4.1 Microstructure evolution after post heat treatment

4.1.1 Microstructures of L-PBF as-processed samples

The microstructure of L-PBF NiTi samples depends on L-PBF process parameters including powder size, layer thickness, etc [12]. L-PBF fabricated samples A1, A2, A4 and A6 featuring the same composition and four typical microstructures are selected in this work [5]. Fig. 4. 1 shows the optical micrographs of fabricated A1, A2, A4 and A6 samples from the top surfaces and cross sections. A characteristic checker grain structure is observed on the surface of all samples, while cross section view exhibits columnar structure. Grain sizes of these samples were calculated by ImageJ (Table 4. 1). The width of the grains of as fabricated sample is close to or slightly less than the hatch spacing value, which is 100, 120, and 140 μm, respectively (Table 4. 1 and Table 3. 1). The grain width of this work is in agreement with the conclusion that grain width should not be larger than hatch spacing [12], [54]. Fig. 4. 1(a) demonstrate squared like grains from surface of as-fabricated A1. A2 shows a good structure without obvious cracks and pores (Fig. 4. 1(b)). Fig. 4. 1(c) gives the microstructures of A4, which reveals slightly macroscopic defects. Keyhole-induced pores can be observed in both views for A6 (Fig. 4. 1(d) & (h)).

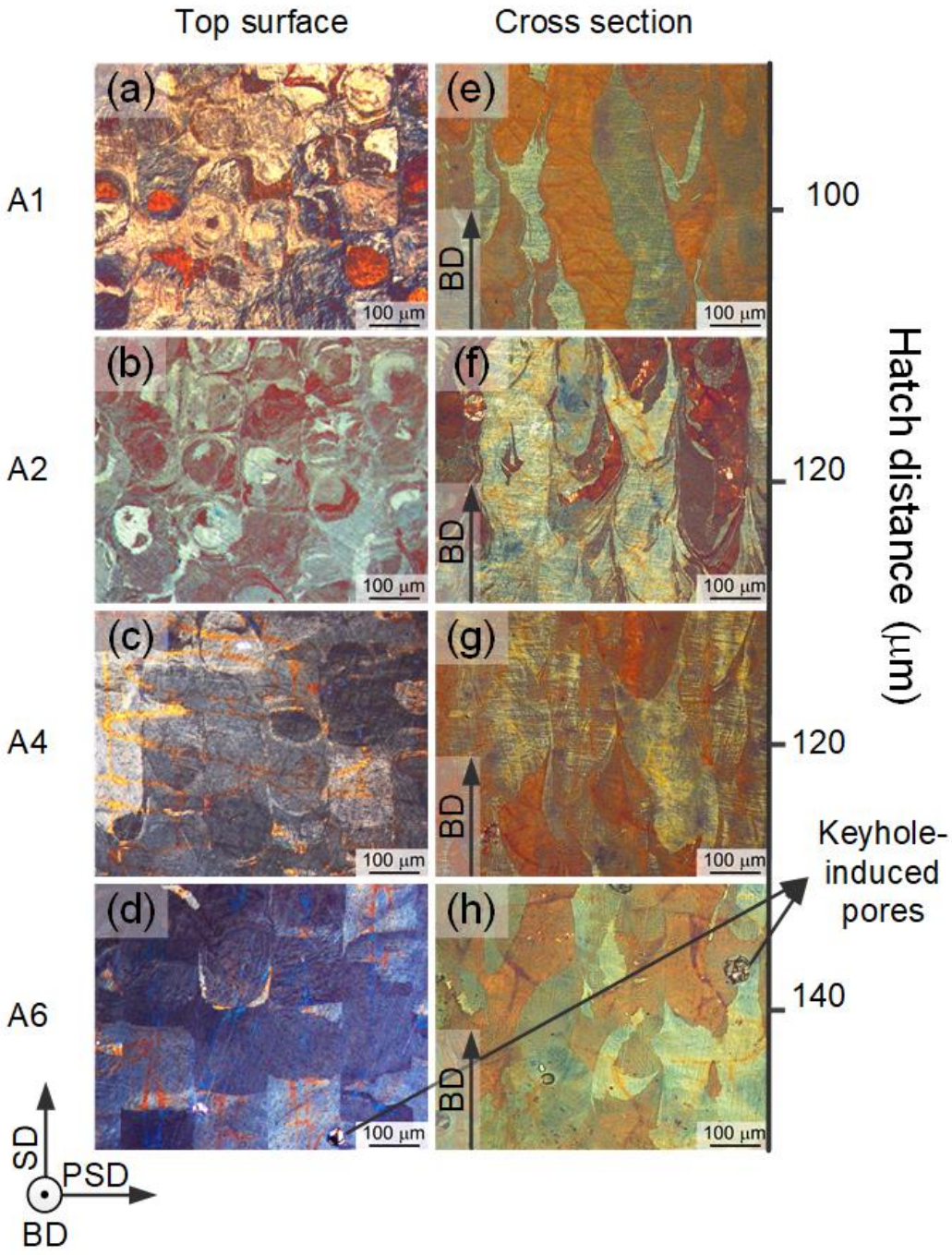

Fig. 4. 1 Optical microscopy images of top surfaces and cross sections for as-processed samples: (a) and (e) A1; (b) and (f) A2; (c) and (g) A4; (d) and (h) A6.

Table 4. 1 Grain size of as-processed samples

Sample type	Grain size in the scanning direction (μm)	Grain size in the perpendicular direction (μm)
A1	102 ± 0.5	100 ± 1.5
A2	120.2 ± 3.2	116.3 ± 0.5
A4	150 ± 2	119 ± 0.6
A6	144 ± 0.8	140 ± 0.4

4.1.2 Microstructure after post heat treatment

Fig. 4. 2-5) compare microstructure of heat treated samples with as fabricated ones for A2, A1, A4 and A6 (see appendix B for lower magnification), respectively. It can be observed that heat treatment process had no significant influence on grain structures for all four L-PBF fabricated conditions. For example, Fig.4. 2 shows the optical micrograph of as fabricated A2 sample. Micrographs of samples treated by HT1, HT2 and HT3 are also given in Fig. 4. 2. The grain sizes are given in Table 4.2. HT3 did not significantly alter grain size, while HT1 and HT2 elongated the grains in the perpendicular scanning direction. However, the grain size remained similar to the as fabricated condition in the scanning direction. This corresponds to the conclusion that the grain width cannot be increased beyond the hatching space [12]. It should be noticed that the grain size may influence the transformation temperature with a relatively smaller impact factor [55].

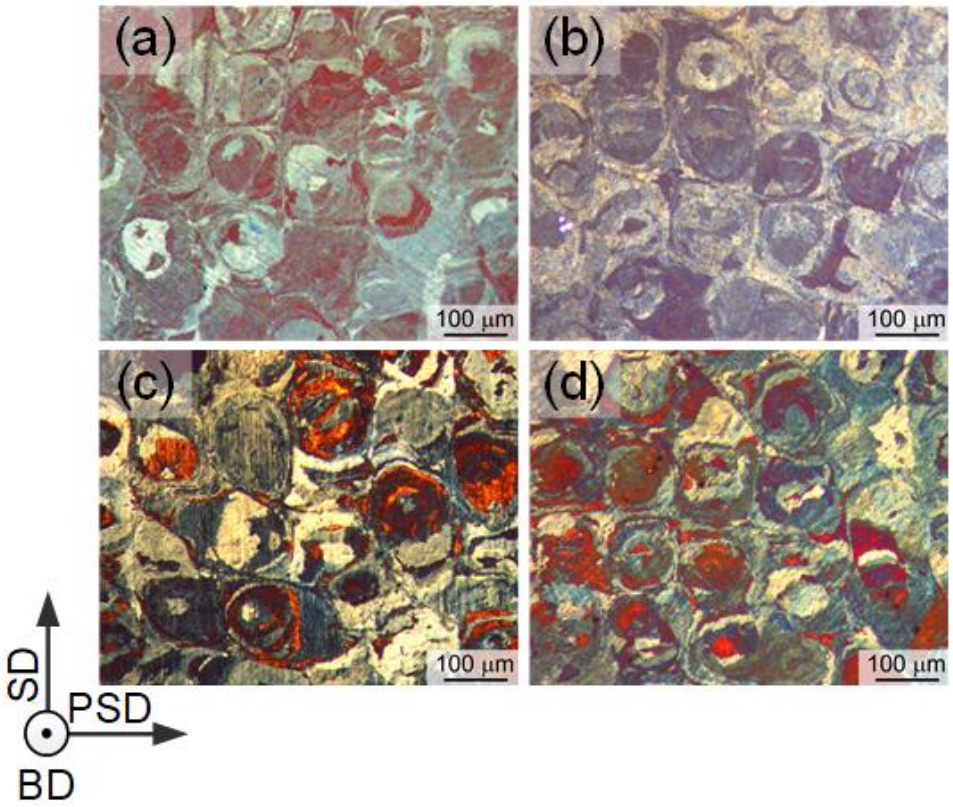

Fig. 4. 2 Optical microscopy images of top surfaces for A2: (a) As fabricated; (b) HT1; (c) HT2; (d) HT3.

Table 4. 2 Comparison of grain sizes before and after heat treatments

HT conditions	Size in the scanning direction (μm)	Size in the perpendicular direction (μm)
As fabricated	120.2 ± 3.2	116.3 ± 0.5
HT1	140 ± 0.6	118 ± 0.5
HT2	134.2 ± 1.2	121 ± 0.4
HT3	122 ± 0.8	117.1 ± 1.2

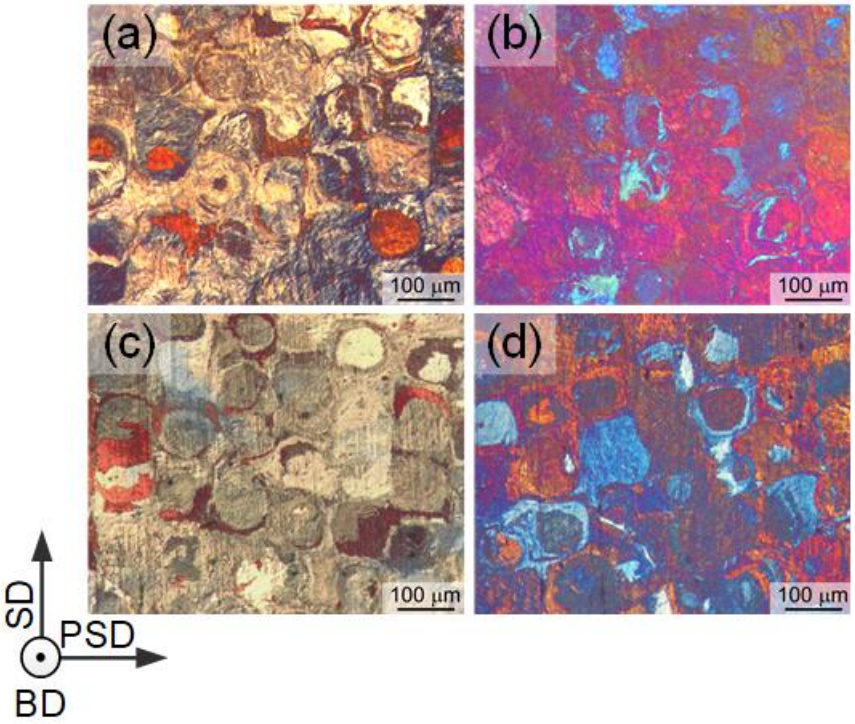

Fig. 4. 3 Optical microscopy images of top surfaces for A1: (a) As fabricated; (b) HT1; (c) HT2; (d) HT3.

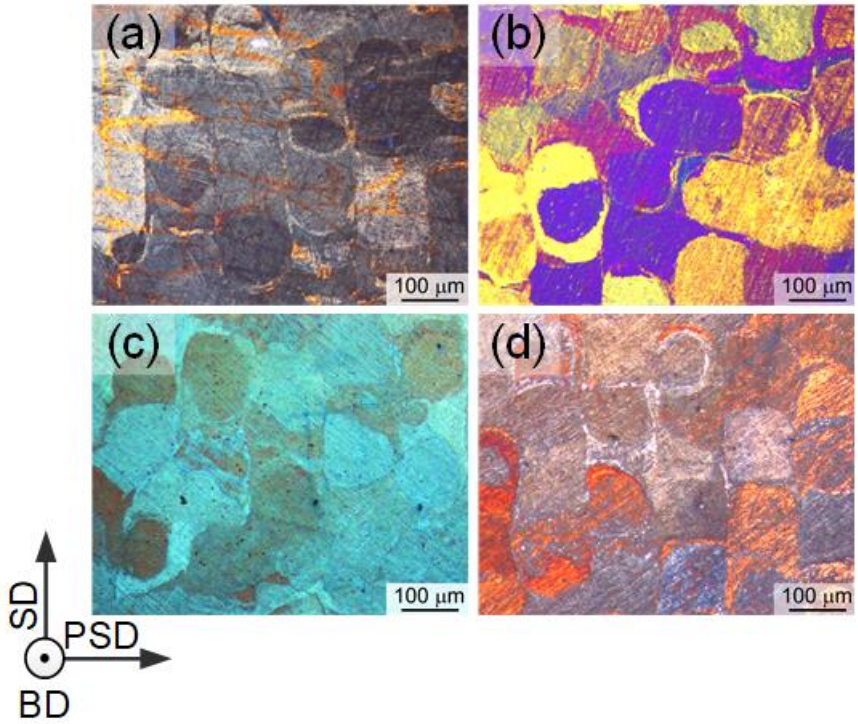

Fig. 4. 4 Optical microscopy images of top surfaces for A4: (a) As fabricated; (b) HT1; (c) HT2; (d) HT3.

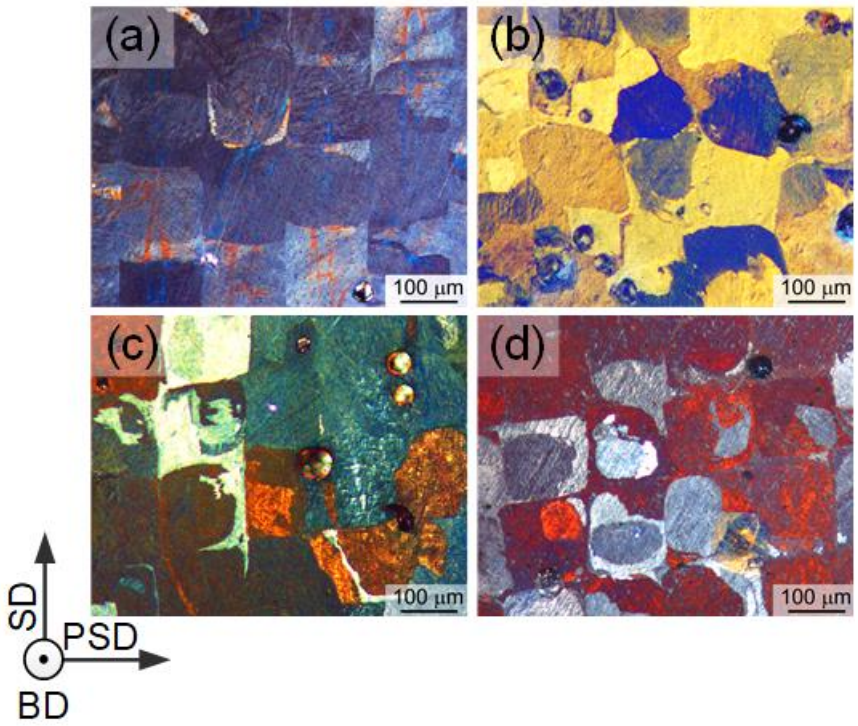

Fig. 4. 5 Optical microscopy images of top surfaces for A6: (a) As fabricated; (b) HT1; (c) HT2; (d) HT3.

4.2 Effect of heat treatment on hardness

Vicker's hardness of A1, A2, A4 and A6 samples with and without various heat treatments is shown in the Fig. 4. 6. As seen hardness values of A2 treated by HT1 condition shows a drastic increase, compared to A1, A4 and A6. This trend implies that HT1 has the most significant effect on the strength of A2. Hence, further characterization tests and mechanical measurements are applied to A2 under the HT1 condition. To understand the effect of aging on A2 sample, the aging time needs to be further optimized.

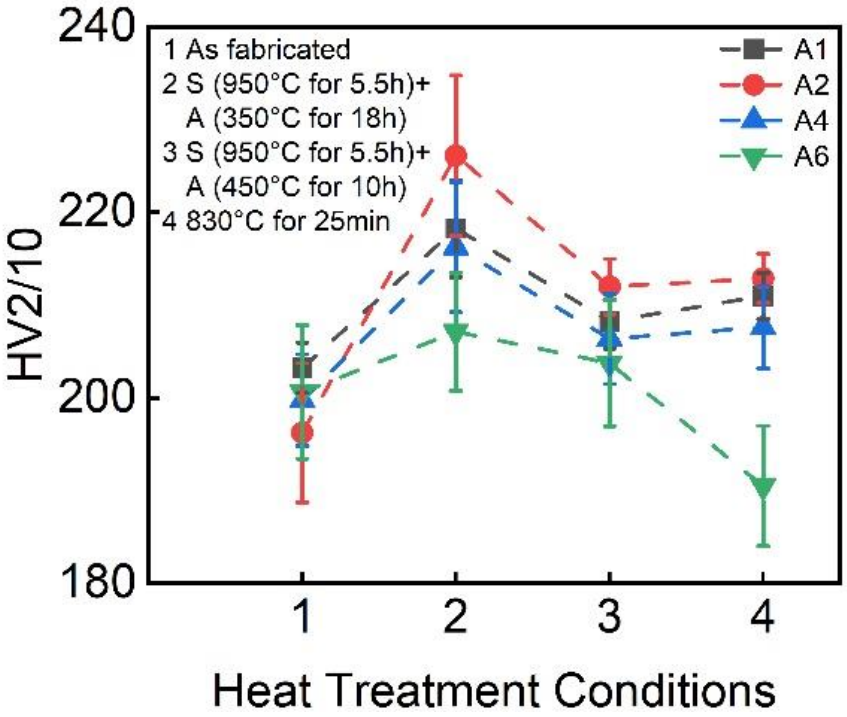

Fig. 4. 6 Vickers hardness of A1, A2, A4, A6 as function of heat treatment conditions: 1. As fabricated; 2. HT1; 3. HT2; 4. HT3.

4.3 Effect of aging in solutionized L-PBF NiTi

4.3.1 Microstructure and hardness

To elucidate second phase precipitates in as fabricated sample, TEM study was performed on as fabricated A2 sample. For the first measurement, HREM image shows that planes in different directions are present (Fig. 4. 7). Spacings between planes can be attributed to TiO_2, but the angles between planes cannot, and composition is close to Ti_2O. However, elemental EDX map exhibits the chemical distribution, indicating the dark spherical particles in the bright-field TEM image are pure Ti particles during another measurement (Fig. 4. 8). Hence, the second phase in as fabricated sample may be a mixture of TiO_2 and pure Ti. TEM images are also taken for the solution annealed sample, the twin martensite structure can be observed, and the dislocation density is relatively high around the precipitates (Fig. 4. 9). The high dislocation density is one of the reasons that solution annealed sample revealed high peak stress and better cyclic stability than as fabricated sample, which will discussed in detail in the next chapter. The fast Fourier transform (FFT) patterns shows that the particle is cubic $Ti_2Ni(O)$ (Fig. 4. 10). In addition, the phase evolution of Ni50Ti50 (at. %) was calculated by Thermo–

Calc software (Fig. 4. 11). It is found that, Ti fraction in liquid phase increased with the solidification. Therefore, more Ti solutes segregate to grain boundaries at the terminal solidification stage (0.9–1.0 residual liquids at this stage), which can promote Ti_2Ni (a Ti–rich precipitate) formation.

Fig. 4. 12 illustrates the SEM images of top surfaces of solutionized samples aged for different time durations. It is known that the spatial resolutions of EDS measurements are about 1 μm for SEM [56], while the average size of the particles is around (37 ± 7) nm (measured by ImageJ), hence the accurate composition of the particles is difficult to be detected by EDS. However, all images were taken in the BES mode, and therefore the darker particles indicate Ti rich (lower atomic number Z). Hence, these dark grey particles should be Ti_2Ni precipitates, which grow after aging process [15][57][58]. As precipitates can act as barriers to dislocation slip during deformation, proper aging will give an effect on strength of solutionized NiTi, which is called precipitate strengthening [59]. However, precipitates with various sizes provide different resistance to dislocation slip. A gliding dislocation must choose an easier way between cutting through the precipitates and penetrating the dislocation line by leaving Orowan loops around precipitates [59]. In addition, the internal stress caused by coherent/semi coherent precipitates also needs to be overcome. Consequently, the larger one of the above stresses is the resistance of precipitates to dislocation slip. In the early stages of aging, the stress increases with precipitates size. With increasing the aging time, the dispersion of coherent or semicoherent precipitates reach a critical status, which can lead to a peak strength. However, further increasing the aging time will lose the coherency and hence decrease the stress. The schematic diagram between hardness and aging time is given in Fig. 4. 13 [59]. The measured hardness value of solutionzied samples as a function of aging time is shown in Fig. 4. 14. Based on the above analysis, 18 hours aging was the closest to the peak aging time due to the highest hardness value. Considering that the hardness value reflects the strength, 18 hours aging time was regarded as the optimized aging time. To simplify the descriptions of heat treatment parameters in further investigations, “Solutionized” (HT7) will be used for “950 ^{o}C for 5.5h and WQ”, “Aged” (HT8) stands for “350 ^{o}C for 18h and WQ”, and “S+A” (HT1) implies “950 ^{o}C for 5.5h and WQ plus 350 ^{o}C for 18h and WQ”. Solutionized, Aged and S+A conditions will be carried out to study the effect of post heat treatments on shape memory behavior in the following chapters.

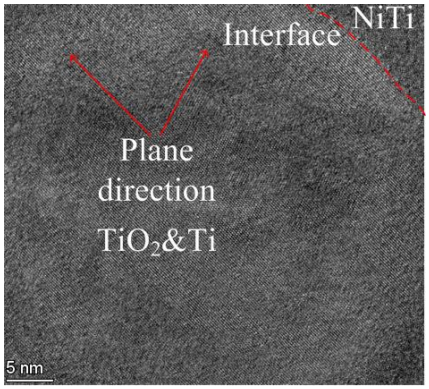

Fig. 4. 7 Transmission electron microscopy images of as fabricated sample.

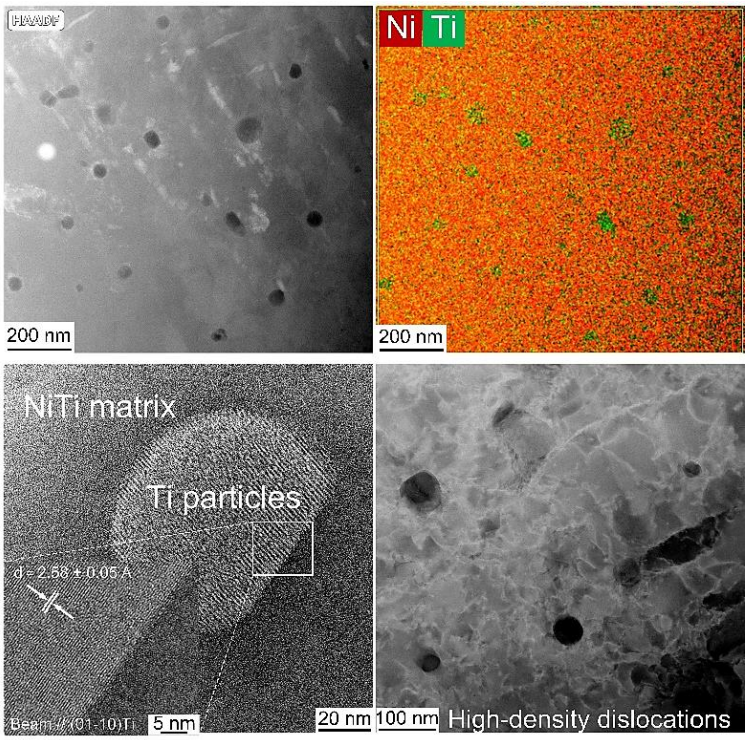

Fig. 4. 8 Transmission electron microscopy images of as fabricated sample.

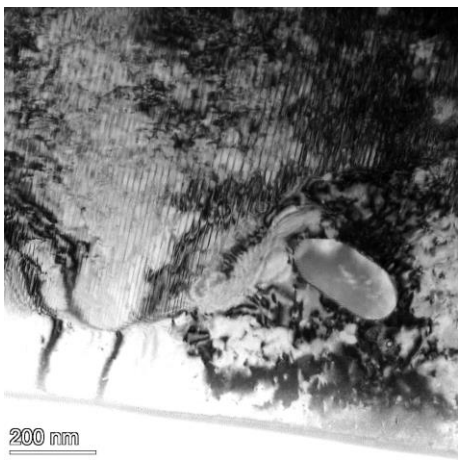

Fig. 4. 9 BF image of solution annealed sample.

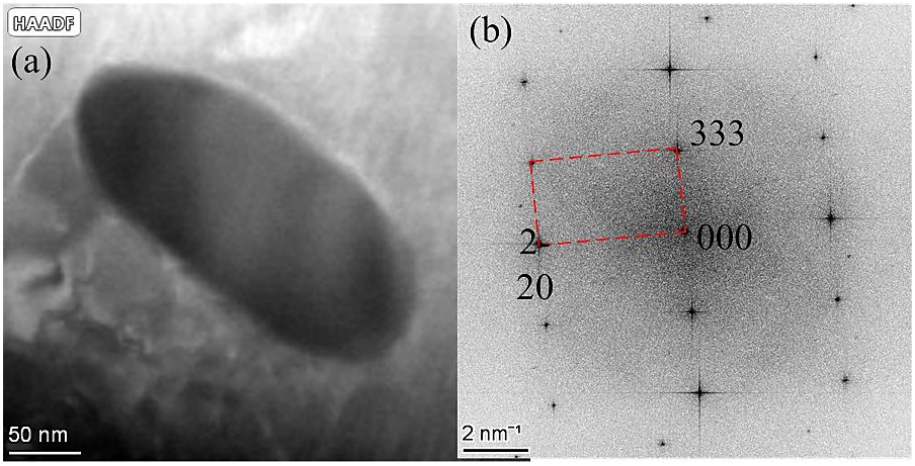

Fig. 4. 10 Transmission electron microscopy images of solution annealed sample.

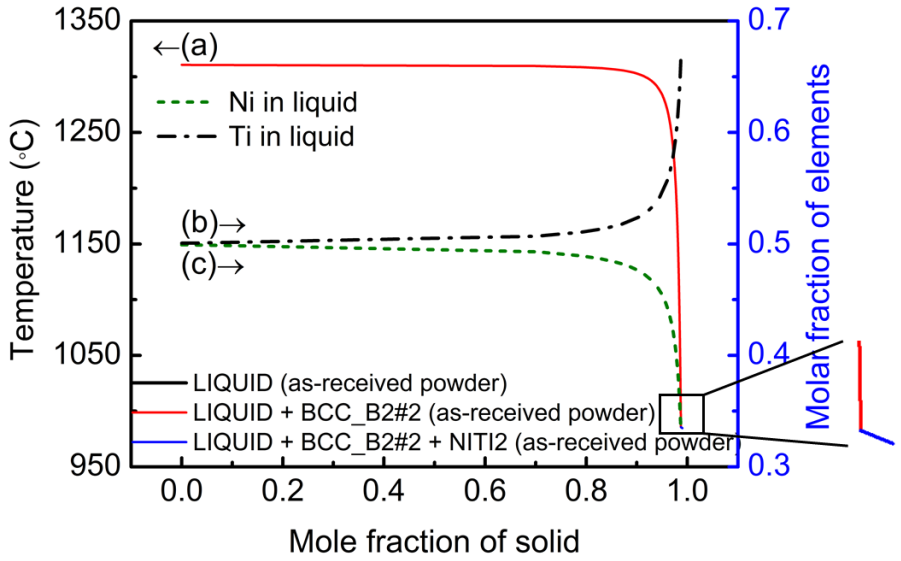

Fig. 4. 11 The Scheil solidification curve.

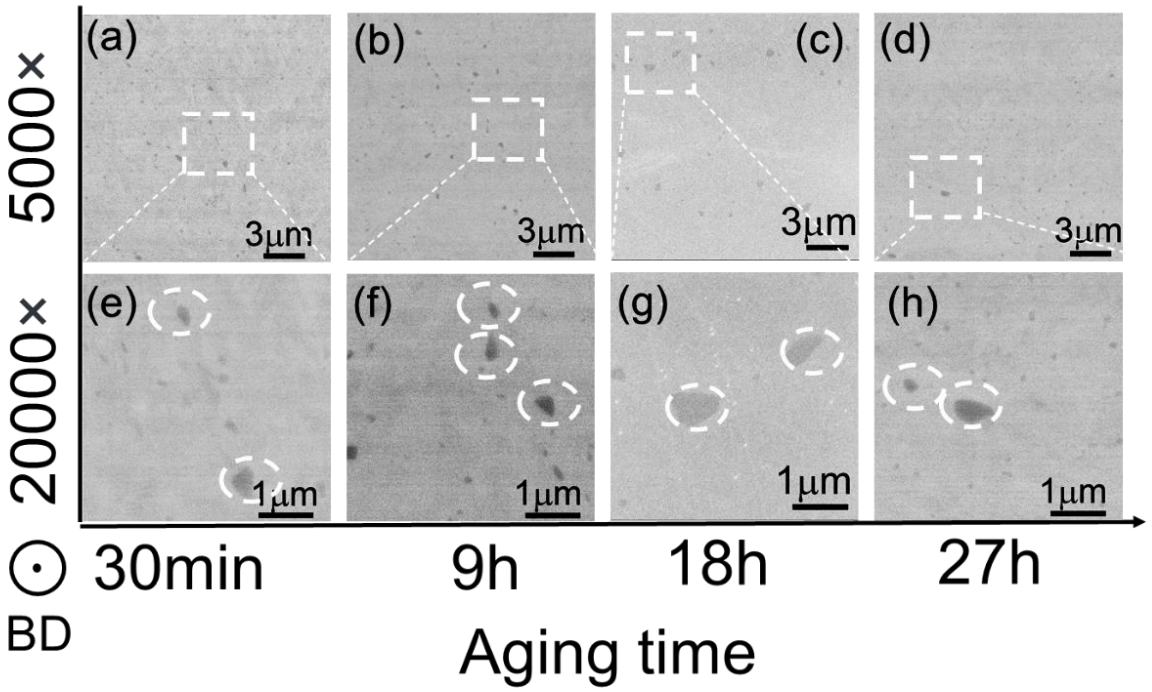

Fig. 4. 12 SEM images of the top surfaces for solutionized samples (950℃ for 5.5h & WQ) followed by aging (350℃): (a) and (e) 30min; (b) and (f) 9h; (c) and (g) 18h; (d) and (h) 27h.

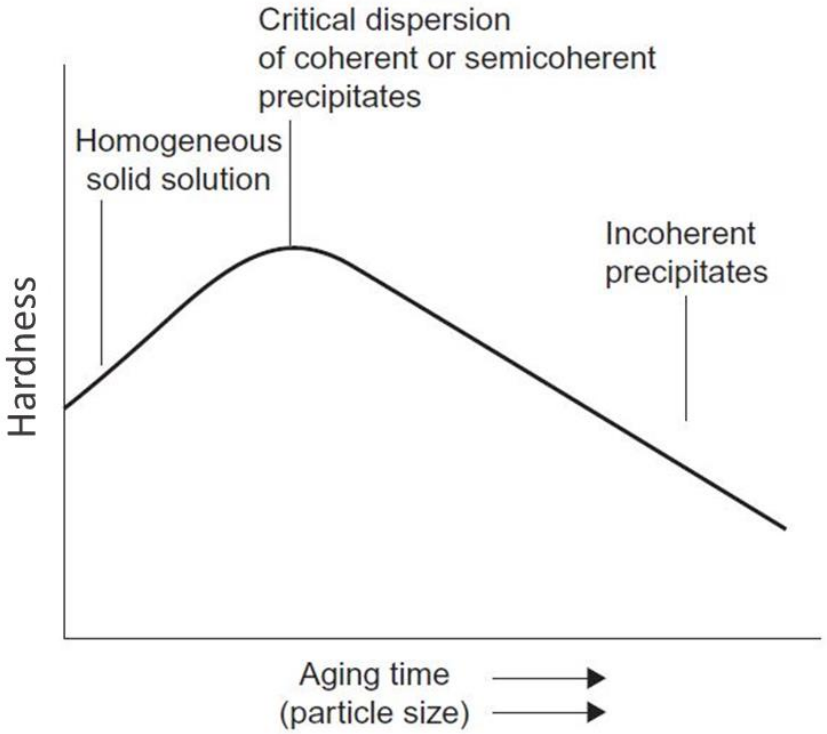

Fig. 4. 13 Schematic variation of hardness with aging time. [59]

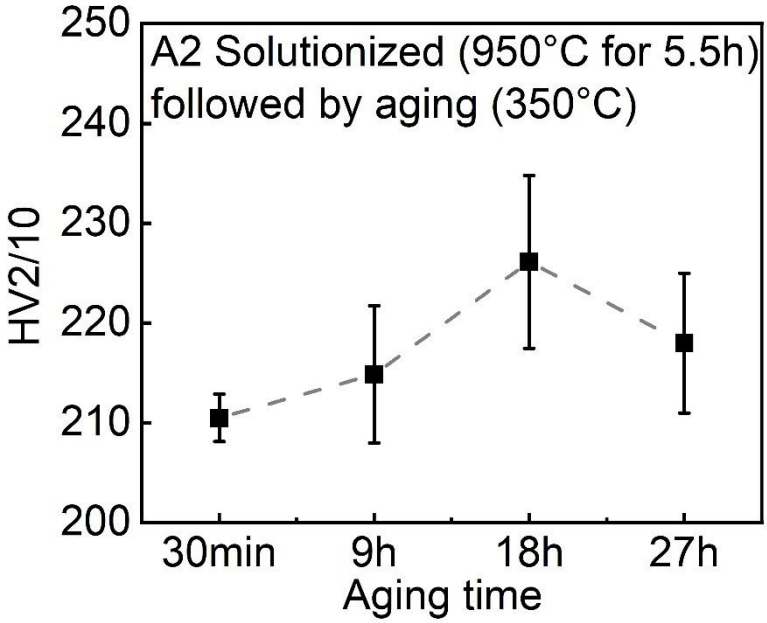

Fig. 4. 14 Vickers hardness of solution annealed A2 as a function of following aging time.

4.3.2 Phase transformation temperature

Fig. 4. 15 shows the DSC plots of the solutionized samples as a function of aging time. The measured phase transformation temperatures are given in Fig. 4. 16. It was observed that phase transformation temperatures were shifted to the lower values with increasing aging duration to 9 hours. This can be attributed to the increased ratio of Ni in the NiTi matrix due to the precipitation of $Ti_2Ni(O)$. However, 18 hours aged sample showed relatively higher phase transformation temperatures compared with 9 hours aged sample. The increase of martensitic transformation temperatures may due to the strong interaction between martensitic transformation and stress field around $Ti_2Ni(O)$ [15]. The stress field originates from the mismatch of lattice parameters between $Ti_2Ni(O)$ and NiTi matrix, which promotes martensite transformation by relaxing transformation strain [15][60][61][62]. There are three stages for the development of stress field as a function of aging time: (1) Coherent strain present at the interface between fine $Ti_2Ni(O)$ and NiTi matrix, which leads to a small stress field; (2) With increasing aging time, $Ti_2Ni(O)$ grows larger, excessive coherent strain partially relaxes by the formation of dislocations [63], [64]. The stress field reaches a maximum value at peak aging time. It should be noted that this peak aging time may be different from the optimum aging time mentioned above for hardness. (3) Over aging produces coarse incoherent $Ti_2Ni(O)$, and

the stress field becomes negligible [57]. The schematic diagram is shown in Fig. 4. 17. In the case of Fig. 4. 15 and Fig. 4. 16, 18 hours aging may produce semicoherent precipitates, which facilitated martensitic transformation and increased transformation temperatures. However, longer aging time may result in large incoherent precipitates and lose coherent strain. In addition, Ti content in the matrix was decreased due to the growth of $Ti_2Ni(O)$, therefore 27 hours aged sample had slightly lower transformation temperatures than that of 18 hours aged sample.

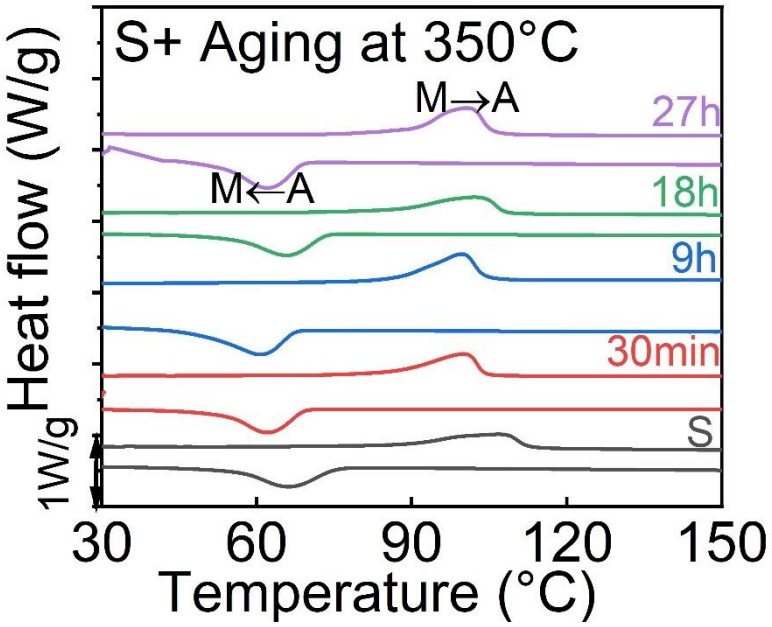

Fig. 4. 15 DSC response of solution annealed A2 aged at 350 °C as a function of aging time.

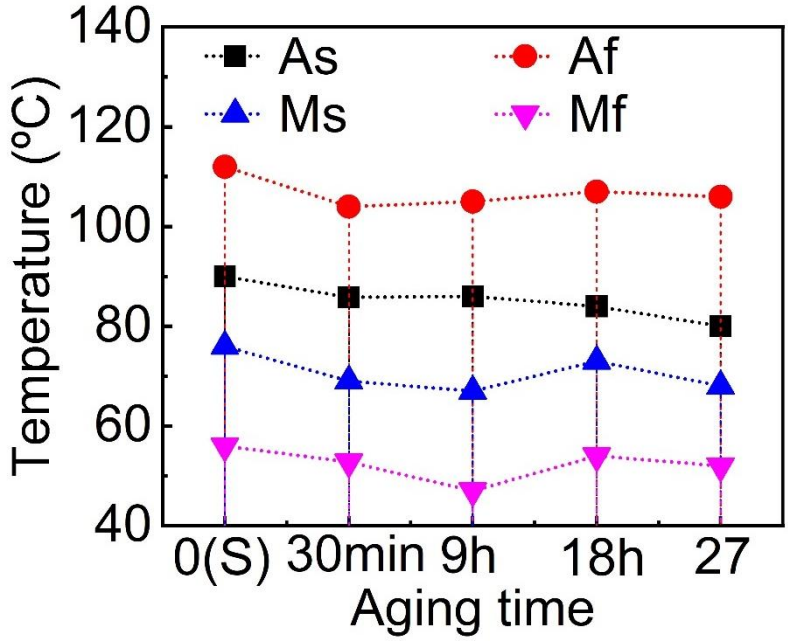

Fig. 4. 16 Effect of aging time on phase transformation temperatures.

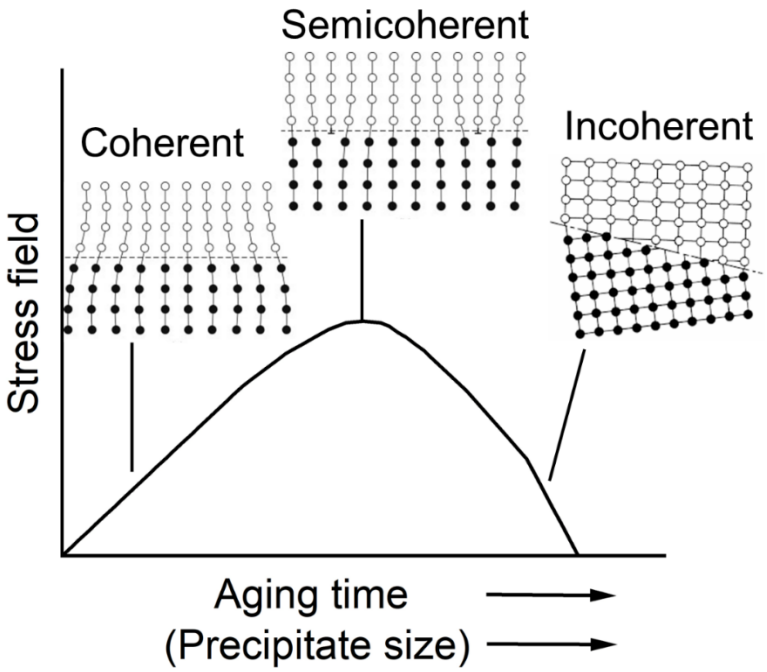

Fig. 4. 17 Schematic of development of stress field

Chapter 5 Effect of post heat treatment on shape memory response

5.1 Effect of heat treatment on phase transformation temperatures

Phase transformation temperatures determine at what temperatures shape memory effect occurs. Hence, it is important to identify the effect of heat treatment on phase transformation temperatures.

Ni and Ti contents of powder and L-PBF fabricated samples were given in Table 5. 1. Ni content decreased 0.2% due to evaporation during L-PBF process, which leads to a Ti-rich NiTi for as fabricated sample. Fig. 5. 1 depicts the DSC responses of A2 samples after heat treatment. Fig. 5. 2 shows the variation of the phase transformation temperatures of tested samples. For comparison, the DSC curves of the powder and as-fabricated sample were also included. It can be observed that the powder has the broadest peaks, which is due to the dispersive diameters of the original powder (Fig. 3. 1 a) [24]. Comparing with the powder, the as-fabricated sample has the higher transformation temperatures. This can be attributed to the lower Ni content due to evaporation of nickel during L-PBF fabricating process. Subsequent solution annealing approaches the material to a state of equilibrium, where microscale heterogeneities and residual stresses are reduced. Consequently, phase transformations are less obstructed. In addition, high temperature solution annealing leds to pure Ti dissolving in the NiTi matrix, which increased the Ti content in the matrix of as fabricated and promoted a shift of transformation temperature to higher values. Moreover, S+A sample shows slightly lower phase transformation temperatures than solutionized sample. As mentioned in Chapter 4, composition alteration and internal stresses caused by $Ti_2Ni(O)$ are the main reasons.

It should be noted that the precipitation process of $Ti_2Ni(O)$ for aged and S+A samples is different. Therefore, leads to a significantly distinguishable structure of $Ti_2Ni(O)$. The schematic diagram of microstructures is given in Fig. 5. 3. The microstructure should be twinning martensite at room temperature, and the real size of defects and $Ti_2Ni(O)$ particles are smaller than that shown in Fig. 5. 3. For aged sample, precipitates prefer to initiating and growing around microscale defects due to their large energy difference with the matrix. Thus, results in inhomogeneous distribution of precipitates. For S+A sample, solution annealing homogenizes microstructures and eliminates defects, then relatively uniform $Ti_2Ni(O)$ nucleates during the water cooling process. Furthermore, subsequent aging provides energy for precipitates to grow. As mentioned in Chapter 4, 18 hours aging exhibits an optimized particle sizes and distribution.

Fig. 5. 4 (a–c) presents DSC curves of A1, A4 and A6 for selected heat treatment conditions. Phase transformation temperatures of A1, A2 and A6 are given in Fig. 5. 4 (d–f), respectively. These DSC responses and variation tendency of phase transformation temperatures of A1, A4 and A6 as function of heat treatment conditions show similar trends with that of A2.

Table 5. 1 Powder and L-PBF fabricated Nitinol compositions

	Ti (at. %)	Ni (at. %)
Power	50.0	50.0
As fabricated	50.2	49.8

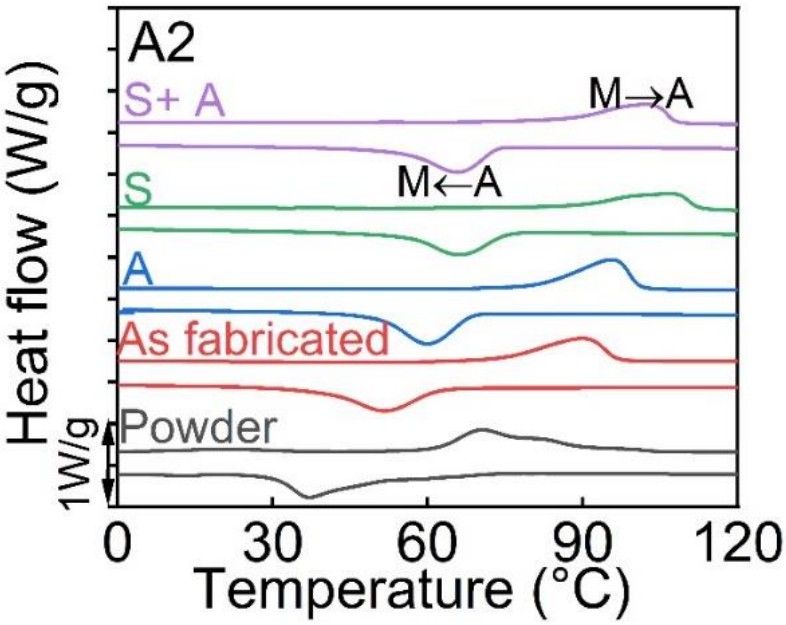

Fig. 5. 1 DSC response of A2 as a function of heat treatment conditions

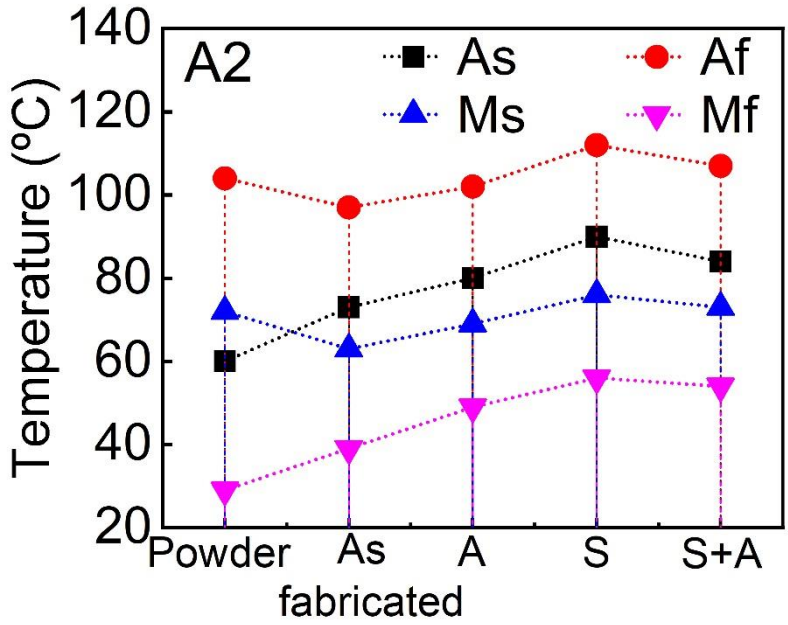

Fig. 5. 2 Phase transformation temperatures of selected conditions for A2 sample.

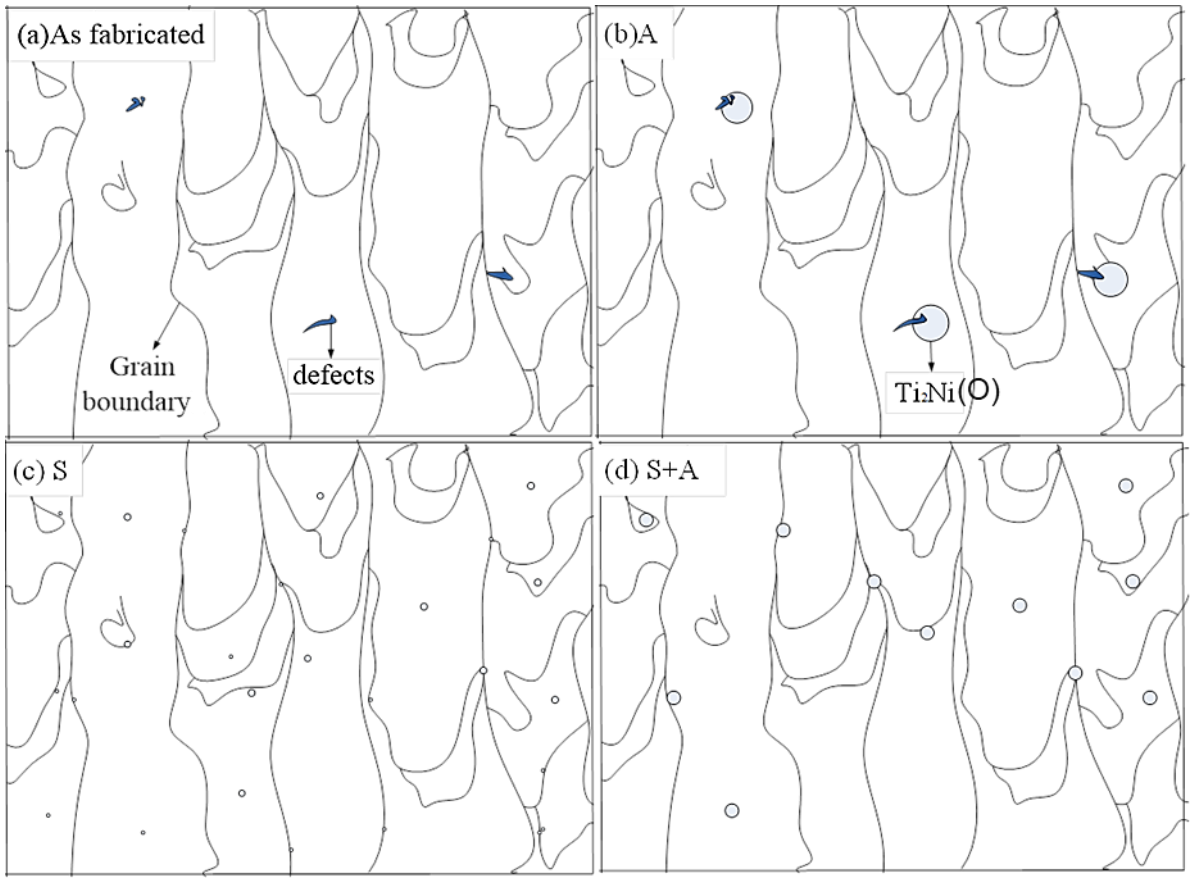

Fig. 5. 3 Schematic diagram of microstructures of testing samples: (a) As fabricated; (b) Aged; (c) Solutionized; (d) S + A.

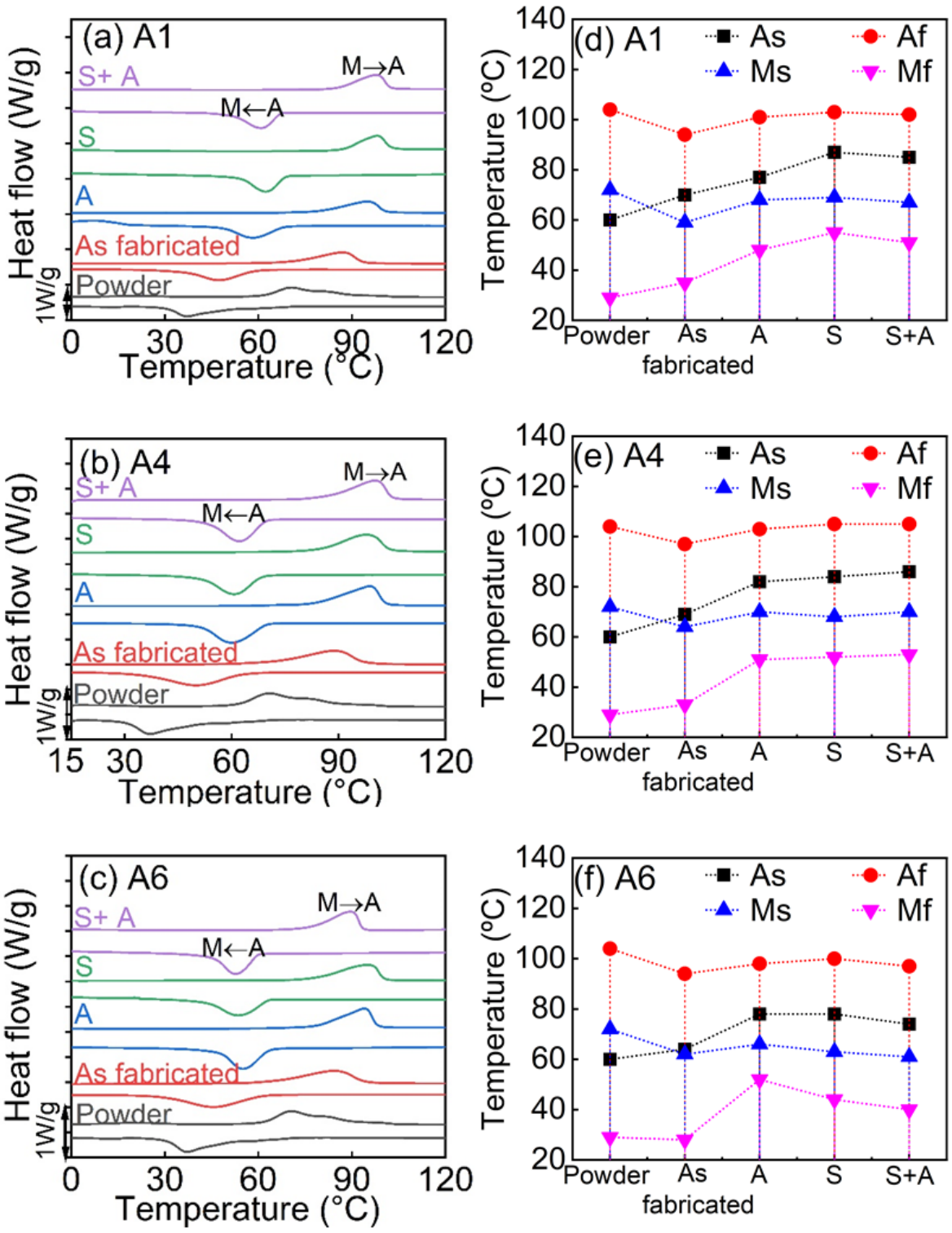

Fig. 5. 4 DSC response and phase transformation temperatures as a function of heat treatment conditions: (a) and (d) A1; (b) and (e) A4; (c) and (f) A6.

5.2 Effect of heat treatment on hardness and microstructures

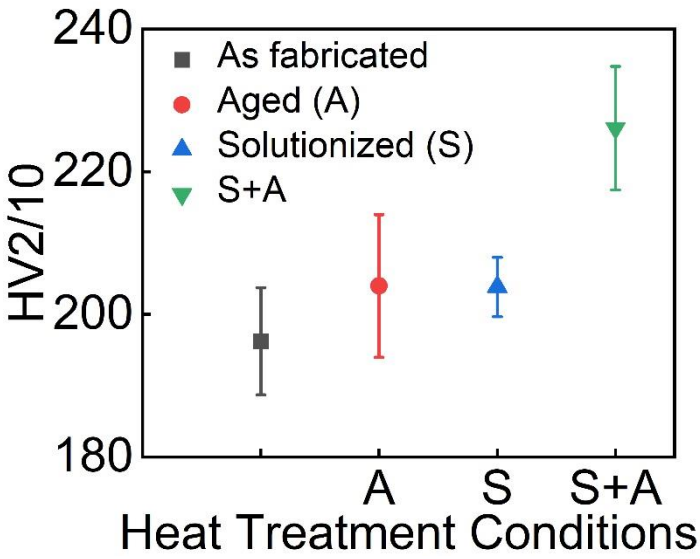

Fig. 5. 5 compares the Vicker's hardness of as fabricated, solutionized, aged and S+A samples for A2 condition at room temperature. Solutionizing and aging both slightly increased the hardness of as-fabricated sample due to precipitates hardening. Moreover, Vicker hardness values of S+A sample shows a significant increase when it is compared to as fabricated sample. This indicates S+A process improved the strength of as fabricated sample, which corresponds to the $Ti_2Ni(O)$ particles.

Fig. 5. 6 (a) and (e) show the optical micrograph of top surfaces and cross sections for as fabricated A2 sample. As mentioned in Chapter 4, the top surface of as fabricated sample shows a checker grain structure with average grain size of about 116×120 μm^2. The cross section displays a columnar structure that reflects the building direction (Fig. 3. 1 b). Fig. 5. 6 (b–d) and (f–h) are the microstructures of heat treated samples from top surface and cross section. Checker grain structure from top surface and columnar grain structure from cross section remained for all heat treated samples, implying good thermal stability of L-PBF A2 sample. However, high temperature heat treatments slightly enlarged the grain size in the perpendicular to scanning direction due to Ostwald ripening phenomenon (Table 5. 2). Optical micrograph of top surfaces for A1, A4 and A6 under selected heat treatment conditions are given in Fig. 5. 7, Fig. 5. 8 and Fig. 5. 9, respectively. They also show negligibly influence of heat treatment on microstructures of A1, A4 and A6. This clarifies that A1, A4 and A6 process shows good thermal stability as well.

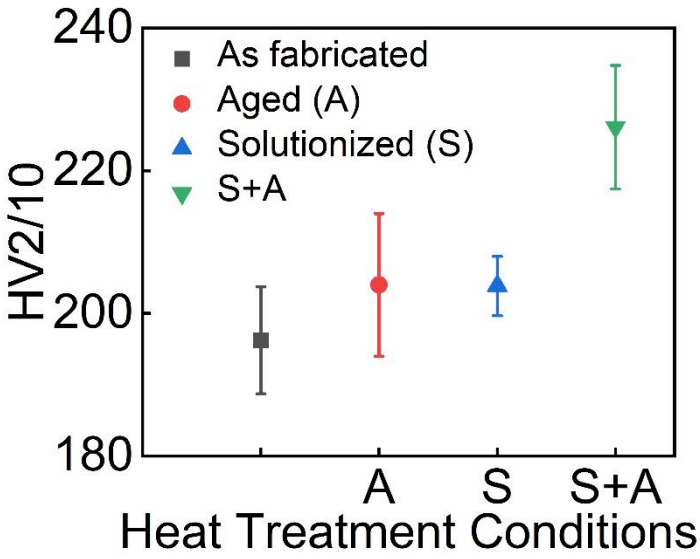

Fig. 5. 5 Vicker hardness as function of heat treatment conditions: A (Aged); S (Solutionized); S+A (Solutionized+ Aged).

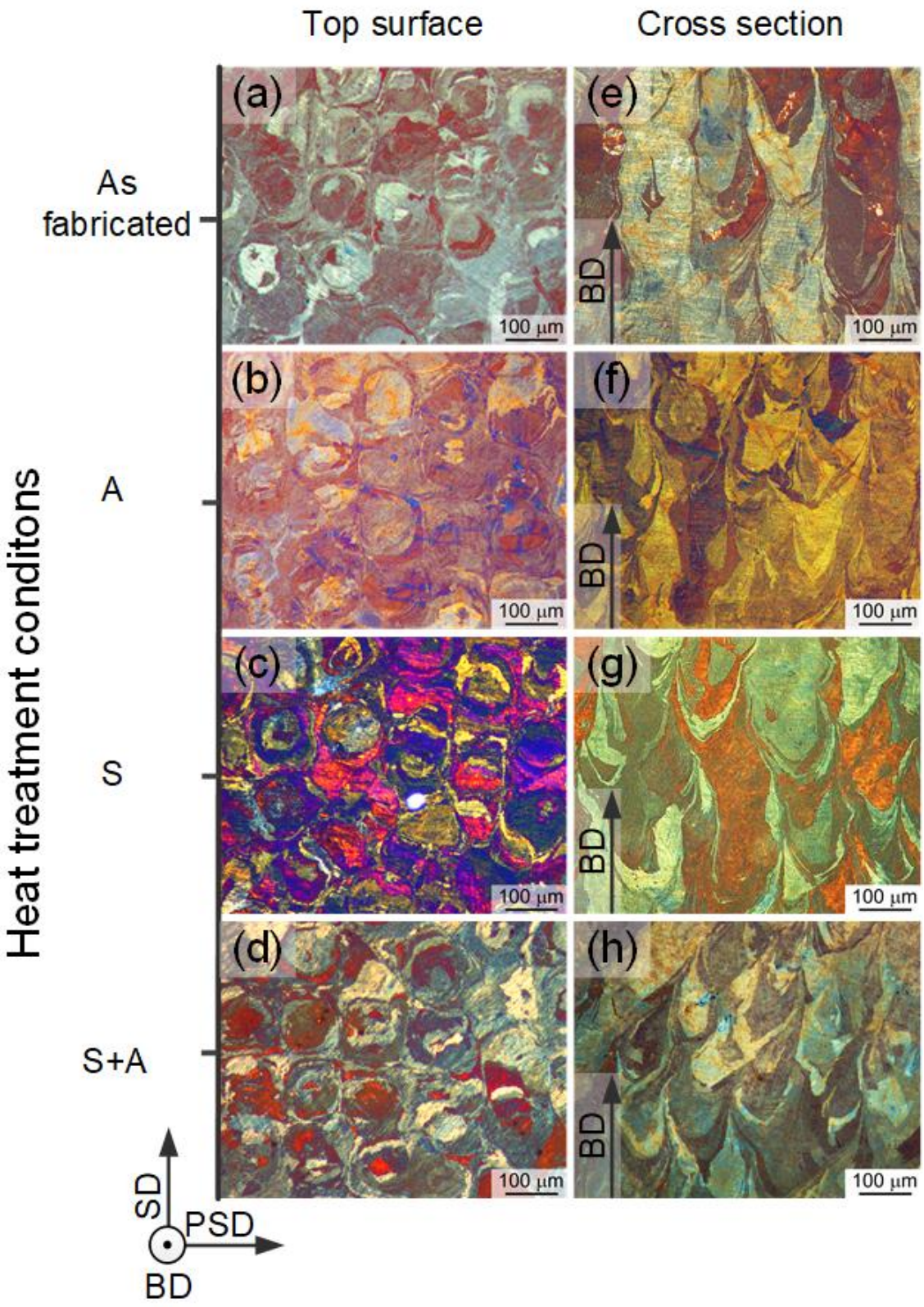

Fig. 5. 6 Optical microscopy images of top surfaces and cross sections for A2: (a) and (e) As fabricated; (b) and (f) Aged; (c) and (g) Solutionized; (d) and (h) S+A.

Table 5. 2 Comparison of grain sizes after heat treatments

HT conditions	Size in the scanning direction (μm)	Size in the perpendicular direction (μm)
As fabricated	116.3 ± 0.5	120.2 ± 3.2
A	117 ± 0.2	119.8 ± 0.5
S	118 ± 0.4	138 ± 0.8
S+A	118 ± 0.5	140 ± 0.6

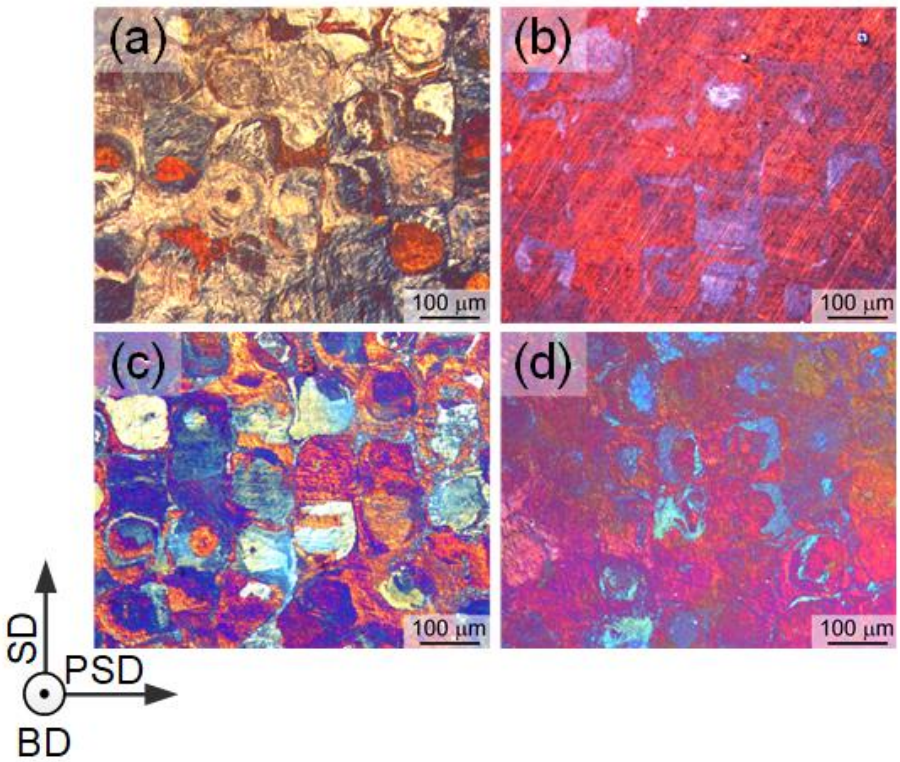

Fig. 5. 7 Optical microscopy images of top surfaces for A1: (a) As fabricated; (b) Aged; (c) Solutionized; (d) S+A.

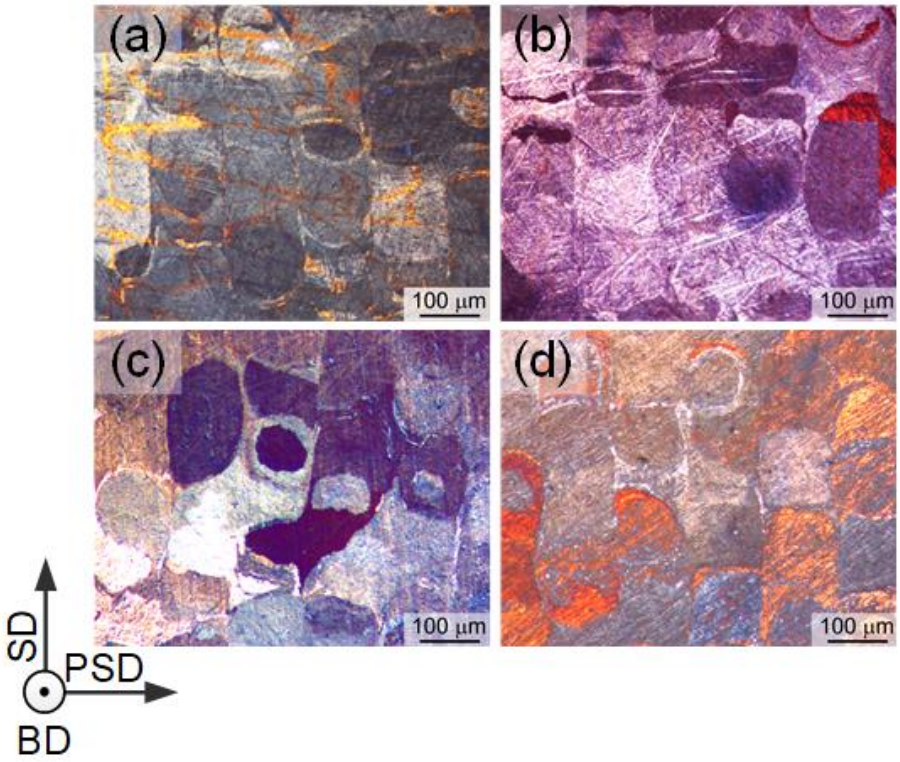

Fig. 5. 8 Optical microscopy images of top surfaces for A4: (a) As fabricated; (b) Aged; (c) Solutionized; (d) S+A.

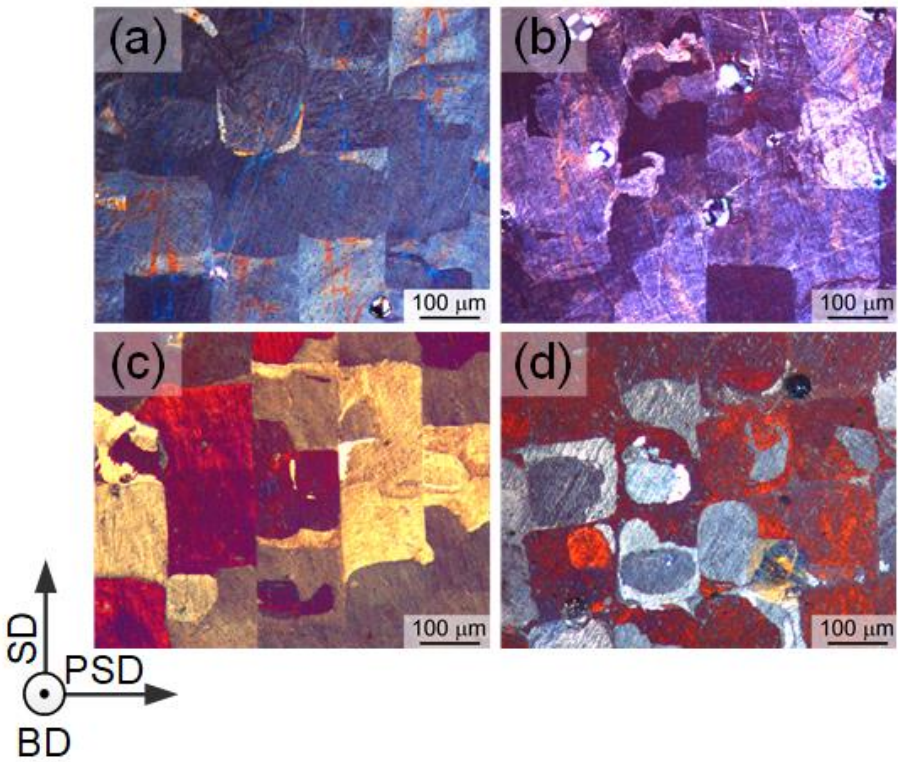

Fig. 5. 9 Optical microscopy images of top surfaces for A6: (a) As fabricated; (b) Aged; (c) Solutionized; (d) S+A.

5.3 XRD measurements and phase fraction

As shown in Fig. 5. 1 and Table 5. 1, the martensite finish temperatures of all samples are higher than room temperature. Hence, all samples were in martensite phase state. However, the XRD spectra exhibits an austenite peak in all samples (Fig. 5. 10). The residual austenite phase may originate from the heterogeneous cooling rate of different parts of samples caused by geometrical conditions. It should be stressed that the residual austenite phase is one of the reasons of degradation of the shape memory behavior and instable cyclic mechanical properties.

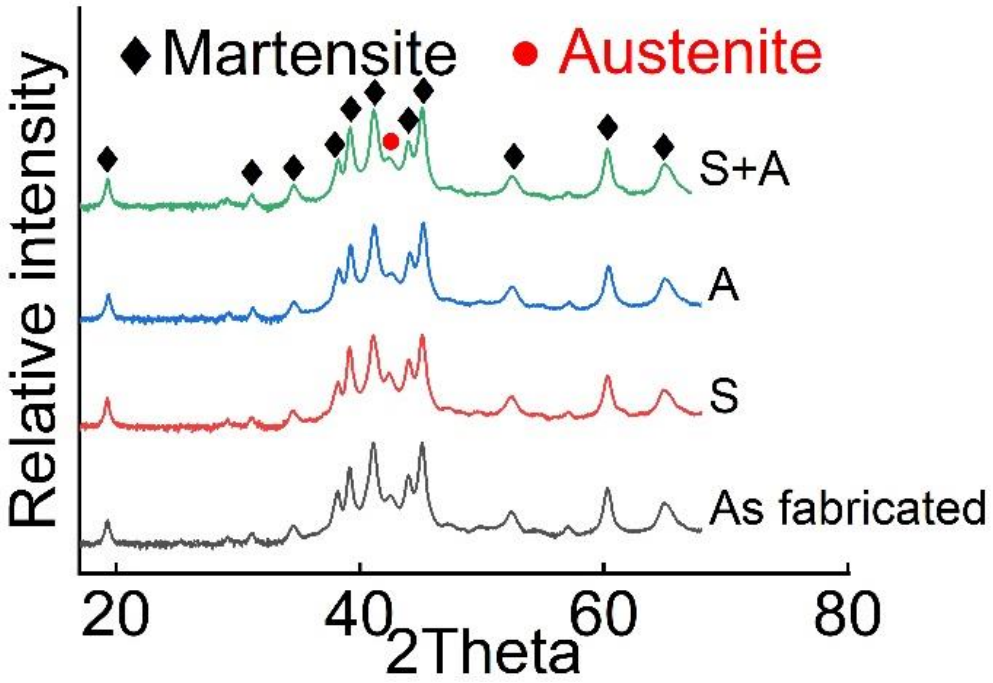

Fig. 5. 10 XRD patterns of A2 as a function of heat treatment conditions (NB: background is subtracted with Y-offset, y-scale is in SQRT)

5.4. Shape memory behavior

5.4.1 Shape memory recovery under gradually increased strain level

Fig. 5. 11 (a–d) shows the stress-strain curves of all samples under gradually increased strain level. All samples show similar mechanical behaviour, which includes elastic deformation of twinned martensite, detwinning process and the elastic deformation of detwinned martensite (Fig. 2. 22). It can be observed that work hardening occurs in all samples, which indicates dislocations evolved and accumulated during mechanical tests. The evolution and accumulation of dislocations impede phase transformation and influence shape memory properties. Recovery ratio of all sample is given in Fig. 5. 11 (e), showing no significant effect

for different heat treatment conditons. However, all post heat treatment process improved the maximum true stress under same strain level (Fig. 5. 11 (f)). As fabricated sample has the lowest stress value due to the microscale defects formed during the L-PBF process. Aging process slightly enhanced the stress value due to the formation of $Ti_2Ni(O)$ particles. Solution annealing homogenized the microstructure, eliminated the microscale defects and generated $Ti_2Ni(O)$ particles, hence also has a positive effect on the stress level. In addition, S+A sample shows the highest stress values for all strain levels, which is consistent with its highest hardness value (Fig. 5. 5). This can be rationalized by the function of heat treatment process. Solution annealing removed the microscale defects, while $Ti_2Ni(O)$ precipitated during the following aging process and strengthened the sample by impeding the slip of dislocations. The present work demonstrates that the stress window was improved by S+A without any sacrifice in the recovery ratio.

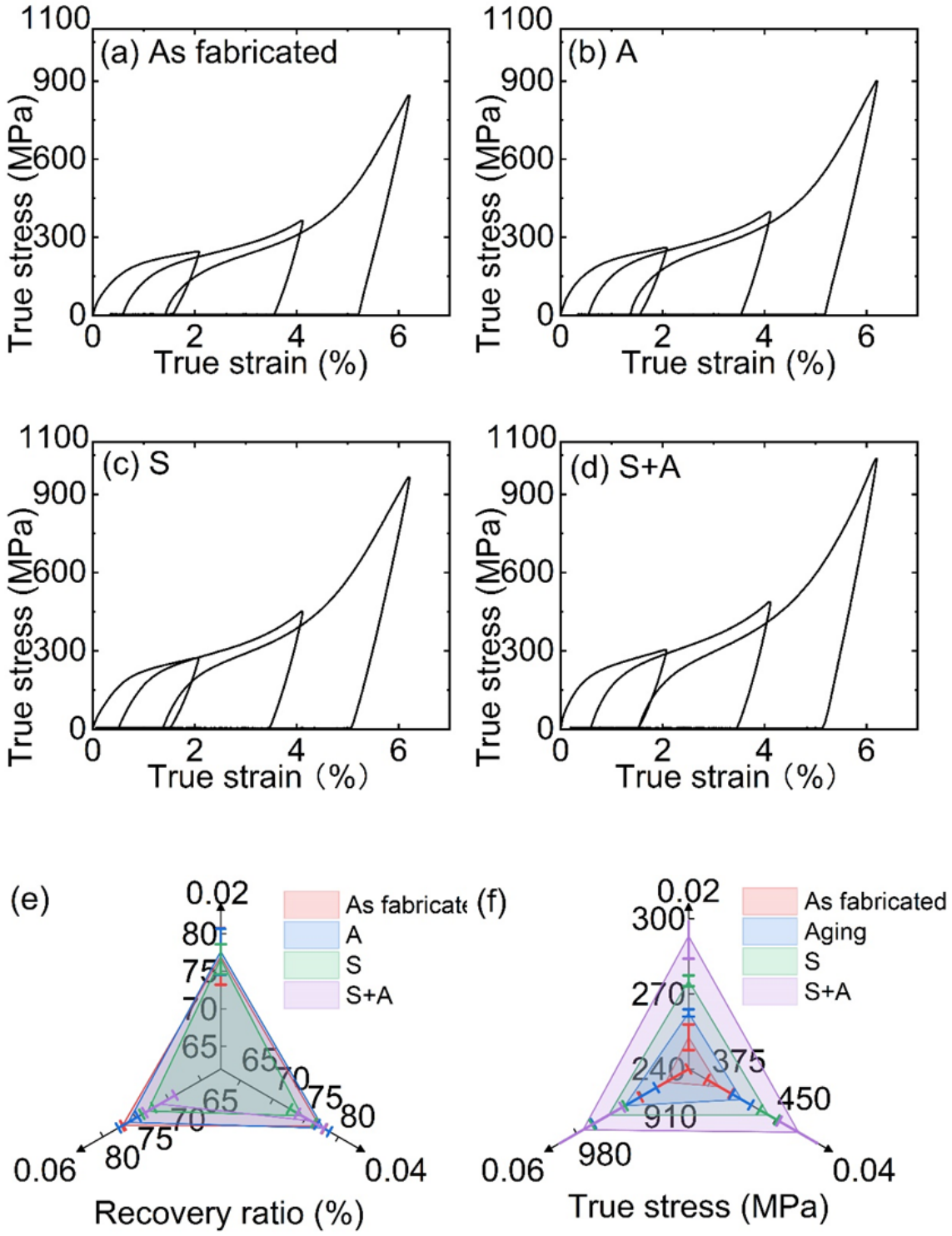

Fig. 5. 11 Stress-strain curves under gradually increased strain level, and corresponding recovery ratio and maximum stress. (a) As fabricated; (b) Aged; (c) Solutionized; (d) S+A; (e) Recovery ratio; (f) Maximum true stress

5.4.2 Cyclic stability under constant strain level

As many shape memory components are used in cyclic applications, hence the cyclic stability is important. Fig. 5. 12 shows the stress- strain curves under 4% deformation for 50 cycles. This strain level was chosen because 4% corresponds to a strain where detwinning is completed and the onset of elastic deformation of detwinned martensite (Fig. 5. 11 and Fig. 2. 22). Fig. 5. 13 shows the evolution of strain recovery during cycling. As explained above, microscale defects and dislocations can evolve and accumulate after cyclic mechanical tests. Furthermore, plastic strain occurred and increased due to local strain concentration and the deformation of residual austenite. All these factors hamper the phase transformation process. As a consequence, degradation of reversible strain appeared. It can also be observed that highest reversible strain reduction occurs in the first cycle, while it continuously decay with increasing the number of cycles. The reason is that work hardening caused a decrease of applied stress under stable strain level. Lower applied stress produces less dislocations accumulation. However, rational post heat treatment can reduce the degradation effects by decreasing these detrimental factors. The recovery strain of aged sample is lowest and decreases almost parallelly to as fabricated sample (Fig. 5. 13). This is reasonable as aging not only promotes new local defects by nonuniform $Ti_2Ni(O)$ particles, but also keeps the heterogeneous microstructures of as fabricated sample. However, the recovery strain of solutionized degrade much slower than that of as fabricated samples after cyclic tests. It can be explained by the minimizing microscale defects of solutionized sample. It is remarkable that S+A sample has the highest recovery strain compared to S sample, especially for the first 30 cycles. The reason is that more uniform $Ti_2Ni(O)$ precipitated in the solutionized sample during the following aging process. $Ti_2Ni(O)$ particles impede the slip of dislocations, and hence improve the mechanical stability of S+A sample. In addition, a drop present at the 14^{th} cycle in the recovery strain curve of S+A sample, which shows a two-stage degradation. The drop may be caused by newly formed smaller martensite plates between the larger regions of stabilized martensite after several cycles [23]. These smaller martensite plates increased grain boundaries density and thus introduce new regions for dislocation accumulation. In conclusion, S+A improved by 51% recoverable strain and over 70 MPa stress, compared with as-fabricated sample for cyclic stability test.

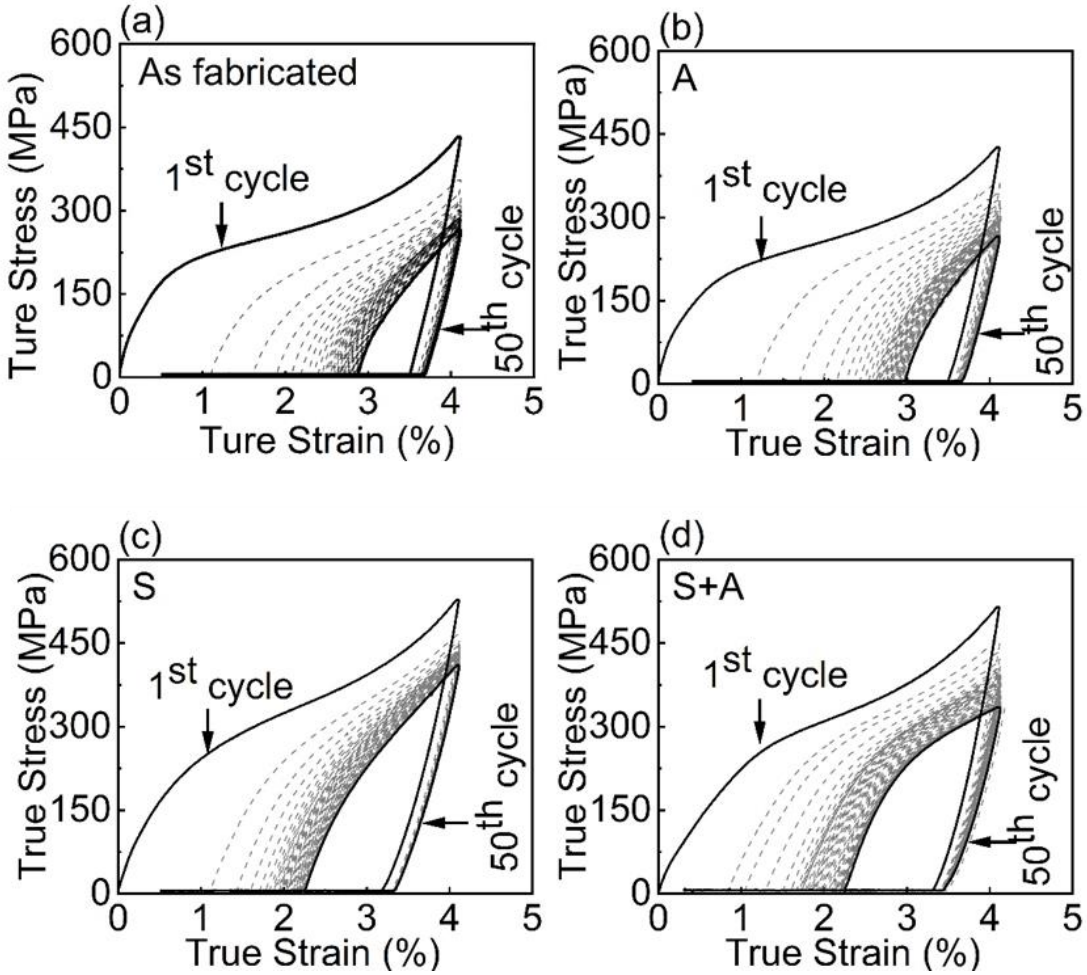

Fig. 5. 12 Stress-strain curves under 4% deformation for 50 cycles: (a) as fabricated; (b) aged; (c) solutionized; (d) S+A.

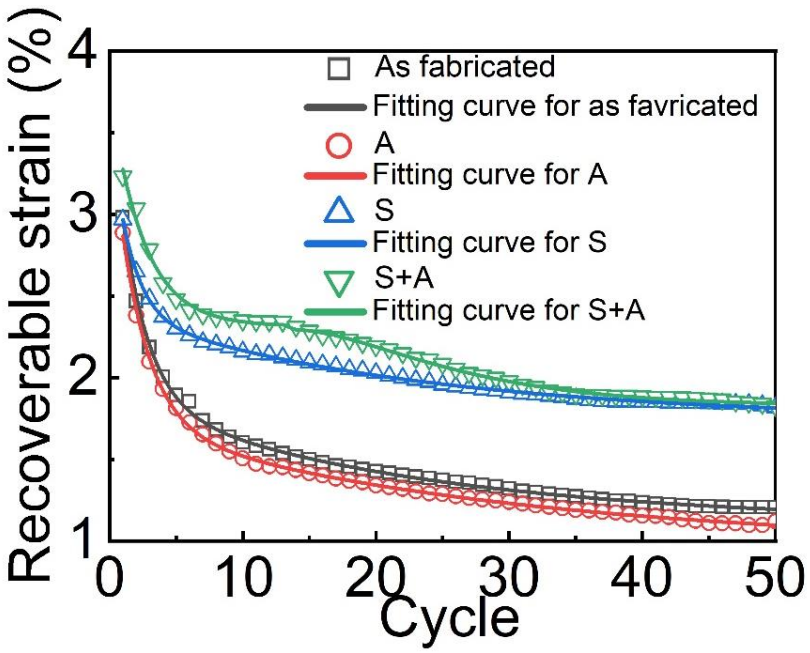

Fig. 5. 13 Recoverable strain as a function of cycles under 4% deformation

Conclusions and Recommendations

In this work, we report an improvement of the cyclic stability of the Ti50Ni50 SMA by solution annealing and solution annealing followed by aging heat treatment. The microstructural evolution, phase transformation mechanism, and shape memory properties were investigated. The main conclusions are summarized below:

(1) Heat treatment process had no significant influence on the grain structures for all studied herein L-PBF samples.

(2) Solution annealing and solution annealing followed by aging heat treatment improved the hardness and strength due to the formation of $Ti_2Ni(O)$ precipitations. Optimized heat treatment was found to be S+A (Aging for 18 hours), which precipitated dispersive $Ti_2Ni(O)$ and showed the best hardness and peak stress. In comparison, the as fabricated sample had a mixture of second phase TiO_2 and pure Ti.

(3) After gradually increased strain level in mechanical testing, the stress window was improved by S+A without any sacrifice in the recovery ratio. In addition, S+A improved by 51.3% recoverable strain and over 70 MPa stress, compared with as-fabricated sample for the cyclic stability test. The improved recoverable strain is attributed to the existence of $Ti_2Ni(O)$ precipitates and dislocation strengthening. $Ti_2Ni(O)$ precipitates hindered the motion and formation of dislocations during the cyclic tension test.

This thesis presents initial findings of optimized post process heat treatments. The following recommendations are proposed for the future work:

(1) Tests at lower strain levels at which detwinning process is completed and there is no elastic deformation of the detwinned martensite.

(2) Post processing heat treatments could be further modified to achieve a more homogenous distribution of $Ti_2Ni(O)$.

(3) The density of precipitates is not high even for the optimized heat treatment conditions. Further study could be done to Ti rich Nitinol. Post processing heat treatments could be further modified to achieve a more homogenous distribution of $Ti_2Ni(O)$.

Bibliography

[1] *Shape Memory Alloys*, vol. 1. Boston, MA: Springer US, 2008.

[2] ASM, *ASM handbook Volume 2 - Properties and selection: Nonferrous alloys and special-purpose materials*, vol. 2. ASM International, 1993.

[3] E. Farber, J. N. Zhu, A. Popovich, and V. Popovich, "A review of NiTi shape memory alloy as a smart material produced by additive manufacturing," *Mater. Today Proc.*, vol. 30, pp. 761–767, Jan. 2020, doi: 10.1016/J.MATPR.2020.01.563.

[4] Z. Khoo, Y. Liu, J. An, C. Chua, Y. Shen, and C. Kuo, "A Review of Selective Laser Melted NiTi Shape Memory Alloy," *Materials (Basel).*, vol. 11, no. 4, p. 519, Mar. 2018, doi: 10.3390/ma11040519.

[5] C. Velmurugan, V. Senthilkumar, S. Dinesh, and D. Arulkirubakaran, "Review on phase transformation behavior of NiTi shape memory alloys," *Mater. Today Proc.*, vol. 5, no. 6, pp. 14597–14606, Jan. 2018, doi: 10.1016/J.MATPR.2018.03.051.

[6] F. Calignano *et al.*, "Overview on Additive Manufacturing Technologies," *Proc. IEEE*, vol. 105, no. 4, pp. 593–612, Apr. 2017, doi: 10.1109/JPROC.2016.2625098.

[7] T. D. Ngo, A. Kashani, G. Imbalzano, K. T. Q. Nguyen, and D. Hui, "Additive manufacturing (3D printing): A review of materials, methods, applications and challenges," *Compos. Part B Eng.*, vol. 143, no. December 2017, pp. 172–196, 2018, doi: 10.1016/j.compositesb.2018.02.012.

[8] I. Gibson, D. Rosen, and B. Stucker, *Additive Manufacturing Technologies*. New York, NY: Springer New York, 2015.

[9] L. Jiao, Z. Chua, S. Moon, J. Song, G. Bi, and H. Zheng, "Femtosecond Laser Produced Hydrophobic Hierarchical Structures on Additive Manufacturing Parts," *Nanomaterials*, vol. 8, no. 8, p. 601, Aug. 2018, doi: 10.3390/nano8080601.

[10] J. C. Chekotu, R. Groarke, K. O'Toole, and D. Brabazon, "Advances in selective laser melting of Nitinol shape memory alloy part production," *Materials (Basel).*, vol. 12, no. 5, 2019, doi: 10.3390/MA12050809.

[11] N. T. Aboulkhair, N. M. Everitt, I. Ashcroft, and C. Tuck, "Reducing porosity in AlSi10Mg parts processed by selective laser melting," *Addit. Manuf.*, vol. 1, pp. 77–86,

2014, doi: 10.1016/j.addma.2014.08.001.

[12] M. Elahinia, N. Shayesteh Moghaddam, M. Taheri Andani, A. Amerinatanzi, B. A. Bimber, and R. F. Hamilton, "Fabrication of NiTi through additive manufacturing: A review," *Prog. Mater. Sci.*, vol. 83, pp. 630–663, Oct. 2016, doi: 10.1016/j.pmatsci.2016.08.001.

[13] S. Saedi, N. Shayesteh Moghaddam, A. Amerinatanzi, M. Elahinia, and H. E. Karaca, "On the effects of selective laser melting process parameters on microstructure and thermomechanical response of Ni-rich NiTi," *Acta Mater.*, vol. 144, pp. 552–560, 2018, doi: 10.1016/j.actamat.2017.10.072.

[14] C. Y. Yap *et al.*, "Review of selective laser melting: Materials and applications," *Appl. Phys. Rev.*, vol. 2, no. 4, p. 041101, Dec. 2015, doi: 10.1063/1.4935926.

[15] K. Otsuka and X. Ren, "Physical metallurgy of Ti-Ni-based shape memory alloys," *Prog. Mater. Sci.*, vol. 50, no. 5, pp. 511–678, Jul. 2005, doi: 10.1016/j.pmatsci.2004.10.001.

[16] "ASTM F 2005-05: Standard Terminology for Nickel-Titanium Shape Memory Alloys."

[17] C. A. Biffi, J. Fiocchi, F. Valenza, P. Bassani, and A. Tuissi, "Selective Laser Melting of NiTi Shape Memory Alloy: Processability, Microstructure, and Superelasticity," *Shape Mem. Superelasticity*, vol. 6, no. 3, pp. 342–353, 2020, doi: 10.1007/s40830-020-00298-8.

[18] Y. Guo, A. Klink, C. Fu, and J. Snyder, "Machinability and surface integrity of Nitinol shape memory alloy," *CIRP Ann.*, vol. 62, no. 1, pp. 83–86, Jan. 2013, doi: 10.1016/J.CIRP.2013.03.004.

[19] O. E. Ozbulut, S. Daghash, and M. M. Sherif, "Shape Memory Alloy Cables for Structural Applications," *J. Mater. Civ. Eng.*, vol. 28, no. 4, p. 04015176, Apr. 2016, doi: 10.1061/(ASCE)MT.1943-5533.0001457.

[20] S. Saedi, "Shape Memory Behavior of Dense and Porous NiTi Alloys Fabricated by Selective Laser Melting," 2017.

[21] H. Meier, J. Haberland, J. Frenzel, and R. Zarnetta, *Selective laser melting of NiTi shape memory components*. .

[22] C. Haberland, M. Elahinia, J. M. Walker, H. Meier, and J. Frenzel, "On the development

of high quality NiTi shape memory and pseudoelastic parts by additive manufacturing," *Smart Mater. Struct.*, vol. 23, no. 10, 2014, doi: 10.1088/0964-1726/23/10/104002.

[23] M. Taheri Andani *et al.*, "Mechanical and shape memory properties of porous Ni50.1Ti49.9 alloys manufactured by selective laser melting," *J. Mech. Behav. Biomed. Mater.*, vol. 68, no. July 2016, pp. 224–231, 2017, doi: 10.1016/j.jmbbm.2017.01.047.

[24] S. Saedi *et al.*, "The influence of heat treatment on the thermomechanical response of Ni-rich NiTi alloys manufactured by selective laser melting," *J. Alloys Compd.*, vol. 677, pp. 204–210, Aug. 2016, doi: 10.1016/j.jallcom.2016.03.161.

[25] S. Dadbakhsh, M. Speirs, J. P. Kruth, J. Schrooten, J. Luyten, and J. Van Humbeeck, "Effect of SLM parameters on transformation temperatures of shape memory nickel titanium parts," *Adv. Eng. Mater.*, vol. 16, no. 9, pp. 1140–1146, 2014, doi: 10.1002/adem.201300558.

[26] T. Bormann, B. Müller, M. Schinhammer, A. Kessler, P. Thalmann, and M. De Wild, "Microstructure of selective laser melted nickel-titanium," *Mater. Charact.*, vol. 94, pp. 189–202, Aug. 2014, doi: 10.1016/j.matchar.2014.05.017.

[27] I. Shishkovsky, I. Yadroitsev, and I. Smurov, "Direct Selective Laser Melting of Nitinol Powder," *Phys. Procedia*, vol. 39, pp. 447–454, 2012, doi: 10.1016/j.phpro.2012.10.060.

[28] J.-N. Zhu, E. Borisov, X. Liang, E. Farber, M. J. M. Hermans, and V. A. Popovich, "Predictive analytical modelling and experimental validation of processing maps in additive manufacturing of nitinol alloys," *Addit. Manuf.*, vol. 38, p. 101802, Feb. 2021, doi: 10.1016/j.addma.2020.101802.

[29] "ASTM F2004：Standard Test Method for Transformation Temperature of Nickel-Titanium Alloys by Thermal Analysis ."

[30] "A. International, Standard Specification for Wrought Nickel-Titanium Shape Memory Alloys for Medical Devices and Surgical Implants."

[31] "An Overview of Nitinol: Superelastic and Shape Memory - Medical Design Briefs." https://www.medicaldesignbriefs.com/component/content/article/mdb/features/articles/23077 (accessed Jul. 11, 2021).

[32] D. S. Levi, N. Kusnezov, and G. P. Carman, "Smart Materials Applications for Pediatric Cardiovascular Devices," *Pediatr. Res.*, vol. 63, no. 5, pp. 552–558, May 2008, doi:

10.1203/PDR.0b013e31816a9d18.

[33] M. Simon *et al.*, "Simon nitinol inferior vena cava filter: initial clinical experience. Work in progress.," *Radiology*, vol. 172, no. 1, pp. 99–103, Jul. 1989, doi: 10.1148/radiology.172.1.2662259.

[34] "'Simon Nitinol IVC Filters' Now Included In BARD IVC FILTER MDL 2641 Claims."

[35] T. Ikeda, "The use of shape memory alloys (SMAs) in aerospace engineering," *Shape Mem. Superelastic Alloy.*, pp. 125–140, Jan. 2011, doi: 10.1533/9780857092625.2.125.

[36] S.-M. An, J. Ryu, M. Cho, and K.-J. Cho, "Engineering design framework for a shape memory alloy coil spring actuator using a static two-state model," *Smart Mater. Struct.*, vol. 21, no. 5, p. 055009, May 2012, doi: 10.1088/0964-1726/21/5/055009.

[37] E. F. Harris, S. M. Newman, and J. A. Nicholson, "Nitinol arch wire in a simulated oral environment. Changes in mechanical properties," *Am. J. Orthod. Dentofac. Orthop.*, vol. 93, no. 6, pp. 508–513, Jun. 1988, doi: 10.1016/0889-5406(88)90080-7.

[38] P. Šittner, L. Heller, J. Pilch, C. Curfs, T. Alonso, and D. Favier, "Young's Modulus of Austenite and Martensite Phases in Superelastic NiTi Wires," *J. Mater. Eng. Perform.*, vol. 23, no. 7, pp. 2303–2314, Jul. 2014, doi: 10.1007/s11665-014-0976-x.

[39] A. R. Pelton, T. W. Duerig, and D. Stöckel, "A guide to shape memory and superelasticity in Nitinol medical devices," *Minim. Invasive Ther. Allied Technol.*, vol. 13, no. 4, pp. 218–221, Jan. 2004, doi: 10.1080/13645700410017236.

[40] H. Qian, H. Li, G. Song, and W. Guo, "Recentering Shape Memory Alloy Passive Damper for Structural Vibration Control," *Math. Probl. Eng.*, vol. 2013, pp. 1–13, 2013, doi: 10.1155/2013/963530.

[41] "ASTM F2063: Standard Specification for Wrought Nickel-Titanium Shape Memory Alloys for Medical Devices and Surgical Implants."

[42] C. Haberland, M. Elahinia, J. Walker, H. Meier, and J. Frenzel, "Additive Manufacturing of Shape Memory Devices and Pseudoelastic Components," Sep. 2013, doi: 10.1115/SMASIS2013-3070.

[43] F. Jiang, Y. Liu, H. Yang, L. Li, and Y. Zheng, "Effect of ageing treatment on the deformation behaviour of Ti–50.9 at.% Ni," *Acta Mater.*, vol. 57, no. 16, pp. 4773–4781,

Sep. 2009, doi: 10.1016/J.ACTAMAT.2009.06.059.

[44] I. Kaya *et al.*, "Effects of aging on the shape memory and superelasticity behavior of ultra-high strength Ni 54 Ti 46 alloys under compression," *Mater. Sci. Eng. A*, vol. 678, pp. 93–100, Dec. 2016, doi: 10.1016/j.msea.2016.09.078.

[45] A. Radi, J. Khalil-Allafi, M. R. Etminanfar, S. Pourbabak, D. Schryvers, and B. Amin-Ahmadi, "Influence of stress aging process on variants of nano-Ni4Ti3 precipitates and martensitic transformation temperatures in NiTi shape memory alloy," *Mater. Des.*, vol. 142, pp. 93–100, Mar. 2018, doi: 10.1016/J.MATDES.2018.01.024.

[46] X. Huang and Y. Liu, "Effect of annealing on the transformation behavior and superelasticity of NiTi shape memory alloy," *Scr. Mater.*, vol. 45, no. 2, pp. 153–160, Jul. 2001, doi: 10.1016/S1359-6462(01)01005-3.

[47] M. T. Andani, C. Haberland, J. Walker, and M. Elahinia, "An Investigation of Effective Process Parameters on Phase Transformation Temperature of Nitinol Manufactured by Selective Laser Melting," Sep. 2014, doi: 10.1115/SMASIS2014-7649.

[48] S. Saedi *et al.*, "Shape memory response of porous NiTi shape memory alloys fabricated by selective laser melting," *J. Mater. Sci. Mater. Med.*, vol. 29, no. 4, 2018, doi: 10.1007/s10856-018-6044-6.

[49] G. . Firstov, R. . Vitchev, H. Kumar, B. Blanpain, and J. Van Humbeeck, "Surface oxidation of NiTi shape memory alloy," *Biomaterials*, vol. 23, no. 24, pp. 4863–4871, Dec. 2002, doi: 10.1016/S0142-9612(02)00244-2.

[50] T. L. Turner, "Thermomechanical response of shape memory alloy hybrid composites," *NASA Tech. Memo.*, no. 210656, 2001.

[51] S. Saedi, A. S. Turabi, M. T. Andani, N. S. Moghaddam, M. Elahinia, and H. E. Karaca, "Texture, aging, and superelasticity of selective laser melting fabricated Ni-rich NiTi alloys," *Mater. Sci. Eng. A*, vol. 686, no. November 2016, pp. 1–10, 2017, doi: 10.1016/j.msea.2017.01.008.

[52] C. L. Chu, C. Y. Chung, and P. H. Lin, "DSC study of the effect of aging temperature on the reverse martensitic transformation in porous Ni-rich NiTi shape memory alloy fabricated by combustion synthesis," *Mater. Lett.*, vol. 59, no. 4, pp. 404–407, Feb. 2005, doi: 10.1016/J.MATLET.2004.08.036.

[53] G. Tadayyon, M. Mazinani, Y. Guo, S. M. Zebarjad, S. A. M. Tofail, and M. J. P. Biggs, "Study of the microstructure evolution of heat treated Ti-rich NiTi shape memory alloy," *Mater. Charact.*, vol. 112, pp. 11–19, Feb. 2016, doi: 10.1016/J.MATCHAR.2015.11.017.

[54] T. Bormann, B. Müller, M. Schinhammer, A. Kessler, P. Thalmann, and M. de Wild, "Microstructure of selective laser melted nickel–titanium," *Mater. Charact.*, vol. 94, pp. 189–202, Aug. 2014, doi: 10.1016/j.matchar.2014.05.017.

[55] W. Tang, "Thermodynamic study of the low-temperature phase B19′ and the martensitic transformation in near-equiatomic Ti-Ni shape memory alloys," *Metall. Mater. Trans. A*, vol. 28, no. 3, pp. 537–544, Mar. 1997, doi: 10.1007/s11661-997-0041-6.

[56] H.-Y. Wang *et al.*, "Refinement and modification of primary Mg 2 Si in an Al–20Mg 2 Si alloy by a combined addition of yttrium and antimony," *CrystEngComm*, vol. 19, no. 42, pp. 6365–6372, 2017, doi: 10.1039/C7CE01309D.

[57] J. X. Zhang, M. Sato, and A. Ishida, "On the Ti2Ni precipitates and Guinier-Preston zones in Ti-rich Ti-Ni thin films," *Acta Mater.*, vol. 51, no. 11, pp. 3121–3130, Jun. 2003, doi: 10.1016/S1359-6454(03)00124-1.

[58] P. R. Halani, I. Kaya, Y. C. Shin, and H. E. Karaca, "Phase transformation characteristics and mechanical characterization of nitinol synthesized by laser direct deposition," *Mater. Sci. Eng. A*, vol. 559, pp. 836–843, Jan. 2013, doi: 10.1016/j.msea.2012.09.031.

[59] R. E. Smallman and A. H. W. Ngan, *Introduction to Dislocations*. 2014.

[60] C. Lexcellent, S. Leclercq, B. Gabry, and G. Bourbon, "The two way shape memory effect of shape memory alloys: an experimental study and a phenomenological model," *Int. J. Plast.*, vol. 16, no. 10–11, pp. 1155–1168, Jan. 2000, doi: 10.1016/S0749-6419(00)00005-X.

[61] J. Zhu *et al.*, "Influence of Ni4Ti3 precipitation on martensitic transformations in NiTi shape memory alloy: R phase transformation," *Acta Mater.*, vol. 207, p. 116665, Apr. 2021, doi: 10.1016/j.actamat.2021.116665.

[62] N. Zhou, C. Shen, M. F.-X. Wagner, G. Eggeler, M. J. Mills, and Y. Wang, "Effect of Ni4Ti3 precipitation on martensitic transformation in Ti–Ni," *Acta Mater.*, vol. 58, no. 20, pp. 6685–6694, Dec. 2010, doi: 10.1016/j.actamat.2010.08.033.

[63] A. Ishida, K. Ogawa, M. Sato, and S. Miyazaki, “Microstructure of Ti-48.2 at. Pct Ni shape memory thin films,” *Metall. Mater. Trans. A*, vol. 28, no. 10, pp. 1985–1991, Oct. 1997, doi: 10.1007/s11661-997-0155-x.

[64] A. Ishida, M. Sato, T. Kimura, and T. Sawaguchi, “Effects of Composition and Annealing on Shape Memory Behavior of Ti-Rich Ti-Ni Thin Films Formed by Sputtering,” *Mater. Trans.*, vol. 42, no. 6, pp. 1060–1067, 2001, doi: 10.2320/matertrans.42.1060.

Appendix A

As mentioned in the thesis, a number of heating solutions and protective measures were attempted to optimize the heat treatment process for HT1. Table A. 1 gives the furnace types which were used in this work. While the overview of heat treatment conditions is shown in Table A. 2. Fig. A. 1 compares the Vicker's hardness of all samples. HT1 revealed the highest hardness. Furthermore, XRD results did not show any oxidation or other impurities on the surface of all heat treated samples (Fig. A. 2). In addition, the heating process in the referenced literature did not include the heating up procedure [20]. Hence, HT1 was chosen with furnace 1 for the annealing process and furnace 2 for the aging process.

Table A. 1 The overview of furnace.

Furnace	Type	Heating process
Reference [20]	Lindberg/Blue M Box furnace (BF514841)	No heating up
Furnace 1	Carbolite chamber furnace (RHF 1400)	No heating up
Furnace 2	Lenton tube furnace (201008)	No heating up
Furnace 3	Nabertherm chamber furnace	10°C/min

Table A. 2 The overview of heat treatment conditions.

Heat Treatment (HT)	Annealing	Furnace	Protective measurements	Aging	Furnace	Protective measurements
HT1	950 °C for 5.5h and WQ	Furnace 1	Stainless steel bag	350 °C for 18h and WQ	Furnace 2	Stainless steel bag
HT7	950 °C for 5.5h and WQ	Furnace 1	Stainless steel bag			
HT9	950 °C for 5.5h and WQ	Furnace 3	Ti Gd powder and Ar			

HT10	950 °C for 5.5h and WQ	Furnace 3	Ti Gd powder and Ar	350 °C for 18h and WQ	Furnace 3	Ti Gd powder and Ar
HT11	950 °C for 5.5h and WQ	Furnace 1	Stainless steel bag	350 °C for 18h and WQ	Furnace 3	Ar
HT12	950 °C for 5.5h and WQ	Furnace 1	Stainless steel bag	350 °C for 18h and WQ	Furnace 3	Ti Gd powder and Ar
HT13	950 °C for 5.5h and WQ	Furnace 3	Stainless steel bag	350 °C for 18h and WQ	Furnace 3	

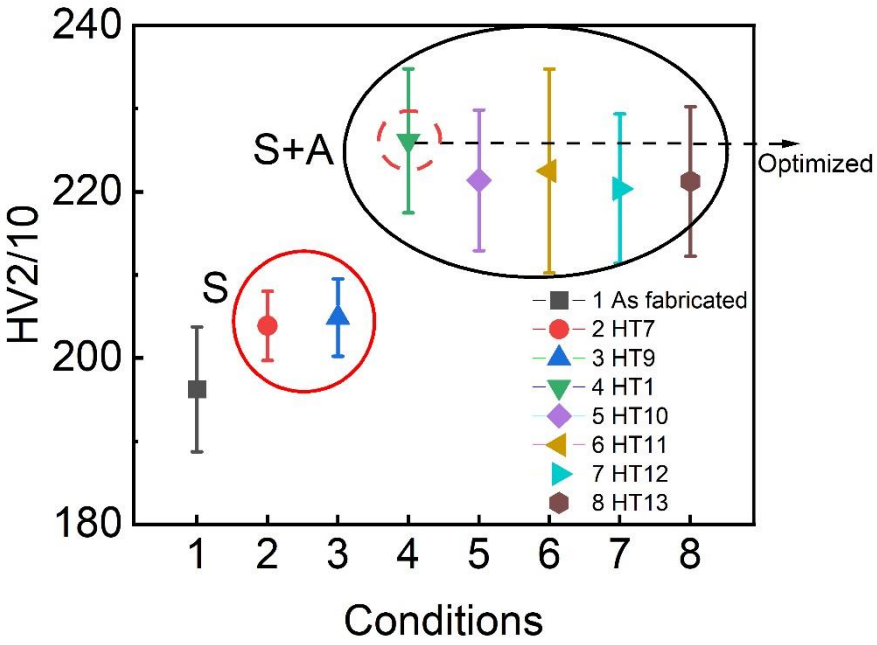

Fig. A. 1 Vickers hardness of A2 as a function of heat treatment conditions

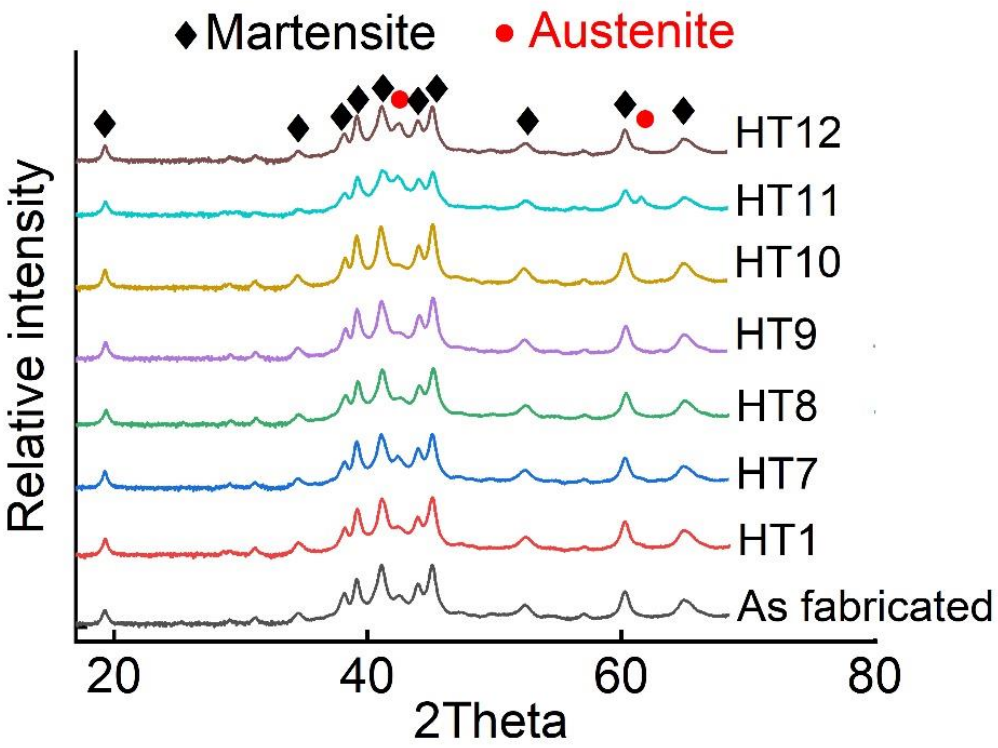

Fig. A. 2 XRD patterns of A2 as a function of heat treatment conditions (NB: background is subtracted with Y-offset, y-scale is in SQRT)

Appendix B

As mentioned in Chapter 4, morphologies of test samples with lower magnification were given in Fig. B. 1–4). It can be observed that an angle of 67° existed between scanning directions, which indicating the schematic of the applied scanning strategy Fig. 3. 1 (b). These samples were etched by H2O (82.7%) +HNO3(14.1%) +HF (3.2%) solution for around 90 sec. The etched microstructures were taken by digital optical microscopy (Keyence VHX-100) with 18 mega-pixel CCD camera.

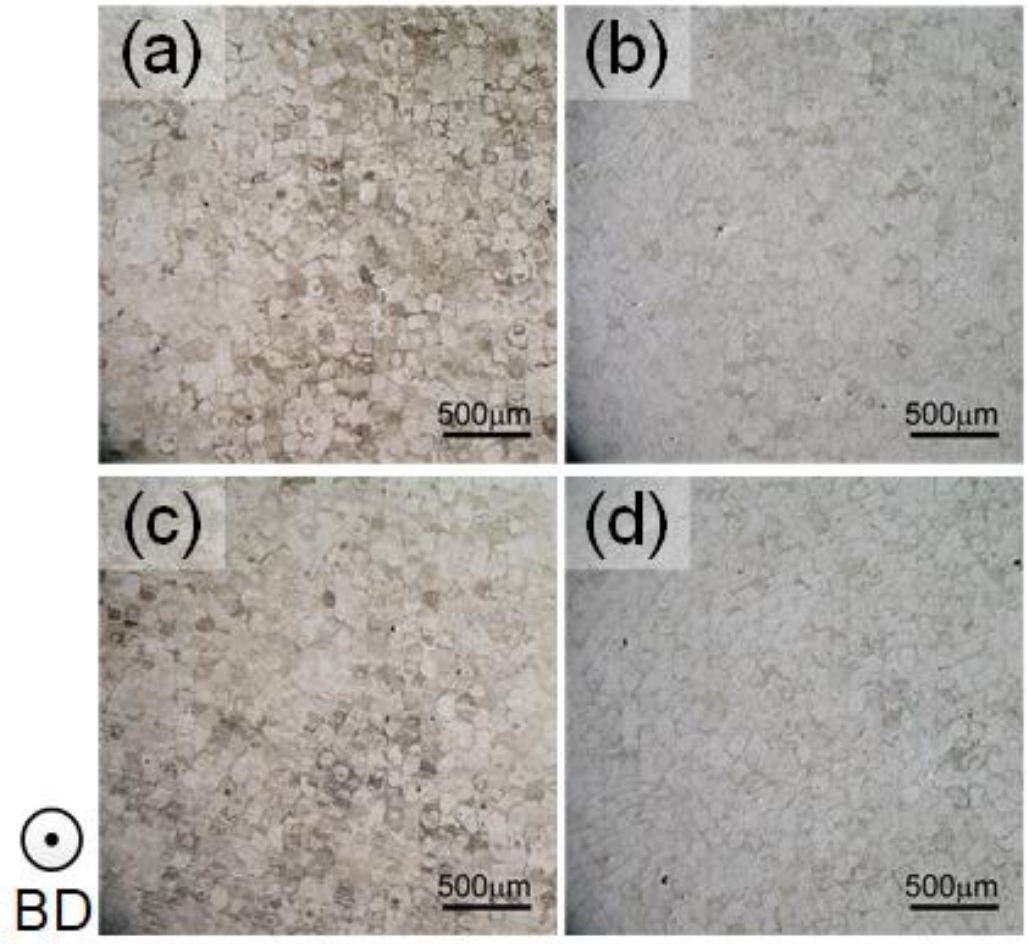

Fig. B. 1 Digital optical microscopy images of top surfaces for A1: (a) As fabricated; (b) HT1; (c) HT2; (d) HT3.

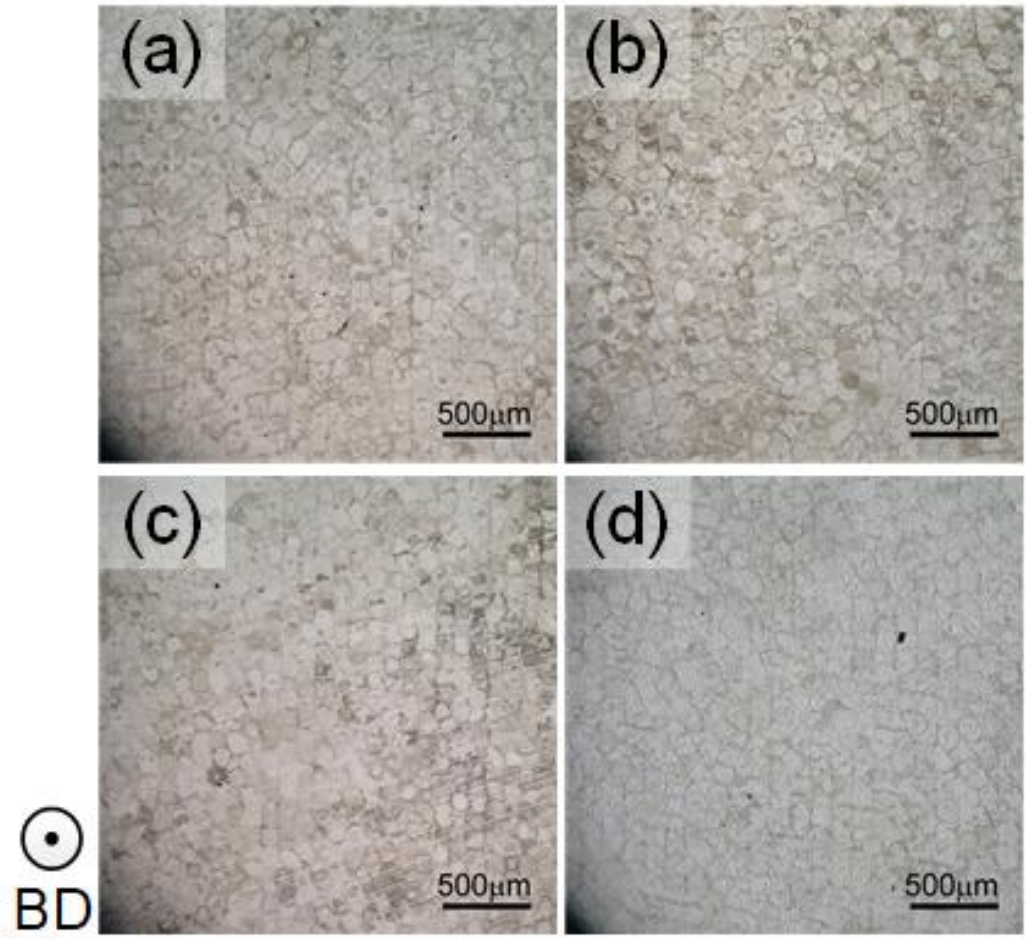

Fig. B. 2 Digital optical microscopy images of top surfaces for A2: (a) As fabricated; (b) HT1; (c) HT2; (d) HT3.

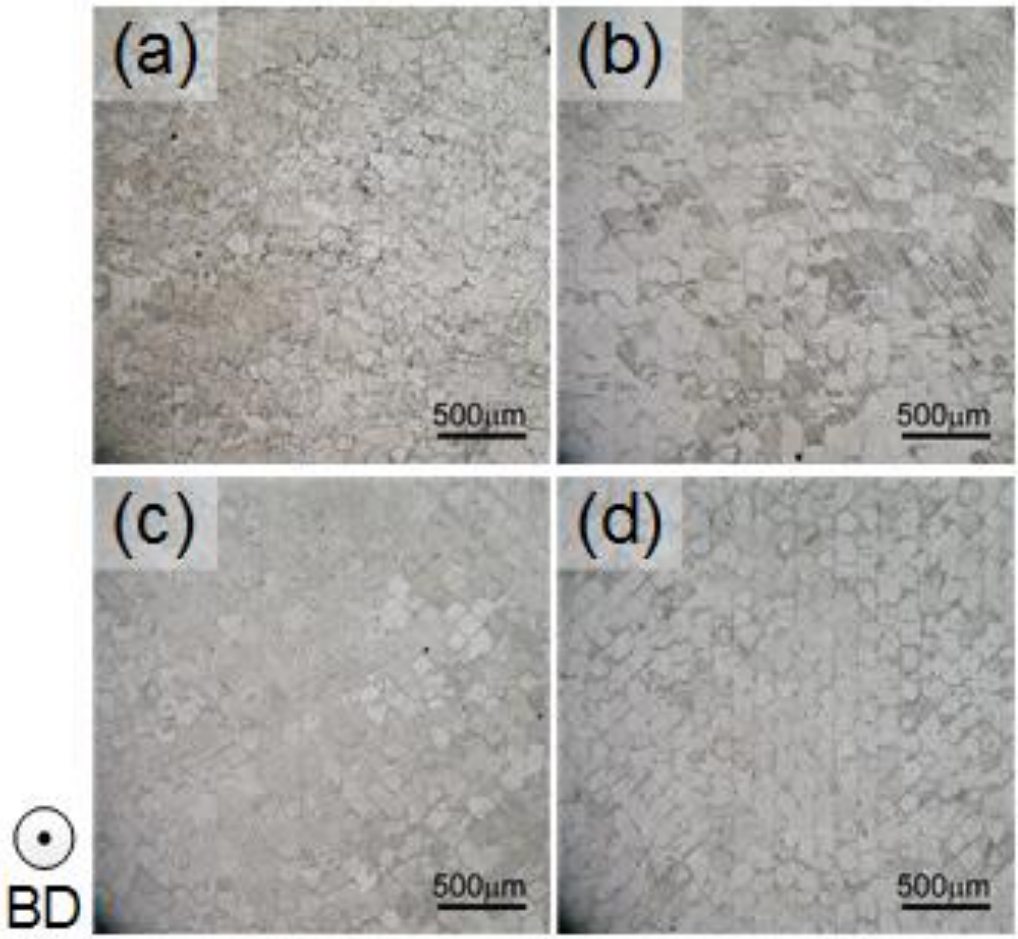

Fig. B. 3 Digital optical microscopy images of top surfaces for A4: (a) As fabricated; (b) HT1; (c) HT2; (d) HT3.

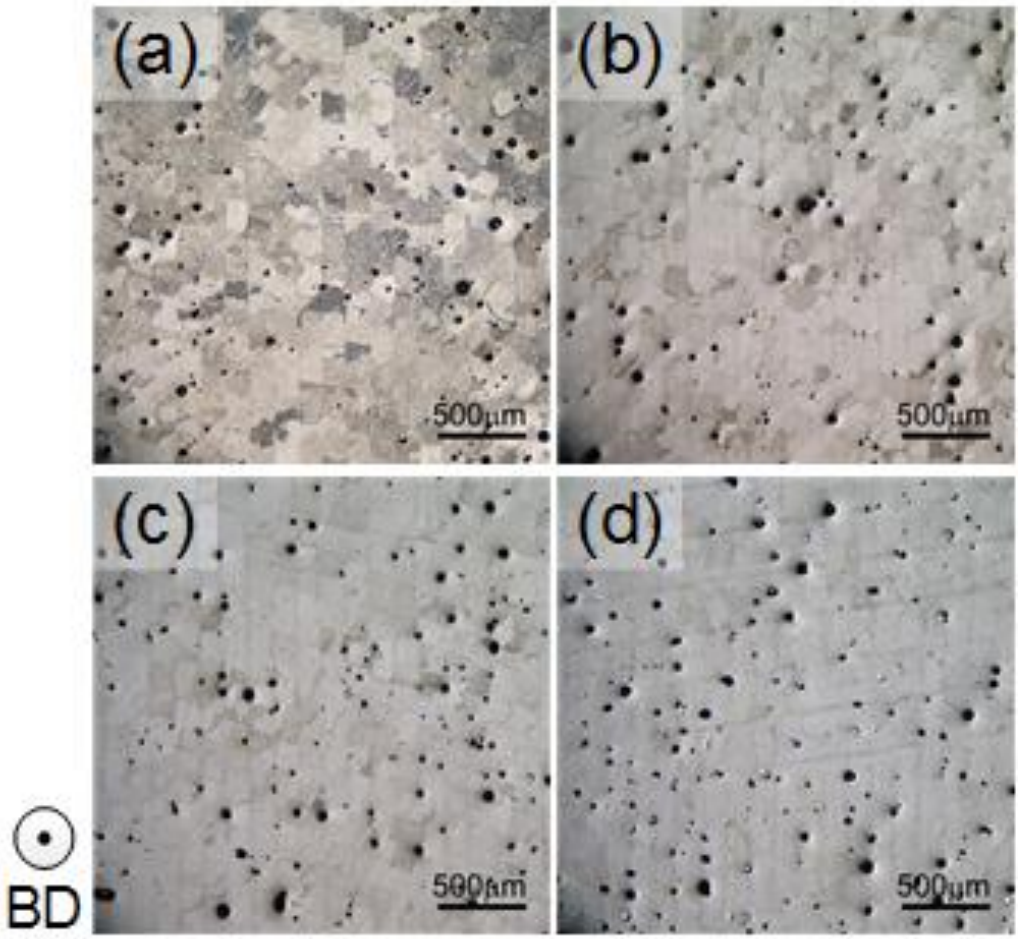

Fig. B. 4 Digital optical microscopy images of the top surfaces for A6: (a) As fabricated; (b) HT1; (c) HT2; (d) HT3.